Hierarchal Visualization of Three-Dimensional Vortical Flow Calculations

by

David L. Darmofal

B.S.A.E. University of Michigan (1989)

SUBMITTED IN PARTIAL FULFILLMENT OF THE
REQUIREMENTS FOR THE DEGREE OF

Master of Science
in
Aeronautics and Astronautics
at the
Massachusetts Institute of Technology

June 1991

©1991, Massachusetts Institute of Technology

Signature of Author _____

Department of Aeronautics and Astronautics
March 4, 1991

Certified by _____

Professor Earll M. Murman
Thesis Supervisor, Department of Aeronautics and Astronautics

Accepted by _____

Professor Harold Y. Wachman
Chairman, Department Graduate Committee

Hierarchal Visualization of Three-Dimensional Vortical Flow Calculations

by

David L. Darmofal

Submitted to the Department of Aeronautics and Astronautics

on March 4, 1991

in partial fulfillment of the requirements for the degree of

Master of Science in Aeronautics and Astronautics

A hierarchal approach for the visualization of complex, three-dimensional vortical flows is presented. This integrated philosophy employs standard and novel visualization techniques to quickly and accurately analyze vortical flows. The hierarchal approach begins by identifying interesting features within the computational domain. Next, these areas of the flow are thoroughly scanned in an attempt to understand the physics which give rise to them. Finally, a variety of extremely interactive probes are used to investigate the finest details of the solution in these regions. Visualization, when approached in this systematic way, is an extremely powerful tool for flow analysis. To aid in understanding of visualization results, the typical features of vortical flows are discussed for a wide range of freestream conditions. The thesis concludes with a detailed visualization of the vortical flow over the National Transonic Facility (NTF) delta wing as calculated by Becker[2]. Using the hierarchal strategy, several interesting flow features including vortex breakdown and vortex sheet instabilities are identified.

Thesis Supervisor: Earll M. Murman,

Professor of Aeronautics and Astronautics

Acknowledgments

During the writing of this thesis, I have been fortunate to be surrounded by some of the best people in the world. This includes my fellow MIT CFDers, a host of great friends, and, of course, my family. I cannot thank everyone enough. Several people deserve special mention for going way beyond the call of duty.

Since the beginning of my graduate work, I have had the privilege of working closely with Phil Poll. I will always remember the late night coffee runs, the thought-provoking technical discussions, and the funny tricks my computer screen would play on me. A true friend. (Is something wrong with Orville?)

Earll Murman, my advisor, has been a terrific person to work with. He has an amazing knack for stimulating new ideas (as well as a knack for pointing out problems in old ones). I am looking forward to continued research with Earll during my doctoral studies.

Peter Schmid is responsible for my education in the fine art of Italian dining. Without his friendship, MIT would be a much harder place to survive. How can one man know so much about mathematics and still have a sense of humor? (Just kidding...)

What can I possibly say about my pseudo-advisor, Bob Haimes, that would be adequate? Thank you so much for everything : the visualization help, the gentle nudges to keep working, the not-so-gentle trouncings on the squash court, *ad infinitum.*

Finally, to my family I owe the greatest debt. In every stage of my life, my parents have always been there to point me in the right direction. And my sister, Debi – I cannot imagine growing up with anyone else. I love you all very much.

Contents

4

List of Figures

Chapter 1

Introduction

Computational fluid dynamics (CFD) has progressed rapidly to become a widely accepted engineering tool along with analytical and experimental approaches. The advances in both computer power and CFD algorithms have led to the calculation of complicated, three-dimensional flows with millions of data points. One of the larger problems facing computational fluid dynamicists is simply understanding the data generated by these huge calculations. In the last decade, computer visualization of three-dimensional data has become the approach used by researchers to understand the results of these calculations. Besides simply being a problem of handling large data sets, results must now be interpreted in three-dimensions. To add a final degree of difficulty, the flow field is often extremely complex and a careful, thorough investigation of the data set is a must. The specific emphasis of this research is the visualization of the vortical flow over delta wings. These flow fields are extremely complicated and varied. The goal of this thesis is to develop an efficient methodology for the visualization of vortical flows using both recently developed and new three-dimensional visualization techniques.

1.1   Background

The vortical flow over a delta wing has been the subject of numerous experimental, theoretical, and computational studies. As the flow progresses around the leading edge, invariably separation occurs. On a sharp leading edge wing, the flow must separate at the leading edge; however, on blunt leading edge wings, the separation line is not fixed. On these wings, the flow can separate from adverse pressure gradients inducing reversed flow. Also, the flow may separate at shocks which are strong enough to generate vorticity. In any case, the resulting shear layer rolls up into a vortex. The presence of the vortex can add significant lift when properly controlled. However, at large angles

12

of attack, a vortex is susceptible to breakdown from the trailing edge pressure gradient. Breakdown can result in a large decrease in lift. If the breakdown is asymmetric, the wing will also suffer a large rolling moment. Frequently the primary vortex is strong enough to induce secondary separation by either an adverse pressure gradient or the presence of a crossflow shock. Similarly, tertiary vortices may also form. Just from these few examples, the complicated nature of vortical flow fields is obvious.

In the last decade, computational fluid dynamicists have managed to calculate many of the dominant features of vortical flows. Euler solutions on sharp leading edge delta wings can simulate primary separation because of the fixed separation location. However, secondary separation, unless shock induced, must be modelled using the Navier-Stokes equations because it is a viscous phenomenon. In flows where secondary effects are minimal, Euler models have proven to be accurate methods of calculating surface pressures [26][27][28]. In blunt leading edge flows, the separation location is no longer fixed; thus, the Navier-Stokes equations must be used to predict separation. These calculations require a much larger effort because of the increased grid resolution near surfaces and the additional viscous fluxes which must be evaluated. Numerous calculations have shown that Navier-Stokes methods can be quite effective in the calculation of vortical flows[28][19][18][24]. A thorough review of the possibilities of vortex flow computation has been given by Hoeijmakers[9] and Newsome and Kandil[24].

After calculating a flow field, the problem of visualizing the results still remains. The first prominent three-dimensional visualization package, PLOT3D, was developed at NASA Ames[13]. PLOT3D featured interactive capabilities and was written for structured mesh computations. Since the introduction of PLOT3D, the development of graphics mini-supercomputers, such as the Stardent GS-2000, has stimulated further advances in 3-D visualization. These machines combine considerable computational abilities with specialized graphics imaging power. At M.I.T, Giles and Haimes[6] recently developed an interactive visualization package on the Stardent GS-2000. Their package, VISUAL3, was written for unstructured grids and also allows the visualization of unsteady calculations[7]. VISUAL3 is the framework for the visualization research of this thesis. The visualization techniques to be discussed, as well as some not mentioned, are all available in VISUAL3. One of the unique features of VISUAL3 is the underlying program architecture. Unlike PLOT3D, VISUAL3 was written for generic volumetric

three-dimensional scalar and vector fields.

1.2 Overview

First, Chapter 2 discusses the various types of flow one expects to find on delta wings. Included in this discussion is the dependence of these flow fields on parameters such as Mach number, angle of attack, Reynolds number, and leading edge shape. Also, trailing edge effects and vortex breakdown are described.

Next, Chapter 3 describes many of the various visualization techniques available in VISUAL3. The techniques are classified to suggest a systematic approach to visualization. Special attention has been given to feature identification visualization techniques which help the researcher to find flow features of interest, as well as the small advances in well-known techniques which significantly increase their "user-friendliness." Algorithmic concerns for new techniques are presented in appendices because the main emphasis of this chapter is in the applicability, not the implementation, of visualization methods.

In Chapter 4, an analysis of a transonic delta wing calculation is presented. The step-by-step description has a twofold purpose: to highlight the power of a systematic visualization process to thoroughly investigate a large, complex data set, and to provide a first-hand experience in the efficient and proper use of a variety of visualization techniques. This chapter is a synthesis of the previous chapters in which the visualization techniques of Chapter 3 are used to gain a better insight into the complicated vortical flow features of Chapter 2.

Finally, in Chapter 5, conclusions are drawn on the effectiveness of the hierarchal approach to visualization of vortical flows and complex flow fields in general. In addition, recommendations are given for future visualization research work.

14

Chapter 2
Vortical Flow Features

The complex and varied flow features found over a delta wing have been studied since the early 1950's when the design of supersonic aircraft first began to be of interest. The additional lift which a vortex provides can add greatly to the performance of a delta wing during manuevers or landings. However, because the flow over a delta wing has many widely varying flow topologies, a slight change in freestream conditions can often mean a large change in the performance of a delta wing. Furthermore, vortices at high angles of attack are susceptible to breakdown which can result in a dramatic decrease in lift.

The purpose of this chapter is to provide a background on the current understanding of vortical flows from experimental, theoretical, and numerical results. The first part of this chapter discusses the typical structure of a vortex and defines some of the aerodynamic terms which will be used to identify vortices during visualization. Then, a discussion of the various vortical flow topologies is presented including a parameterization of these flows. Next, the effects of leading edge bluntness and Reynolds number are considered. Finally, a description of trailing edge effects and vortex breakdown conclude the discussion of vortical flow features.

2.1   Structure of a Vortex

The structure of an isolated vortex is typically divided into two main regions. At the vortex axis is a viscous core which rotates as a solid body. The effects of viscosity dominate in this region because, as in a boundary layer, the shear is high due to the tangential velocity rapidly decaying to zero at the core axis. Outside of the viscous core is a region of the flow which approaches a potential flow corresponding to a point vortex. The viscous core eliminates the velocity singularity at the vortex axis of the potential

flow point vortex model. A model often used to describe the velocity distribution in a vortex is the Lamb vortex. The tangential velocity component of a Lamb vortex is:

$$u_\theta = \frac{\Gamma}{2\pi r}\left\{1 - e^{-\left(\frac{r}{a}\right)^2}\right\} \qquad (2.1)$$

where Γ is the circulation and a is the core radius. Near the vortex axis, as $r \to 0$, a first order expansion shows that Equation 2.1 becomes:

$$u_\theta = \frac{\Gamma}{\pi a^2}\, r. \qquad (2.2)$$

The velocity distribution in the core is linear; thus, the core is in solid body rotation. A similar first-order expansion as $r \to \infty$ gives:

$$u_\theta = \frac{\Gamma}{2\pi r}. \qquad (2.3)$$

Thus, the outer velocity distribution is the potentialflow due to a point vortex.

2.1.1 Total Pressure Loss

The total pressure loss is defined as:

$$C_{pl} = 1 - \frac{C_{p0}}{C_{p0_\infty}} \qquad (2.4)$$

where C_{p0} and C_{p0_∞} are the local and freestream total pressures, respectively. When the flow undergoes a loss, the total pressure decreases and thus the total pressure loss approaches unity. A value of zero total pressure loss indicates the flow is isentropic. Total pressure losses may occur from viscous effects or across shocks. In the case of a vortex, large total pressure losses occur in the vortex core where viscous effects dominate. Thus, high total pressure losses are often used to locate vortices during calculation and visualization of vortical flows. Surprisingly, Euler solutions, which lack a physical viscous loss mechanism, also produce total pressure losses in vortical regions of the flow. Research by Powell[26] indicates that the total pressure loss is a result of artificial viscosity. Thus, total pressure loss can be used to successfully locate vortices in both Euler and Navier-Stokes calculations.

16

2.1.2 Helicity and Helicity norm

Helicity and helicity norm are defined as:

$$H \equiv \text{helicity} = \vec{u} \cdot \vec{\omega} \tag{2.5}$$

$$H_n \equiv \text{helicity norm} = \frac{\vec{u} \cdot \vec{\omega}}{|\vec{u}||\vec{\omega}|} \tag{2.6}$$

where $\vec{\omega} = \nabla \times \vec{u}$, is the vorticity vector. Helicity and helicity norm are a measure of the helical, and thus, the vortical motion of the flow[16]. An important aspect of helicity is that its sign indicates the sense of rotation. When the velocity and vorticity vectors are aligned, helicity will be positive; if they point in opposite directions, helicity will be negative. Thus, primary and secondary vortices will have opposite signs of helicity making them easy to distinguish visually.

Helicity norm is simply the cosine of the angle between the local velocity and vorticity vectors. When its magnitude is one, the velocity and vorticity vectors lie along the same line. At the axis of a vortex, the helicity norm tends toward one for most flows. Along the vortex axis, a non-unity value of helicity norm indicates the presence of vorticity not aligned to the streamwise direction. This portion of the vorticity vector is responsible for the turning of the axis streamline. Since the axis of a vortex is essentially straight except near the wing apex or trailing edge, the helicity norm will approach one. For a more thorough discussion on the usefulness of helicity and helicity norm in vortical flows see Levy[16].

2.2 Flow Classifications for a Sharp-leading Edge

Some of the more prominent experimental studies of delta wings have occured in the last decade. Of particular note are the experiments of Miller and Wood[21], Seshadri and Narayan[23], and McMillin et al[19]. These efforts aimed at collecting data over a wide range of freestream conditions in an attempt to better parameterize the various flow topologies found. Miller and Wood, following the work of Stanbrook and Squire[33], choose to parameterize their results according to M_n and α_n, the Mach number and angle of attack normal to the leading edge, respectively. Specifically, these are defined

by:

$$M_n = M_\infty \sin \alpha \csc \alpha_n = M_\infty \left(1 - \sin^2 \Lambda \cos^2 \alpha\right)^{\frac{1}{2}} \qquad (2.7)$$

$$\alpha_n = \tan^{-1} \left(\frac{\tan \alpha}{\cos \Lambda}\right) \qquad (2.8)$$

where Λ is the leading edge sweep angle. The tangential Mach number component is given by:

$$M_t = M_\infty \cos \alpha \sin \Lambda. \qquad (2.9)$$

From their results for a large variety of sharp leading edge delta wings, they defined seven unique flow categories. Seshadri and Narayan continued by adding two more categories which are slight variations upon the Miller and Wood types. Furthermore, Seshadri and Narayan also investigated the effects of Reynolds number and of leading edge bluntness upon vortical flows. McMillin revised the boundaries of the Miller and Wood vortical flow classifications. Finally, although experimental results for hypersonic flows are lacking, some independent numerical results for the Navier-Stokes equations over a delta wing indicate the presence of a tenth type of flow topology[29][30]. Figure 2.1 shows the various flow types in α_n, M_n space. The boundaries defining the various regimes are meant to indicate only the general location of the flow types. Also, the hypersonic boundary is dashed because no thorough parameterization studies have been done in that regime. Its placement on the figure simply indicates that this flow type has high Mach number and angle of attack. The remainder of this section describes the wide variety of sharp leading edge flow classifications previously mentioned using typical surface pressure distributions, oil flow data, and crossflow diagrams (Figures 2.2 - 2.11).

2.2.1   Type 0: Attached Flow

This flow is only achievable at the smallest angles of attack and Mach number. The flow field is subsonic throughout and attached over the entire surface. The oil flow on the leeward surface shows the flow rounding the leading edge at a direction nearly normal to it. Progressing inboard, the oil flow gradually adjusts to the freestream direction. The pressure distribution reveals the leading edge suction peak and its rapid decrease away from the leading edge.

2.2.2 Type 1: Separation Bubble / No Shock

At very low normal angles of attack and Mach number, the separated flow region will consist solely of a bubble. Outside of the separation bubble, the flow is irrotational. Thus, the effect of the separation bubble is an apparent thickening of the delta wing leading edge. The pressure is low under the separation bubble and rises as the flow reattaches. The surface pattern shows outward flow under the bubble and streamwise flow inboard of the reattachment line. Also, near the leading edge, another oil accumulation line can been seen probably indicating a small region of reversed flow. In this regime, the suction peak essentially occurs very near the leading edge.

2.2.3 Type 2: Full Separation / No Shock

Often referred to as the classical vortex, this type occurs for α_n from about 8 to 40 degrees and subsonic normal Mach numbers. The crossflow diagram shows a shear layer emanating from the leading edge. The primary vortex is displaced slightly by the inboard secondary vortex. This displacement effect increases with the angle of attack; furthermore, as the vortex system continues rising above the leeward surface, tertiary vortices will eventually appear. The flow features with only primary and secondary vortices can easily be extended to included tertiary effects, thus, no discussion of the tertiary system will be given. Oil flow data clearly displays the primary attachment line. It borders the flow near the symmetry plane which is directed along the freestream. As the angle of attack, or Mach number is increased, the primary attachment line will continue moving inboard to the symmetry plane. Some experimental and numerical results have indicated that embedded shocks may also exist under the primary vortex in the Type 2 vortical flow region[35][26]. A substantial pressure gradient underneath the primary vortex definitely exists, however, a shock is not present in many other results[21][23]. The secondary separation line is the line outboard of the primary attachment. Secondary separation in a classical vortex is caused by separation of the boundary layer due to an adverse pressure gradient just outboard of the primary vortex[25]. Finally, the secondary flow reattaches itself on the oil flow line just inboard of the leading edge. The flow between the secondary attachment line and the leading edge flows outward and

eventually joins the shear layer at the leading edge. The surface pressure again shows the suction peak at the leading edge. Travelling inboard, the pressure continues decreasing because of the primary and secondary vortices. Then, near the primary reattachment line, the pressure rises significantly due to the higher pressure of the freestream-directed flow. As mentioned previously, the primary attachment line and vortex move inboard with increasing angle of attack or Mach number; thus, the lower pressure region will extend further inboard. For nominal increases, this results in a subsequent increase in lift.

2.2.4 Type 3: Full Separation / Embedded Shock

This flow regime is the transonic normal Mach number case of the classical, Type 2 vortex. The typical classical vortex system with primary and secondary vortices appears; however, as a result of the higher Mach number, the flow between the wing and the primary vortex is locally supersonic. In order to match the pressure with the flow further outboard, compression occurs via a weak shock underneath the primary vortex. The existence of this type of vortical flow was first recognized by Michael[20] from a subtle redirection of the oil-drop surface lines. Several other experiments and numerical results have also identified the crossflow shock [23] [27] [35]. The surface pressure also shows a small pressure rise associated with the crossflow shock. Note that for this weak shock, the secondary flow remains attached until the adverse pressure gradient further outboard is encountered. Thus, Type 3 flows still have a pressure-induced secondary separation.

2.2.5 Type 4: Shock-induced Secondary Separation

Type 4 and Type 3 flows are very closely related. The only difference is the mechanism of secondary separation. The higher normal angle of attack in Type 4 provides the embedded shock with enough strength to separate the boundary layer causing secondary separation further inboard than in the pressure-induced separation. Narayan and Seshadri noticed a sudden inward movement of the secondary separation line when the shock causes separation [23]. Since the shock and separation occur at the same location,

the "kink" in the oil flow patterns disappears because it now lies on a separation line. The pressure distribution on the surface is essentially identical to Type 3.

2.2.6   Type 5: Full Separation / Shock

At high angles of attack, a shock appears above the classical vortex (Type 2) to provide turning at the symmetry plane. The main features of the oil flow pattern are the same as seen in the classical vortex except the streamwise flow near the symmetry plane is absent. The entire vortex system shifts inboard with angle of attack; thus the low pressure region covers more of the leeward surface. The shock, being located on the top of the primary vortex, cannot be detected from the surface pressure coefficient. At the higher angles of attack, additional shocks at the symmetry plane and underneath the primary vortex may be present. A similar embedded shock system is described in the discussion of Type 9, hypersonic flow fields.

2.2.7   Type 6: Attached Flow / Shock

At supersonic normal Mach numbers, the flow around the sharp leading edge undergoes an isentropic Prandtl-Meyer expansion. The flow must then turn streamwise at the symmetry plane; the Mach number is supersonic because of the expansion around the leading edge, thus, the turning is accomplished through an oblique shock. If the shock strength is relatively low, the boundary layer will remain attached after the shock; consequently, the flow over the entire wing will be attached. The oil flow pattern is extremely similar to Type 0 attached flow with subtle kink in the oil flow lines at the shock. The pressure distribution shows the typical suction peak at the leading edge which is then followed by a compression through the shock.

2.2.8   Type 7: Shock-induced Primary Separation

When the shock strength is large enough, the boundary layer of Type 6 flow will separate forming a primary separation region. Narayan and Seshadri [31], based on an idea from Korkegi [11], suggest that the incipient shock and boundary layer interaction is

21

qualitatively and quantitatively similar to a glancing shock interaction on a flat plate (see Figure 2.12). The only essential difference is that the shock for the flat plate is generated by a wedge while for the delta wing it is generated because of the symmetry condition. Based on a large amount of data, Korkegi correlated incipient separation in a turbulent boundary layer with a pressure ratio of 1.5 across the shock; assuming this correlation correct for delta wings, Narayan and Seshadri were able to calculate the boundary for separation on the $\alpha_n - M_n$ plane. This boundary matched remarkably well with the observed separation on oil flow data from a variety of experiments.

The oil flow shows inboard flow until the shock. Just beyond the shock in the rotational region of the flow, the experimental surface lines are difficult to discern because the vortical region is extremely small. Thus, the pattern shown in Figure 2.9 underneath the primary vortex is drawn randomly. Finally, the flow reattaches and is streamwise along the symmetry plane. The pressure distribution shows the leading edge suction, the crossflow shock, and the symmetry plane compression.

An interesting aspect of Figure 2.1 for flow types 6 and 7 is that separation is extremely sensitive to the normal angle of attack, but almost completely insensitive to the normal Mach number. This implies that the shock strength is extremely sensitive to the normal angle of attack but essentially insensitive to the normal Mach number because it is the shock strength, or pressure rise across a shock, which causes the boundary layer to separate. Increasing the normal Mach number while holding the normal angle of attack constant raises the Mach number normal to the shock but the flow turning angle needed to match symmetry condition remains nearly constant. However, increasing the normal angle of attack while holding the normal Mach number constant increases the turning angle while the Mach number normal to the shock remains nearly constant. The shock table in Figure 2.13 shows that for pressure ratios near 1.5, the shock strength (i.e. pressure ratio) is extremely sensitive to small perturbations of the turning angle but relatively insensitive to perturbations in incoming Mach number. Thus, as shown by the Type 6 and Type 7 boundary in Figure 2.1, increasing the normal angle of attack will lead to separation much sooner than increasing the normal Mach number.

2.2.9 Type 8: Separation Bubble / Shock

As with the classical vortex, the separation bubble forms a shock above it at higher angles of attack. The oil flow patterns, unlike the Type 5 patterns, show the shock position clearly with an accumulation line. Also visible are the primary reattachment and the accumulation line near the leading edge indicating a small reversed flow region. The pressure distribution shows the compression due to the shock over the bubble, again unlike the Type 5 pressure distribution. The placement of this flow type in Figure 2.1 is from the results of McMillin et al[19]. Her results indicated that the separation bubble with a shock is the transition type between fully separated and attached flows. For example, if the flow is initially a separation bubble (Type 1) and the normal Mach number is increased, a shock will first develop over the bubble leading to a Type 8 flow. Then, as normal Mach number increases further, the shock will begin to increase in strength and generate enough vorticity to create full separation beyond it. Thus, a shock-induced primary separation, Type 7 flow, will occur.

2.2.10 Type 9: Hypersonic Flow

In the high Mach number or hypersonic regime, the flow shocks more than once; independent numerical calculations have shown the existence of a shock above the primary vortex and one perpendicular to the symmetry plane[29]. The first shock is necessary to match the symmetry conditions while the second shock is a result of turning at the wing surface. The oil flow patterns are identical to the Type 5 patterns except the two vortices are much more compact in this high Mach number case. The pressure distribution is extremely benign because the leeward surface is nearly a vacuum as a result of the extremely large expansion around the leading edge. Thus, the pressure is constant along nearly the entire upper surface. Blowing-up the resolution of the pressure graph should show a distribution similar to the Type 5 flow below the primary and secondary vortices.

2.3 Leading Edge Bluntness Effects

When the leading edge is blunt, the location of separation is no longer fixed. At low Mach numbers, flow separation, if it occurs, is due to pressure-induced boundary layer separation. As Mach number is increased, a shock may form somewhere along the inboard of the leading edge. Separation may occur at the shock due to either vorticity generation or the large adverse pressure gradient. The consequence of the separation position and type not being fixed is that several flow types may occur over a delta wing with blunt leading edges[23]. For example, the flow may remain attached over the tip region of the wing and later transition into a fully-separated flow. Since the flow is attached over a portion of the wing and also because the suction peak is not a large as in a sharp leading edge, the vortex formed on a blunt delta wing is generally weaker and further inboard. The descriptions of sharp leading edge flows, in general, applies equally to the blunt leading edge flows; the only difference is that several of these flow types can occur on the same wing at different chord locations.

2.4 Reynolds Number Effects

The major effect of Reynolds number on vortical flows are in the location of separation and in the size of the vortex core. The size of the vortex remains essentially constant; however, the size of the core, in which viscous effects are appreciable, is dependent upon the Reynolds number. Once the core becomes turbulent, its size is generally insensitive to Reynolds number variations. Another effect could be whether the boundary layer on the wing is laminar or turbulent. If it is turbulent, separation is less likely to occur and the formation of a vortex may be delayed. Viscous effects are also prominent when vortices are interacting with the boundary layer. Typical instances of this interaction are at low angles of attack or near the tip on a blunt leading edge delta wing. Somewhat surprisingly, these few effects are the major variances of the flow with Reynolds number. One problem with detecting Reynolds number effects is defining a suitable length scale; using the chord seems improper to determine Reynolds number effects for when and where separation occurs. A scale related to the bluntness of the leading edge would seem more appropriate for this purpose. However, a more adequate length scale for the

size of a vortex is probably a local span length. Thus, to simply state that vortical flows are not affected by Reynolds number variations is probably a little naive.

2.5 Trailing-edge Effects and Breakdown

The effect of the trailing-edge is of extreme practical importance. The breakdown of vortices as a result of the trailing-edge pressure gradient can result in a large, sudden loss of lift if the breakdown occurs over the delta wing. Breakdown is generally considered to have two distinct modes[15][25]. Figure 2.14 illustrates the two modes. A bubble mode exists where the vortex reaches a stagnation point and then forms a region of reversed flow; this form appears as if a solid body were placed in the vortex path. The other type, the spiral breakdown, also reaches a stagnation point but then the entire vortex core begins to rotate about its axis in the same direction as the core rotation. The upstream deceleration of the vortex in both breakdowns occurs in only one or two core diameters. Downstream of the breakdown, the flow is highly-oscillatory and turbulent.

Another effect of the trailing-edge is the turning of the vortices back to the freestream direction. If the vortex does not burst, it will be aligned with the freestream as it passes the trailing-edge. The persistence of the vortex downstream of the delta wing is also a worrisome problem in aerodynamic design. The interaction of the delta wing primary vortex with tail surface causes significant unsteady loading which greatly increases its fatigue. Simple viscous dissipation has a neglible effect on decreasing vortex strength and the vortex must be dissipated by turbulent motions. However, even turbulent dissipation is relatively minimal in many cases. The persistence of vortical motion can be seen in the extremely long trailing vortices behind commercial aircraft.
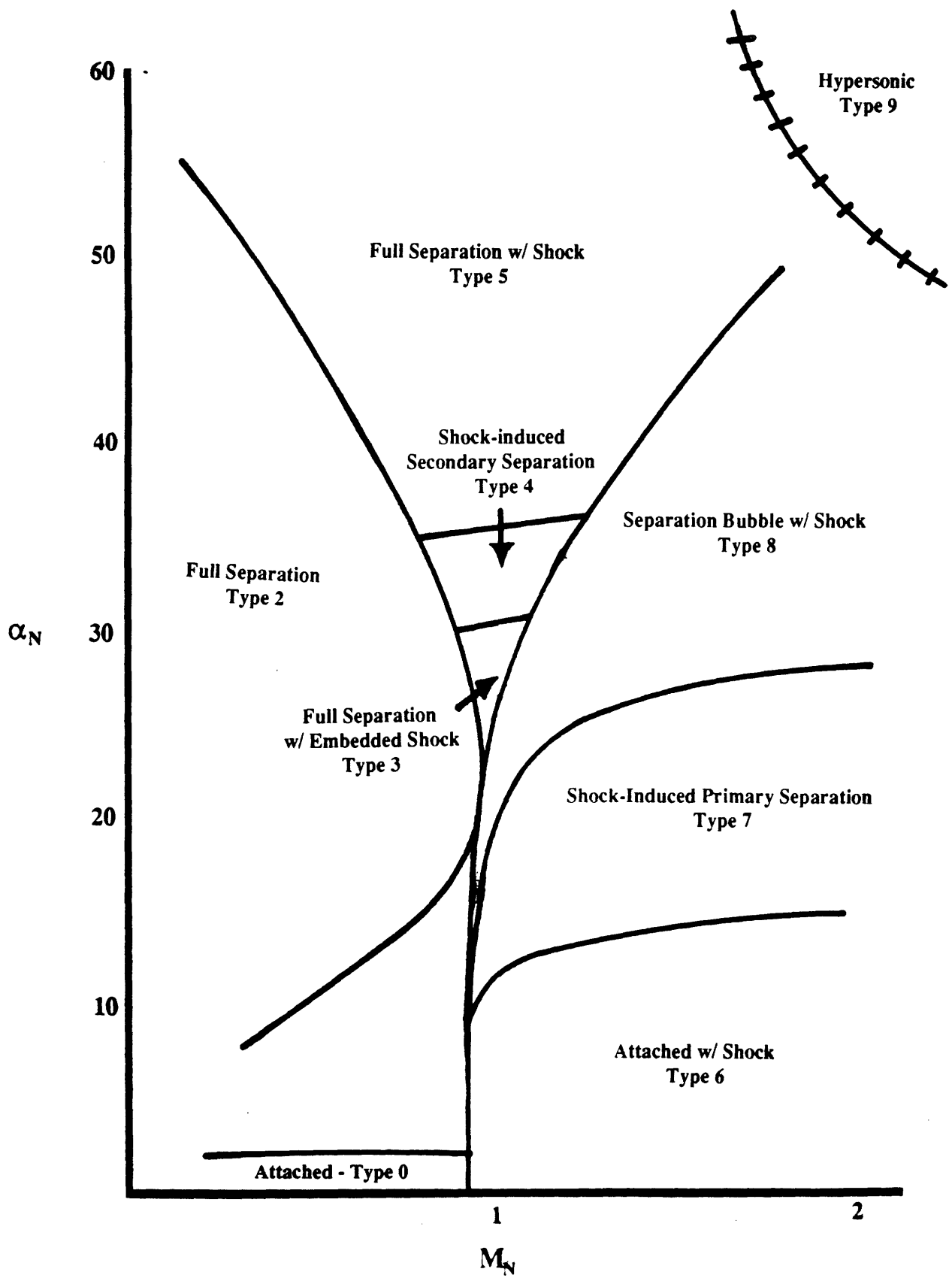
Figure 2.1: Vortical flow classifications

Oil flow

Crossflow

$-C_p$
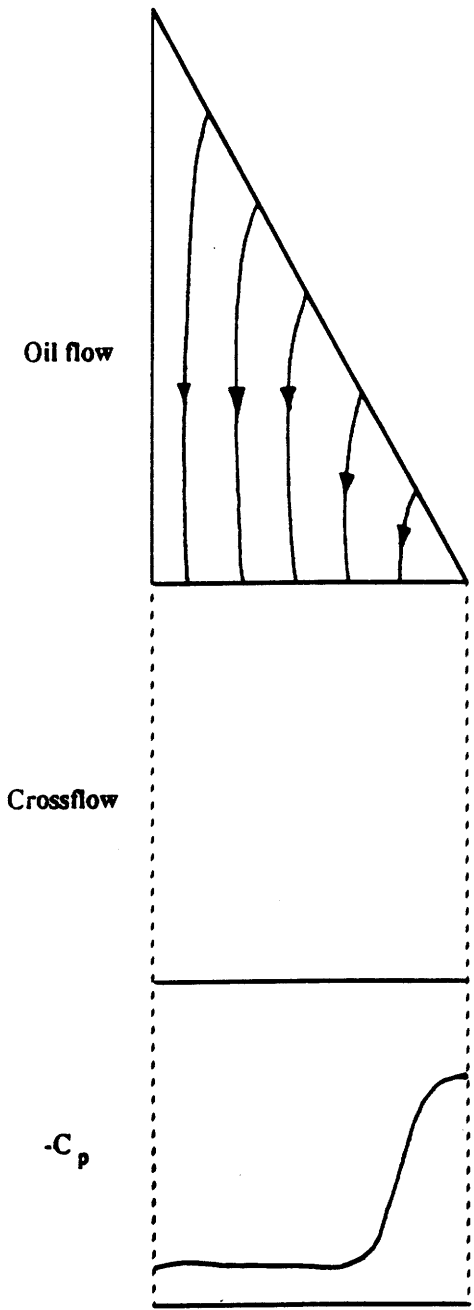
Figure 2.2: Type 0

Attached Flow

Oil flow

Crossflow

$-C_p$
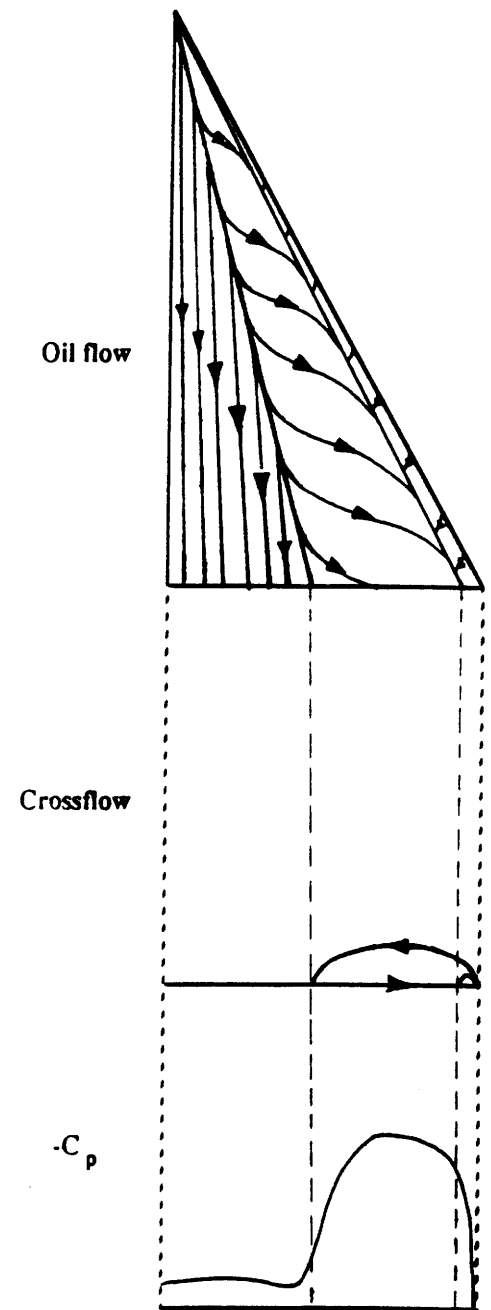
Figure 2.3: Type 1

Separation Bubble

27
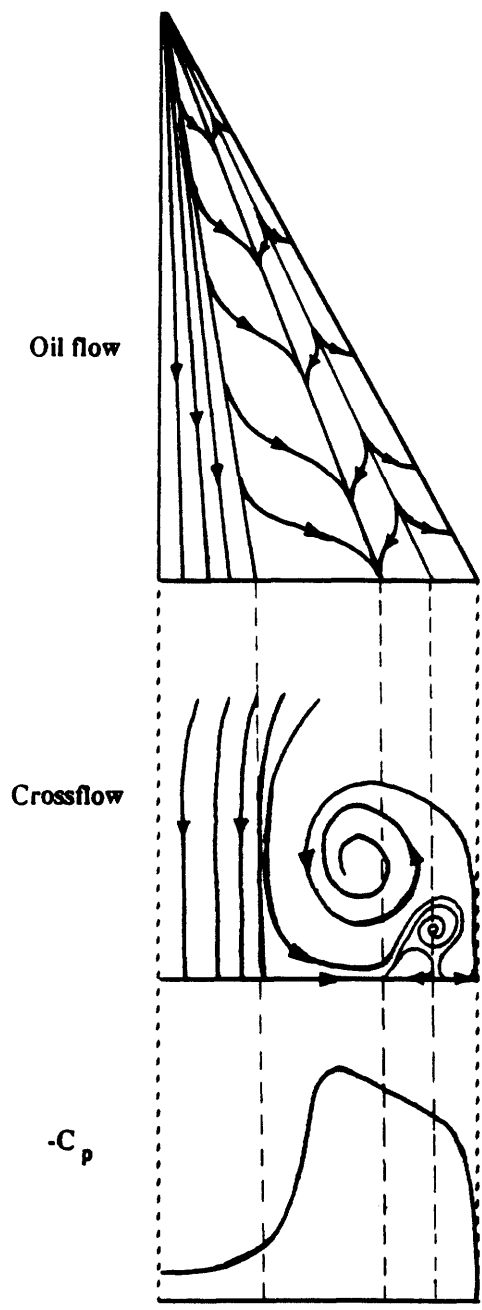
Figure 2.4: Type2

Full Separation
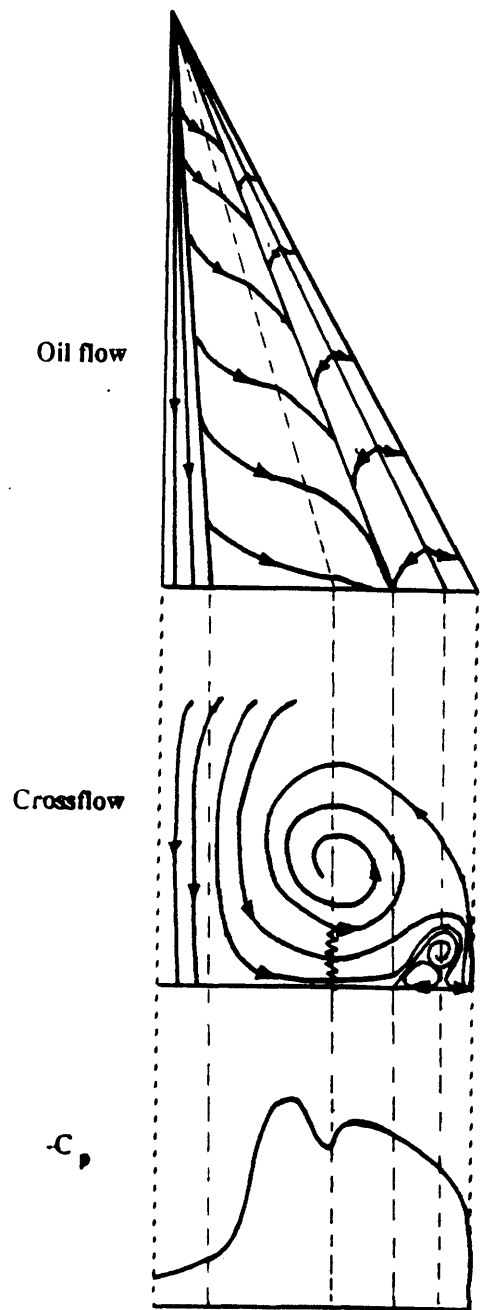
Figure 2.5: Type 3

Full Separation / Embedded Shock

Oil flow

Crossflow

$-C_p$
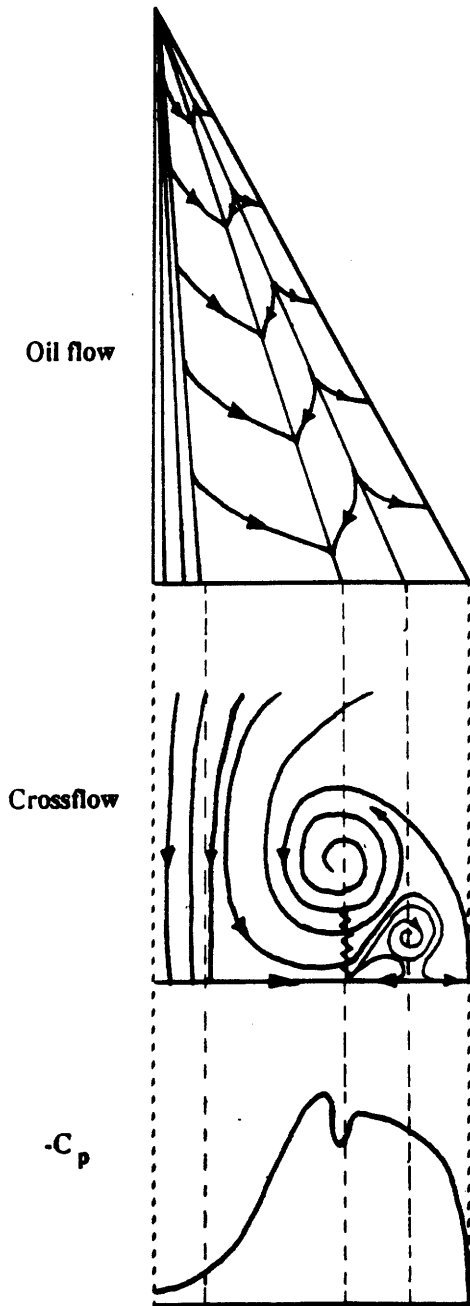
Figure 2.6: Type 4

Shock-induced Secondary Separation

Oil flow

Crossflow

$-C_p$
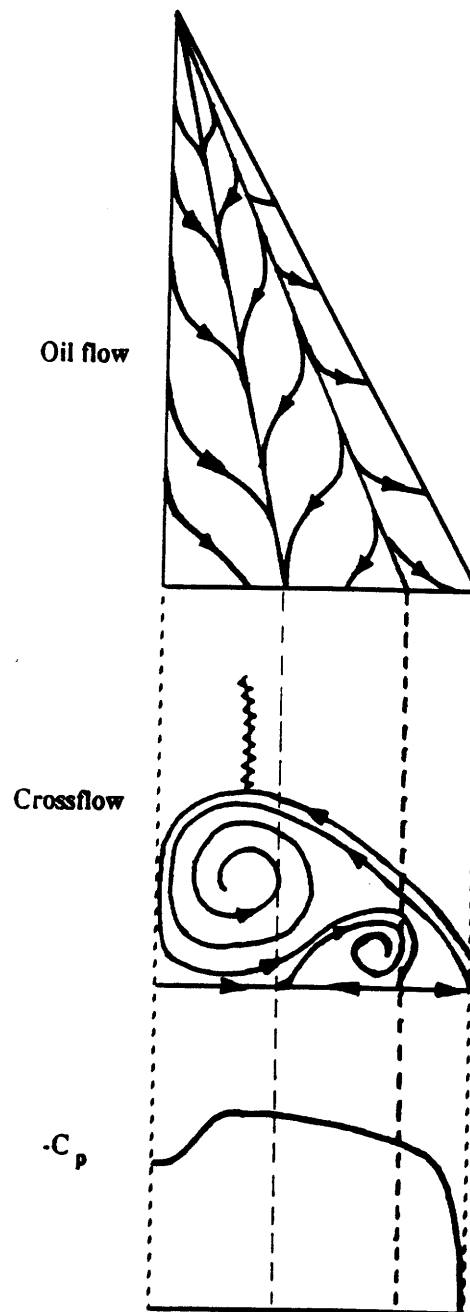
Figure 2.7: Type 5

Full Separation / Shock

29

Oil flow

Crossflow

$-C_p$
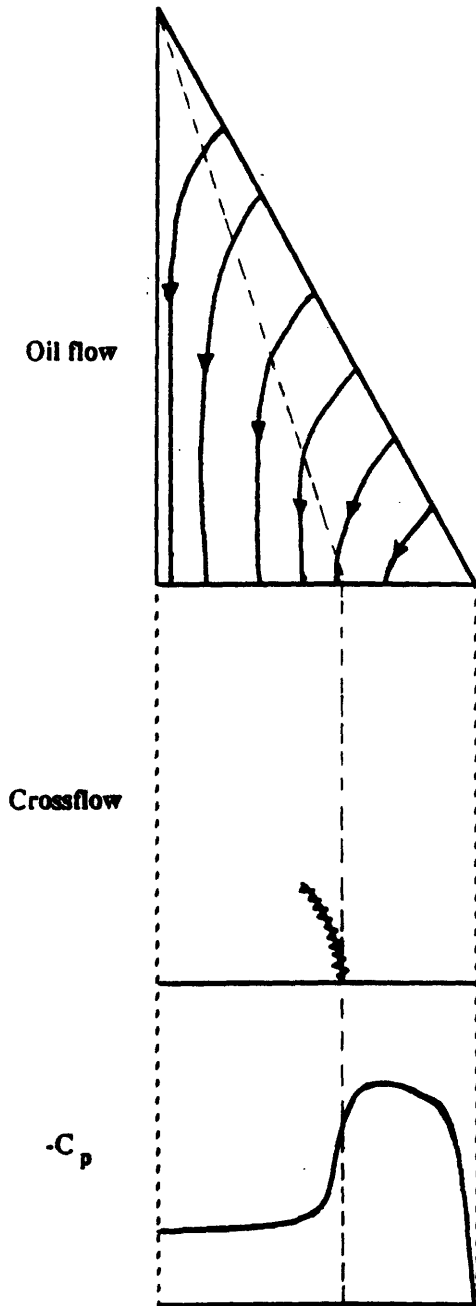
Figure 2.8: Type 6

Attached Flow / Shock

Oil flow

Crossflow

$-C_p$
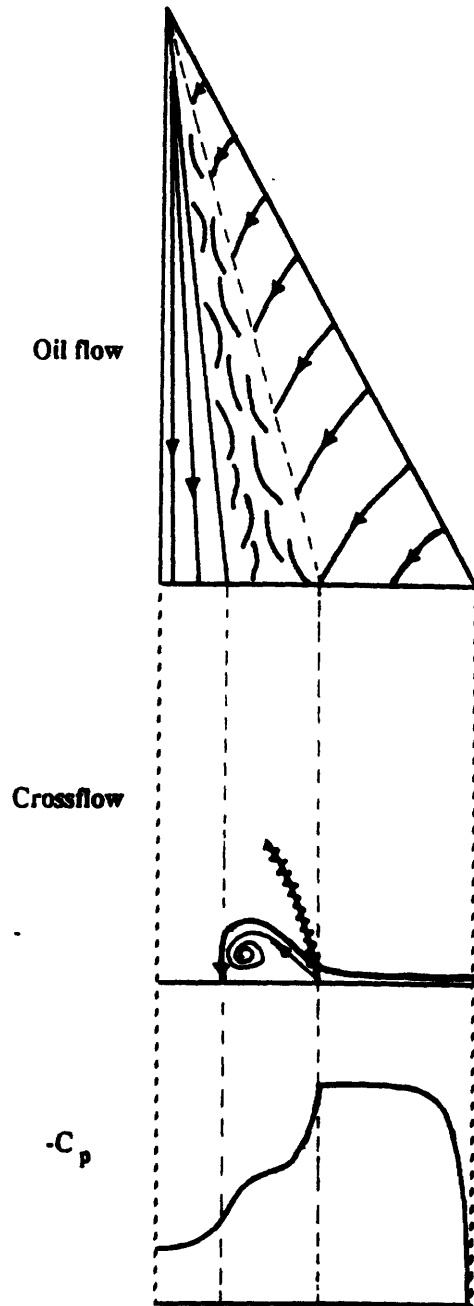
Figure 2.9: Type 7

Shock-induced Primary Separation

30

Oil flow

Crossflow

-C$_p$
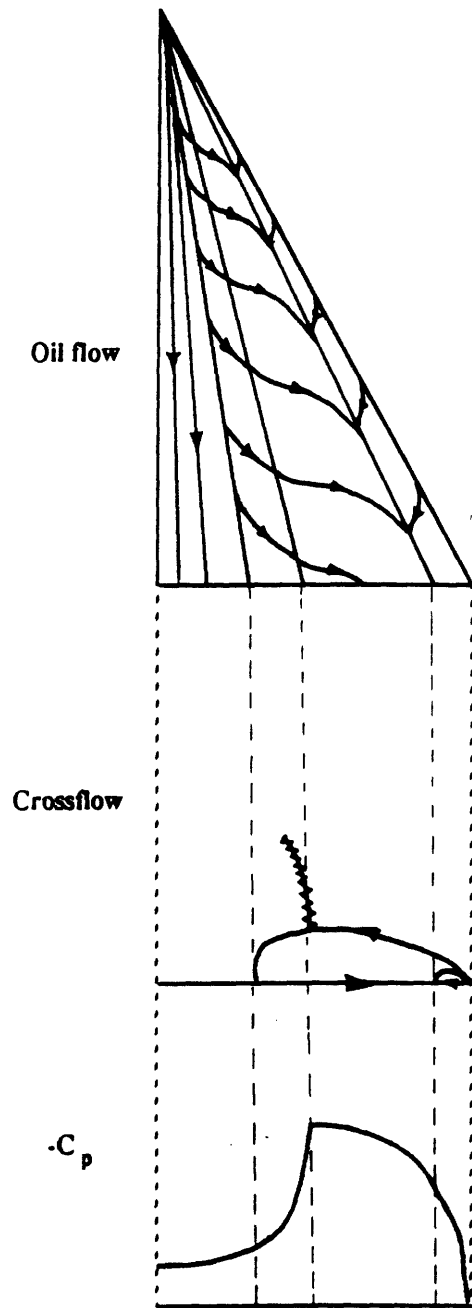
Figure 2.10: Type 8

Separation Bubble / Shock

Oil flow

Crossflow

-C$_p$

Figure 2.11: Type 9

Hypersonic Flow

31
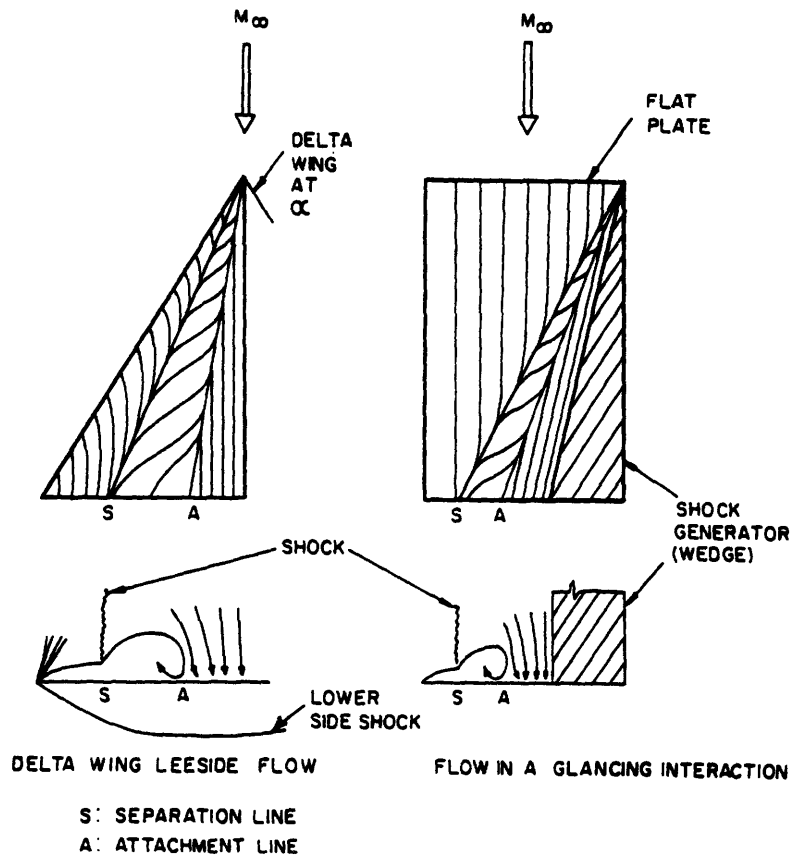
Figure 2.12: Glancing and symmetry plane shock comparison[31]
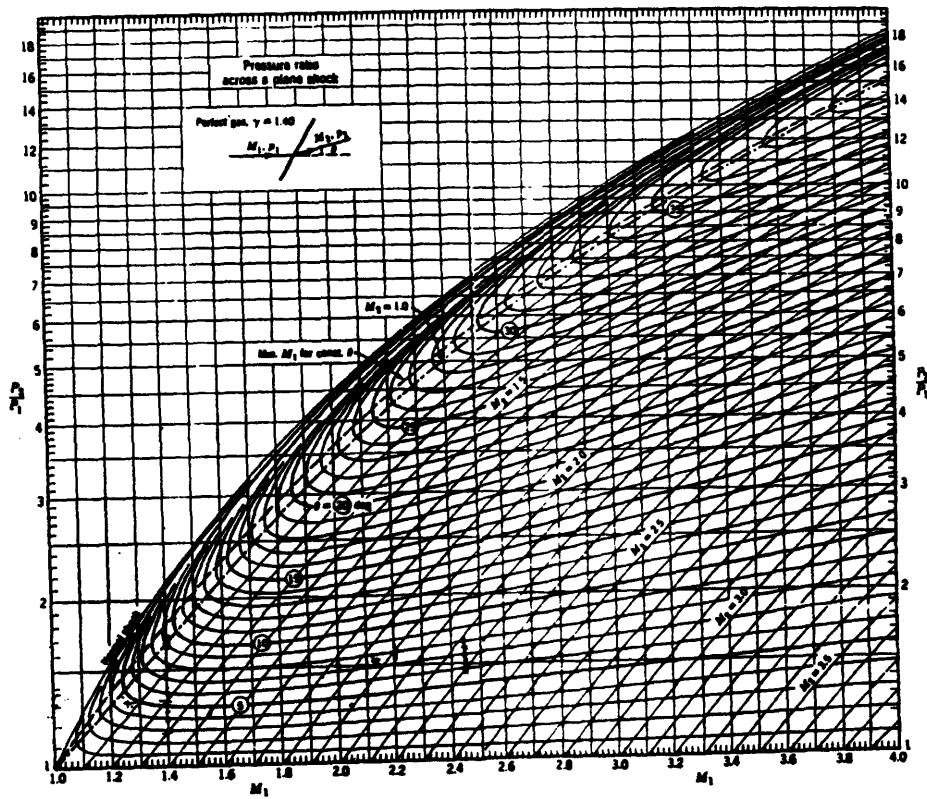
Figure 2.13: Oblique shock tables[3]
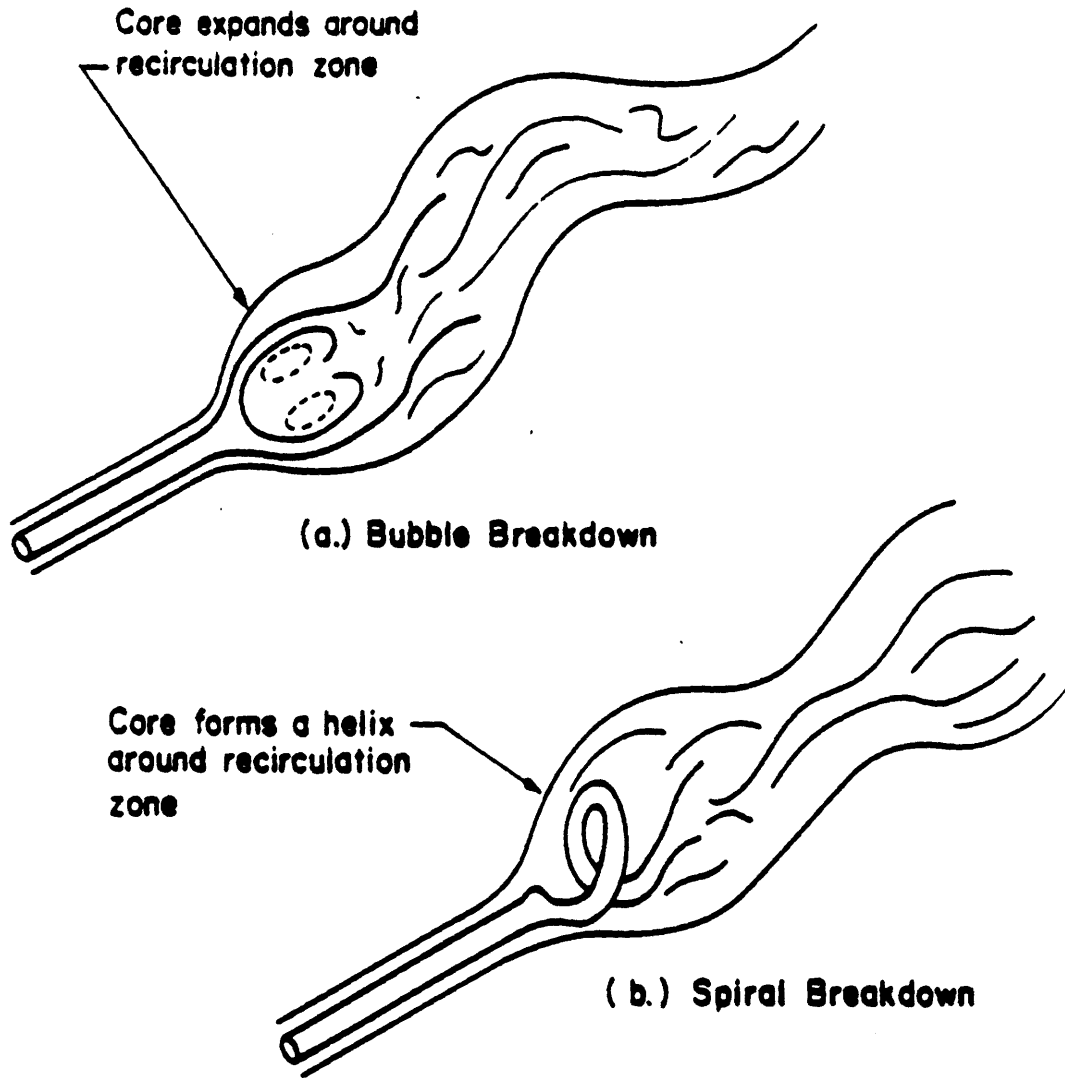
Figure 2.14: Types of vortex breakdown[25]

Chapter 3

Visualization Techniques

Three-dimensional visualization techniques have progressed greatly in the last few years. This progress stems from increased hardware capabilities and better algorithms. The introduction of graphics workstations, providing relatively affordable high-powered rendering and computational abilities, has been perhaps the greatest stimulus for the successes in scientific visualization. A wide variety of techniques are now available to many researchers. Even with these numerous tools, arriving at a complete understanding of a complex fluid flow is still a major undertaking. Often, researchers will stumble across interesting flow features. However, the more likely case is that many important features are never found. Even after a flow feature is located, the task of unde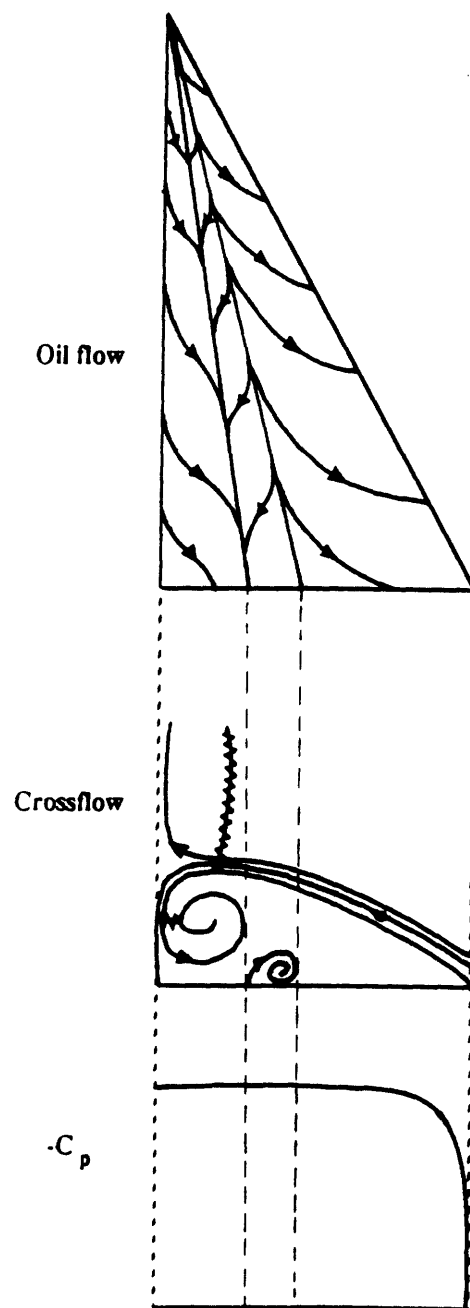rstanding how it was formed is still difficult. Before investigating a computation, a thorough knowledge of all the techniques available can save time and lead to a better understanding of the flow.

Visualization techniques may be classified according to their purposes. Figure 3.1 shows such a classification. First, the techniques have been divided into two main groups: static and dynamic techniques. Static techniques essentially do not allow the researcher any control over the information displayed other than the standard graphic functions of pan, zoom, and rotation of the rendered image. Domain surface rendering – coloring the body or preselected coordinate surfaces according to pressure, for example – is a static technique. A dynamic technique in some way allows the user to interactively interrogate a flow field. A moveable cutting plane – a two-dimensional plane cutting through the domain – is a dynamic technique. The user may interactively scan the plane through the domain to search for important flow features.

Dynamic techniques may be broken down into three subgroups: indentification, scanning, and probing. Identification techniques attempt to locate flow features automatically by searching over the entire computational domain in some way. Thus, after

flow features have been isolated using these methods, other tools are then used for more in-depth investigation. Scanning techniques typically allow the researcher to interactively search the domain by varying a continuous parameter. A cutting plane, as defined previously, is a good example. Finally, probing techniques provide the user with highly localized, specific information from the data. For example, a point probe which returns a value from a specific location is a probing technique. This breakdown of dynamic visualization techniques is in some sense simply a reduction of dimensions. In other words, identification techniques are essentially three-dimensional, scanning techniques are two-dimensional, and probing are one-dimensional.

The VISUAL3 user-interface is set-up to reflect this dimensional, hierarchal approach. VISUAL3 has three main graphics display windows : one-, two-, and three-dimensional. The screen layout is shown in Figure 3.2. As indicated by their names, the main graphics windows are used to display 1-D, 2-D, and 3-D data concurrently. For example, suppose we wish to view a delta wing calculation. The 3-D window may start with a static rendering of the wing surface pressures. Next, a cutting plane of constant x may be positioned; the results of this cutting plane are then rendered into the 2-D window. Finally, a line probe in the 2-D window will result in an XY plot in the 1-D window displaying the variation of a scalar along the 2-D line. A detailed description of the VISUAL3 interface is given by Giles and Haimes[6].

When a data set is being viewed for the first time, an efficient plan of attack can save valuable effort. A logical approach would be to first use any identification techniques which are available. Then, proceed by scanning the areas where features have been detected with cutting planes or iso-surfaces. The final step of the flow field investigation would use probing tools for the finest detailed information. By employing this common sense, hierarchal visualization strategy, even large data sets can be interrogated with relatively high efficiency.

The remainder of the chapter focuses on describing the set of visualization techniques available in VISUAL3; some of these techniques are relatively mature and less description is provided for them. Others, especially the feature identification techniques, are more recent ideas and considerable attention is spent on their description. Also, many techniques have some novel features which, although simple extensions in general, con-

siderably enhance their usefulness. For reference purposes, many of the visualization terms used in this chapter are also briefly defined in the glossary in Appendix A.

The data set used in this chapter is a thin-layer Navier-Stokes solution of a hypersonic delta wing done by Lee[14][29]. The wing has a rounded leading edge with 70 degree sweep angle. The freestream conditions are $M_\infty = 7.15$, $Re_\infty = 5.85 \times 10^6$, $T_{wall} = 288$ K, and $\alpha_\infty = 30.0°$. The normal Mach number and angle of attack for this case are: $M_n = 4.16$ and $\alpha_n = 59.4°$. The data set contains just under 300,000 cells. The coordinate system is shown in Figure 3.3. A detailed analysis of the calculation is not included here; the data is simply used as a vehicle to describe the various visualization methods.

3.1 Static Techniques

3.1.1 Surface Rendering

Surface rendering is probably the easiest of all three-dimensional visualization methods. In this technique, a limiting surface is shaded according to some scalar variable. Surface rendering can give some topological information. For example, the pressure surface rendering on the wing will show the approximate location of vortices and shocks on the leeward side. Furthermore, surface rendering is one step away from the calculation of force and moment coefficients of the delta wing. Thus, some useful information may be gained by surface rendering; however, as a means to probe the flow, surface rendering is only a starting point.

3.2 Identification Techniques

Identification techniques examine the entire computational domain to locate features, thus, saving the researcher the effort of finding them. The first feature identification technique discussed is flow topology. The next two methods described, X-rays and clouds, are general in that they rely upon the user to describe what to look for (for

example, high areas of total pressure loss). The stimulus for them is a brief mention of the techniques in a paper by R. Löhner[17]. The fourth idea is a new shock finding algorithm.

3.2.1 Topology

A recent area of research in visualization is the use of topological descriptions in identifying flow features. Topological techniques require the location of singular and critical points of the velocity field from which separation surfaces, vortex cores, and other flow features may be identified and displayed. The most impressive work to date in flow topological visualization techniques are the results of Helman and Hesselink[8] and the group at DLR Institute in Germany[4].

A subset of a full topological description is the surface topology. Surface topology in experimental work is determine typically by oil flow patterns on a wing surface. Currently, surface topology is the only topological identification technique that has been implemented for this research. To simulate oil flows, surface pathlines are used. Pathlines are lines which are everywhere tangent to a given vector field (see Section 3.5.1). Surface pathlines are pathlines which are constrained to remain on a boundary surface. Surface pathlines are useful to simulate oil flows by using the skin friction vector (in the case of Navier-Stokes calculations) or surface streamlines using the velocity vector (in the case of Euler calculations). As seen in the discussion of various delta wing flow types in Chapter 2, surface flow topology can be extremely useful in locating separation, attachment lines, and sometimes shock positions. Thus, surface pathlines are an effective feature identification technique in vortical flows.

To illustrate surface pathlines, we will look at the oil flow lines on the leeward surface of the delta wing (Figure 3.4). The first line inboard of the leading edge is the primary vortex separation line; unlike sharp delta wings, primary separation is not fixed at the leading edge. The next line visible in the surface flow is the secondary vortex reattachment line followed by the secondary vortex separation line. Finally, on the symmetry plane is the primary vortex reattachment. Except for the primary separation location, this surface flow is the same as the description of section 2.2.10.

3.2.2 X-rays

X-rays are exactly analagous to the medical usage of X-rays. In medical imagery, as an X-ray beam travels through a patient, the beam loses energy through interactions with the matter of the patient's body. The ratio of initial to final intensity of an X-ray beam may be modelled by the following simple equation:

$$I(x,y) = I_1/I_0 = \exp\left(-\int_{z_0}^{z_1} \mu(x,y,z)\,dz\right) \tag{3.1}$$

where μ is an attenuation constant which varies with position[36]. The z-direction is assumed to be the ray direction. If the attenuation constant was zero along the entire ray path, then the ratio is one (i.e., no loss has occured). In the human body, bones have much higher attenuation constants than flesh; thus, an X-ray travelling through a bone suffers a much higher loss than one travelling only through flesh. Similarly, a ray which travels a greater distance through bone will also suffer a greater loss.

In flow visualization, the computational domain is analagous to the human body, and a flow scalar, such as total pressure loss, is essentially the attenuation constant. As an "X-ray" travels through the domain, it loses intensity according to the local attenuation constant, i.e., the local scalar value. Thus, similar to how X-rays in medicine highlight internal portions of the human anatomy, X-rays in visualization highlight internal flow features of the computation. In this implementation of X-rays, the attenuation constant is actually a function of the local scalar:

$$\mu(x,y,z) = f(s(x,y,z))$$

where s is a flow scalar, and f is a mapping function such that $0 \leq f \leq 1$. The initial step of the mapping is:

$$s' = \frac{s - s_{min}}{s_{max} - s_{min}}$$

where (s_{min}, s_{max}) are user-specified scalar limits. At this point, the mapping of s' to μ is performed. In this implementation of X-rays, three mapping functions are currently available:

1. Linear - this mapping is defined as:

$$f = \begin{cases} 0 & \text{if } s' < 0 \\ s' & \text{if } 0 \leq s' \leq 1 \\ 1 & \text{if } s' > 1 \end{cases}$$

2. Threshold - this mapping is defined as:

$$f = \begin{cases} 0 & \text{if } s' < 0 \\ s' & \text{if } 0 \leq s' \leq 1 \\ 0 & \text{if } s' > 1 \end{cases}$$

Although this mapping is similar to the linear mapping, the scalar variables greater than s_{max} will not contribute any loss to an X-ray. This is helpful when the user strictly wishes to view the effect of a certain range of the scalar variable.

3. Midpoint - this mapping is defined as:

$$f = \begin{cases} 0 & \text{if } s' < 0 \\ 1 - 2|s' - 0.5| & \text{if } 0 \leq s' \leq 1 \\ 0 & \text{if } s' > 1 \end{cases}$$

The midpoint mapping is useful when examining the range around a particular scalar value, i.e., the midpoint, and equal weighting is desired on either side of the midpoint.

The mapping functions provide additional freedom when determining how to highlight a particular range of a scalar variable. Additional mapping functions can be easily implemented if the situation arises; for example, one could construct a routine that allowed the user to interactively generate a mapping function. Thus, an X-ray can be tailored to meet the specific needs of the particular circumstance. Care must be taken, however, when using various mapping functions because the resulting X-ray could be confusing.

When an X-ray is taken, rays which travel into the screen (i.e. along the positive z-axis in screen coordinates) are issued from a gridded plane. The user may interactively set the view before taking an X-ray. Furthermore, the user also controls the X-ray grid density. The current capability is up to a grid 320 by 320 of X-rays. Also, X-rays

may exit and then re-enter the domain analagous to an X-ray exitting and re-entering a body. If this occurs, no loss is accumulated while the X-ray is outside the domain. For a description of the X-ray algorithm, see Appendix B.

To illustrate the use of X-rays in feature identification, an X-ray using helicity will be taken looking in the x-direction over the leeside of the wing. This view should identify the vortical regions of the flow field. The linear mapping is used; thus, red portions of the X-ray represent regions of high helicity and blue portions represent regions of low helicity (see Figure 3.5). The primary vortex is the blue-green area at the bottom left. The secondary vortex is the red area along the bottom. Note how the secondary vortex appears to spread towards the right much more than the primary vortex. This effect is because the primary vortex is nearly aligned along the x-axis (i.e., the X-ray direction) while the secondary vortex is not. The large red region above the vortices is probably the portion of the flow just above the shear layer which would have a positive helicity. Finally, a crossflow shock nearly parallel to the symmetry plane can also be seen in the X-ray as the rapid change in intensity from yellow to green.

3.2.3 Clouds

Clouds are shrunken thresholded cells. If a cell-average scalar quantity falls between a user-controlled minimum and maximum, a percentage of the cell is rendered. The resulting display reveals which areas of the flow have features of possible interest (for example, high total pressure loss). Furthermore, several, additive threshold limits may be applied to clouds (For more on thresholding, see Section 3.4.4). Thus, features may be filtered so that the resulting display shows only pertinent information. An example of the usefulness of multiple thresholding occurs in the Navier-Stokes solution over a delta wing. If we are interested in where the leading edge vortex is, thresholding high values of total pressure loss will display the vortex and also the boundary layer. Additional thresholds may be applied to remove the boundary layer from the display; for example, an additional threshold on speed or Mach number could be performed to eliminate the near zero velocity in the boundary layer leaving only the vortex visible. However, the thresholds must be applied without losing the primary feature of interest in the process.

Clouds may also be used to display the quality of a unstructured grid. A fractional size of the cells are rendered according to a user-set parameter between 0 and 1. A value of one renders the cell at its actual size; a value approaching zero causes the volume of the cell rendered to approach zero. Rendering only a fraction of the cell creates the desired cloud effect where the "drops" are shrunken cells. This technique for rendering gives the user information on the quality of the grid by displaying cell size in areas where the flow features are interesting. Clouds can be effective in viewing a grid even before a calculation. Thresholding by a spatial coordinate will display the grid only in the specified range. Thus, an entire unstructured grid may be scanned by simply varying the spatial coordinate thresholds. For a description of the algorithm, see Appendix C.

In the hypersonic data set, the bow shock will cause significant total pressure losses thus obscuring most of the additional total pressure loss from any vortical regions in the flow. However, a total pressure cloud can still be useful as a starting point. Figure 3.6 is total pressure loss cloud with a threshold range of (0.92,1.0). The image is rendered by total pressure loss also. The red region on the upper surface of the delta wing is the separated flow region. Another important feature of the cloud is the loss region along the symmetry plane; this area is probably behind a crossflow shock that runs parallel to the symmetry plane. The fraction of the cell rendered in this figure is 0.1. This small value is needed to be able to see in the interior of the domain otherwise larger cells would completely hide anything behind them; as it is, this image is hard enough to understand. However, an additional threshold can greatly relieve the difficulties.

Perhaps clouds most powerful feature is the ability to perform multiple thresholds. For a second threshold, helicity will be used. Figure 3.7 shows the negative regions of helicity shaded by Mach number (high Mach is red, low blue). The primary vortex can clearly be seen now as the area of high Mach number (yellow and red shading). The separation location can also be seen on the upper surface slightly inboard of the leading edge where the region of negative helicity clouds emanates from the wing surface. Notice that the Mach number in the separated flow near the surface is low, and that as the separated flow becomes entrained by the vortex, the Mach number increases. This image also effectively displays the sheet-like nature of the vortical flow on the wing's leeside.

41

3.3 Shock Finding

Shock detection in three-dimensional flows is extremely difficult. However, shocks play an important part in vortical flows often causing separation and the formation of a vortex. Shocks are also important in many transonic and supersonic flows. The ability to automatically detect shocks can be a significant aid in complex flows.

To identify a shock, the first step is to determine the normal direction to the shock. Across a shock, the tangential velocity component does not change; thus, the gradient of the speed at a shock will be normal to the shock. The exact location of a shock is then determined by calculating the magnitude of the Mach vector in the direction of the speed gradient at all points in the domain. We define the normal Mach number to be the opposite of the Mach vector dotted into the speed gradient. Thus, a positive normal Mach number indicates streamwise compression and a negative normal Mach number indicates streamwise expansion. If this value is positive one, then a shock has been found (or an isentropic recompression through Mach one). The entire surface where the normal Mach number is positive one is then displayed. Typically, a little additional thresholding is needed to eliminate some stray portions of the flow field where the normal Mach number happens to be one.

Having calculated the speed gradient, its magnitude normalized by the local speed is often an effective threshold variable. For two shocks with the same incoming speed, the speed gradient will be larger in the stronger shock. To compare shocks with different incoming speeds, the speed gradient must be normalized and the logical choice is the local speed. Thus, the normalized speed gradient is a measure of shock strength and can effectively be used to threshold shocks of varying strengths.

Figure 3.8 is the result of the shock finding algorithm viewing the wing from behind looking upstream. The bow shock and two crossflow shocks are visible. The shock surfaces are rendered by the magnitude of the speed gradient with yellow being high and blue being low values. As discussed in Section 2.2.10 of hypersonic delta wing flows, the first crossflow shock is necessary to turn the flow along the symmetry plane. The second crossflow shock is required to turn the flow entrained by the vortex as it heads toward the wing surface. The bow shock is the strongest shock. Surprisingly, the crossflow

shock which is parallel to the symmetry plane is relatively weak; the small crossflow shock perpendicular to the symmetry plane is even stronger. Also, notice the strange shock structure of the first crossflow shock at the trailing edge. Looking back at the total pressure loss clouds in Figure 3.6, a enlarged region of total pressure loss can also be seen at the trailing edge. It is possible that these two features are related to problems with the downstream boundary condition. The detection of this downstream boundary problem highlights the usefulness of feature identification techniques in debugging a code.

Finally, we view the shocks from the front of the wing with a portion of the bow shock thresholded away by shock strength (Figure 3.9). The bow shock is extremely strong at the wing tip and near the leading edge. At this point, further investigation of the shock and vortex system would be done with the other dynamic visualization techniques.

An unusual feature of the shock finding results is the apparent double-valued nature of the two crossflow shocks. In other words, the normal Mach number is positive one at two points in the shock. To analyze this result further, we plot the variation of normal Mach number along a streamline through the first crossflow shock in Figure 3.10 (see pathline probe description in Section 3.5.2). The normal Mach number just ahead of the shock is negative; thus, the flow is expanding before the shock. At the shock, the normal Mach number must jump above one because the speed gradient changes sign as the flow switches from expansion to compression. Then, as the shock compresses the flow, the normal Mach number passes through one again and generally will be near zero or negative indicating expansion. Thus, the streamwise variation of normal Mach number is double-valued through the shock. In reality, the true definition of a shock is where the first derivative of a flow quantity is large and the second derivatives are zero. A shock always contains an inflection point and thus the second derivatives will be zero at some point in the shock. Thus, an improvement upon the shock finding algorithm would be to display an iso-surface of the second derivative of the speed in the direction of the first derivative of the speed. Then, thresholding away low values of the speed gradient magnitude will eliminate the freestream portions of the iso-surface[5].

43

3.4 Scanning Techniques

Scanning techniques, although still relatively recent developments, are much more estab-
lished than feature identification techniques. This set of methods allows the researcher
to scan through the domain either spatially or through scalar values. Some additional
techniques, such as contours, tufts, and thresholding, although not truly scanning tech-
niques, are used so often in conjunction with scanning methods that they are also
described in this section.

3.4.1 Cutting Planes

Cutting planes are planar surfaces which slice through the computational domain. The
scalar values at the nodes of the cut cells are interpolated onto the planar surface
and then rendered in two-dimensions. The plane may then be scanned in its normal
direction allowing the user to investigate the entire domain if necessary. The plane
normal direction, location, and size may be interactively set by inputs to the dialbox
(a pathline cutting plane positioning tool also exists and is described in Section 3.5.2).
A very efficient algorithm for unstructured grid cutting planes has been successfully
implemented by Giles and Haimes[6]. Figure 3.11 shows the cutting plane positioned
at about 75% chord with its normal in the x-direction and Figure 3.12 is the two-
dimensional display of the plane in the 2-D window rendered with temperature. Both
primary and secondary vortices and all of the shocks can be seen in this plane. The
plane may then be scanned to gain further insight into the flow field.

3.4.2 Contours

Contours are lines of constant scalar value and are very useful in the rendering of scalar
distributions. Typically, several contours over a range of scalar values are rendered.
Coloring indicates their exact scalar value and the closeness of consecutive contours
indicates the scalar gradient. In areas of high gradients, several contours will be close
together. Figure 3.13 is the same cutting plane at 75% chord rendered by temperature
but this time with contours. The various shocks are much more visible now because the

contours bunch together near them. Also, the shear layer and the expansion process around the leading edge are much more evident as is the windward surface boundary layer adjected to the cooled surface. Comparison of Figure 3.12 and 3.13 serves to highlight that contouring is often much more effective than the usual Goraud shading. The drawback of contours is that they generally require more rendering time than Goraud shading and, therefore, are less interactive.

3.4.3 Tufts

Tufts are small vectors whose direction and size represent the vector field, which is typically the velocity vector. A regular grid of points on a cutting plane defines where the tufts are displayed. The projection of the tufts appears on the cutting plane. The three-dimensional view shows the tufts in their true position. A slight variation places tufts only at the intersection of the cutting plane and a computational cell edge. This option limits errors arising from interpolation. Depending on the specific use of tufts, either method may prove more adequate. For example, when looking at boundary layer velocity vectors, a regular grid of points on the cutting plane will place equal amounts of tufts in the streamwise direction as in the boundary normal direction. This grid of tufts wastes effort in the streamwise direction along which gradients will be low. The computational grid, having been set-up for efficient calculation, probably has more nodes in the normal direction than in the streamwise direction. Thus, in this example, the computational cell edge method is best. As a counter example, suppose we wish to view the leeside of a Navier-Stokes delta wing and are interested in the general structure of the vortices. In this case, using the computational grid is inefficient because many nodes are packed extremely close to the wall which will not be recognizable when rendered at the scale of the wing span. Thus, in this example, a regular grid of tufts is the best method.

The difficulty with tufts is that their projection on the cutting plane depends on the plane's orientation and, in three-dimensions the tufts can be very misleading depending on the current viewing angle. To illustrate the problem, two different cutting planes are used with tufts rendered by temperature. The first plane is the same plane of constant x used previously. The tufts for it are shown in Figure 3.14. The other plane is essentially

in the same position except normal to the leading edge (i.e., the plane's normal is in the leading edge direction). Figure 3.15 shows the second plane's tufts. The differences are obvious and highlight the difficulties with tufts. The center of the primary vortex is in different positions. The secondary vortex does not appear at all in the second rotated plane. Also in the rotated plane, the symmetry plane condition does not appear to have been enforced at all. When using the three-dimensional view of tufts, the best approach is to rotate the plane to view the tufts pattern from a number of different angles. A typical three-dimensional view of tufts is shown in Figure 3.16. Also, tufts are even more effective when used as the cutting plane is scanned. This combination of scanning with tufts active is useful in obtaining a 3-D sense of the vector field.

3.4.4 Thresholding

Thresholding limits the displayed portion of a surface by only rendering those parts of the surface whose scalar values fall within a user-defined range[37]. For example, using the same cutting plane as before, thesholding could be used to only display the plane where the total pressure loss is between 0.92 and 1.0. By doing this on several planes, a picture revealing some of the three-dimensional nature of the flow field may be constructed. Figure 3.17 is an example which does exactly that. The display variable is helicity. The primary and secondary vortices can be clearly identified (highlighting one of the advantages of helicity). Thresholding several planes like this is similar to clouds. Depending on the particular flow field, either technique may be more preferred. The advantage of clouds is that it scans over the entire domain while the thresholded planes only scan a few planes of the computational domain. However, this is often adequate and the information provided by thresholded cutting planes is often more readily understandable. The best bet is to experiment with both techniques.

3.4.5 Iso-surfaces

Iso-surfaces are three-dimensional surfaces of a constant scalar value. In reality, cutting planes are simply the geometric subset of iso-surfaces where the constant value parameter is a geometric coordinate. The shock finding technique uses the iso-surface of normal

Mach number equal to positive one. A difficulty with iso-surfaces is that, especially in vortical flows, they tend to be extremely complicated and are often meaningless. However, in internal flows, iso-surfaces of pressure are often very informative and can help determine exit pressure effects on the internal flow. Iso-surfaces, for this case, are particularly helpful when scanned slowly through a pressure range. The scanning of pressure iso-surfaces is an effective method for visualizing three-dimensional pressure gradient fields since each consecutive surface represents a small change in pressure from the previous surface. Thus, in areas where gradients are locally high, consecutive iso-surfaces will essentially maintain the same shape. Similarly, in areas where the gradients are low, consecutive iso-surfaces will displace considerably and change a large amount.

3.5   Probing Techniques

Probing methods, the final type of visualization technique, provide the most localized information. These tools are primarily used in the final step of investigating a flow feature to gather quantitative information such as the pressure distribution on a surface, or velocity profiles in boundary layers. The techniques described in the rest of this section rely upon having a two-dimensional plane; we will use the cutting plane at 75% chord for examples (see Section 3.4.1).

3.5.1   Path-related Methods

Pathlines

Pathlines are lines through a vector field which are everywhere parallel to the local vector at an instant in time. Typically, streamlines (i.e., pathlines of the velocity vector field) are used and are an excellent means for visualizing vortical flows. In a steady flow, they coincide with the path a particle would follow when released from some location. In unsteady flows, streamlines and particle paths are different. The calculation of pathlines for steady flows amounts to integrating:

$$\frac{d\vec{x}}{dt} = \vec{f} \tag{3.2}$$

47

where $\vec{x}$ is the position in space and $\vec{f}$ is a vector field. The integration technique is the adaptive numerical integration described by Giles and Haimes[6].

A powerful feature of the VISUAL3 implementation of pathlines is the method of spawning them. Pathlines require a unique point in the three-dimensional data set from which to begin the integration either backwards or forwards through the vector field. This point is set by using cutting planes. First, a cutting plane is set-up in the domain. The user may then position the cursor using the mouse at any spot on the two-dimensional cutting plane. At the desired location, the user hits a mouse button and the pathline is spawned. This spawning method allows the user complete freedom in spawning pathlines anywhere in the flow field (e.g., from the center of a vortex). Furthermore, the pathline implementation is truly a probe because the cursor may be moved interactively. Thus, the user can probe a region dynamically with the pathline probe. When a pathline of interest is located, a press of a mouse button will store the streamline for permanent use. This interactive pathline probe (called a streamer in VISUAL3) is extremely effective in understanding localized areas of the flow.

Figure 3.18 shows several streamlines spawned from the 75% chord cutting plane. The streamlines have been integrated backward to their origin at the upstream boundary and forward to their exit location at the downstream boundary. They are shaded by Mach number. The streamline near the symmetry plane is approximately the axis of the primary vortex. The other three streamlines show the flow as it travels around the leading edge. The drastic change in Mach number and in the direction of the streamlines underneath the wing is caused by the bow shock.

Ribbons

Ribbons are pathlines that have been given some width. Many implementations of ribbons calculate two pathlines with the second pathline constrained to remain a constant distance away from the original pathline[34][10][32]. This method can be troublesome because as the second pathline diverges from the initial pathline, the resulting ribbon becomes a less accurate representation of the local twist. Furthermore, in a highly sheared flow when using the velocity vector field, neighboring streamlines may have

large velocity differences causing the slower streamline to require many more time steps before completing the integration. The construction of triangles forming the ribbon surface will also be extremely difficult in a shear flow because the slower streamline will contain many more points. The end result is the need for a complicated algorithm to build ribbon surfaces. The approach here is slightly different. One edge is the true pathline, the other edge is contructed by rotating a constant length normal vector about the path according to the local pathwise angular rotation rate. The result is a ribbon whose twist reflects the pathwise curl of the vector field of the flow. For streamribbons, the ribbon twist reflects the streamwise vorticity. The equation which describes the rotation of the pathline normal is:

$$\frac{d\theta}{dt} = \frac{1}{2}(\vec{\omega} \cdot \vec{s})$$

$$\vec{s} = \frac{\vec{f}}{|\vec{f}|} \tag{3.3}$$

$$\vec{\omega} = \nabla \times \vec{f}$$

where θ is the current angle of the normal with respect to its initial direction. The factor of $\frac{1}{2}$ is needed because the angular rotation rate is half the curl of the vector. Equations 3.2 and 3.4 are then integrated simultaneously. The final step is choosing an initial normal direction. Initially, this is done automatically; however, the user may rotate this position interactively and thus rotate the entire ribbon. This rotation feature is extremely helpful in determining exactly how and which direction a ribbon twists. Furthermore, this method of ribbon calculation avoids the problem of constraining a second pathline and is extremely easy to implement in comparison.

Figure 3.19 is the streamribbon equivalent of Figure 3.18. The white edge of the ribbons is the true streamline. Again, the shading is by Mach number. The rotation of the primary vortex can be clearly scene. Furthermore, the three streamlines near the leading edge have very little rotation except near the bow shock. This figure shows the power of streamribbons extremely well. In one image, the stream paths, the local rotation, and the variance of a scalar can be clearly depicted. This same effect using streamlines would require twice as many lines and clutter the image often creating interpretation difficulties.

Streamtubes and Rakes

Streamtubes are the surface formed by every streamline which passes through a given closed curve[1]. A analagous definition exists for tubes of other vector fields. Streamtubes are useful in visualizing the expansion of a flow field. The difficulty with constructing a streamtube is that they frequently diverge such that connecting adjacent streamlines to form a surface is nearly impossible. Instead of trying to construct a surface, VISUAL3 constructs streamtubes by simply specifying a circle on a two-dimensional cutting plane and then calculating a user-defined number of pathlines spawned from equidistant points around the circle. This gives the same effect of a streamtube surface with much less trouble. A true streamtube is still desirable; however, an easy and efficient algorithm needs to be developed before streamtubes or streamsurfaces will become standard visualization methods. A rake is very similar to a streamtube except the circle is now a line. The user may position a line on the two-dimensional cutting plane and then view any number of pathlines starting from that line at equidistant intervals.

The image in Figure 3.20 is a streamtube in the primary vortex rendered by Mach number. The two interesting features to note are the extreme inboard position of the primary vortex and the slow growth of the vortex as it progresses downstream. Also, the tube is an effective means to visualize vortical motions because the helical nature of the flow can be quite clearly seen.

Animation

Pathline animation is a simple yet effective technique which provides the researcher with a dynamic display of a vector field. During animation, small particles travel downstream along the current set of pathlines in accordance with their local speed; the effect dynamically reveals the relative speed of various pathlines and is extremely useful for building an intuitive understanding of the flow field.

3.5.2 1-D Probes

The final set of probing techniques, 1-D probes, although simple, are extremely powerful for detailed examination of the flow field. VISUAL3's cursor mapping ability is a particularly useful extension of 1-D probes. The cursor mapping allows the simultaneous display of the current cursor position in the one-, two-, and three-dimensional views. The usefulness of cursor mapping will be further highlighted in the following descriptions of the various 1-D probes. For some of the probes, examples are omitted because their uses are relatively obvious and also tend to be more effective in dynamic use rather than in a static image.

Point Probe

The point probe has two major functions: the local scalar value is displayed in a text window, and the local vector is projected on the two-dimensional plane. As a result of the cursor mapping function discussed earlier, this also displays the local vector in the three-dimensional window.

Line Probe

A line probe displays the variation of the scalar value upon a line on the two-dimensional plane. This probe can be useful in finding the variation of scalar across a shock or through the core of a vortex. Figure 3.21 shows the entire screen when a line probe is active. The line has been placed at the small crossflow shock which is perpendicular to the symmetry plane. The bottom right corner of the figure shows the variation of the pressure along the line. The shock is clearly seen in the plot as the abrupt increase in pressure. The vertical line in the 1-D window indicates a position which is in turn echoed in the 2-D and 3-D displays as a result of the cursor mapping. Since the point probe is also active, the local velocity vector is also displayed (the blue vector in the three-dimensional window).

Boundary Edge Probe

The boundary edge probe plots the variation of a scalar along a boundary surface. An example is the pressure coefficient distribution on the surface. Figure 3.22 shows the pressure coefficient surface distribution at 75% chord. The leeward surface is nearly at the vacuum limit which is $C_p = -0.0274$. The large expansion around the leading edge can also be seen in the plot.

Boundary Layer Probe

The boundary layer probe plots the variation of a scalar along a direction normal to a boundary surface. The normal may be interactively positioned anywhere on the boundary surface by moving the cursor in the 2-D window. This probe is effective for, as the name indicates, investigating boundary layer effects. On the wing's windward side, the boundary layer is attached and extremely thin. Across boundary layers, especially thin boundary layers, the pressure is nearly constant. Since the calculation uses the ideal gas law as its state equation, constant pressure implies that the temperature and the density must be inversely related across the boundary layer. To check this, a boundary layer probe is used on the windward surface at 75% chord and approximately 50% span. Figure 3.23 and 3.24 are the boundary layer variation of density and temperature respectively. The variations can clearly be seen to have an inverse behavior as expected.

Pathline Probe

The pathline probe displays the variation of a scalar along a pathline. The cursor mapping ability allows the pathline probe to pinpoint the exact location of unusual pathwise behaviors. The pathline probe was already used in Section 3.3 to display the variation of normal Mach number along a streamline. An additional feature is the ability to use the pathline probe to position a cutting plane. When the probe is on, the cutting plane may be placed at any location on the current pathline with the plane normal being the local path-direction at the cursor location. Using this tool, a cutting plane can be easily placed at a shock or any other interesting feature along the pathline.

Again, the 75% chord cutting plane will used to begin. A streamline in the core of the secondary vortex is spawned and the pathline probe is activated. The plot (Figure 3.25) has an amazing amount of information. Near the beginning of the streamline, the Mach number drops rapidly from the freestream 7.15 to approximately 2.6 as a result of the bow shock. There is some further compression before the flow rapidly accelerates to Mach 4 as it rounds the leading edge. At about $x = 0.2$, the Mach again drops; this compression is from the first crossflow shock which is approximately parallel to the symmetry plane. Then, another acceleration occurs as the flows turns downward toward the wing at the symmetry plane. Here, it encounters the crossflow shock perpendicular to the symmetry plane. Finally, the streamline becomes a part of the secondary vortex as it heads outboard from the influence of the primary vortex pressure gradient. Figure 3.26 is the three-dimensional view of the streamline looking down from the wing tip; the streamline is shaded by Mach number.

Dynamic

X-rays — Topology — Shock Finding — Clouds   *Identification*

Cutting Planes
- Thresholding
- Contours
- Tufts

Iso-surfaces
- Thresholding

Scanning

1-D Probes
- Surface Layer
- Pathline
- Point
- Line
- Edge

Pathlines/Ribbons
- Streamtubes & rakes
- Animation

Probing

Static

(Surface Rendering)
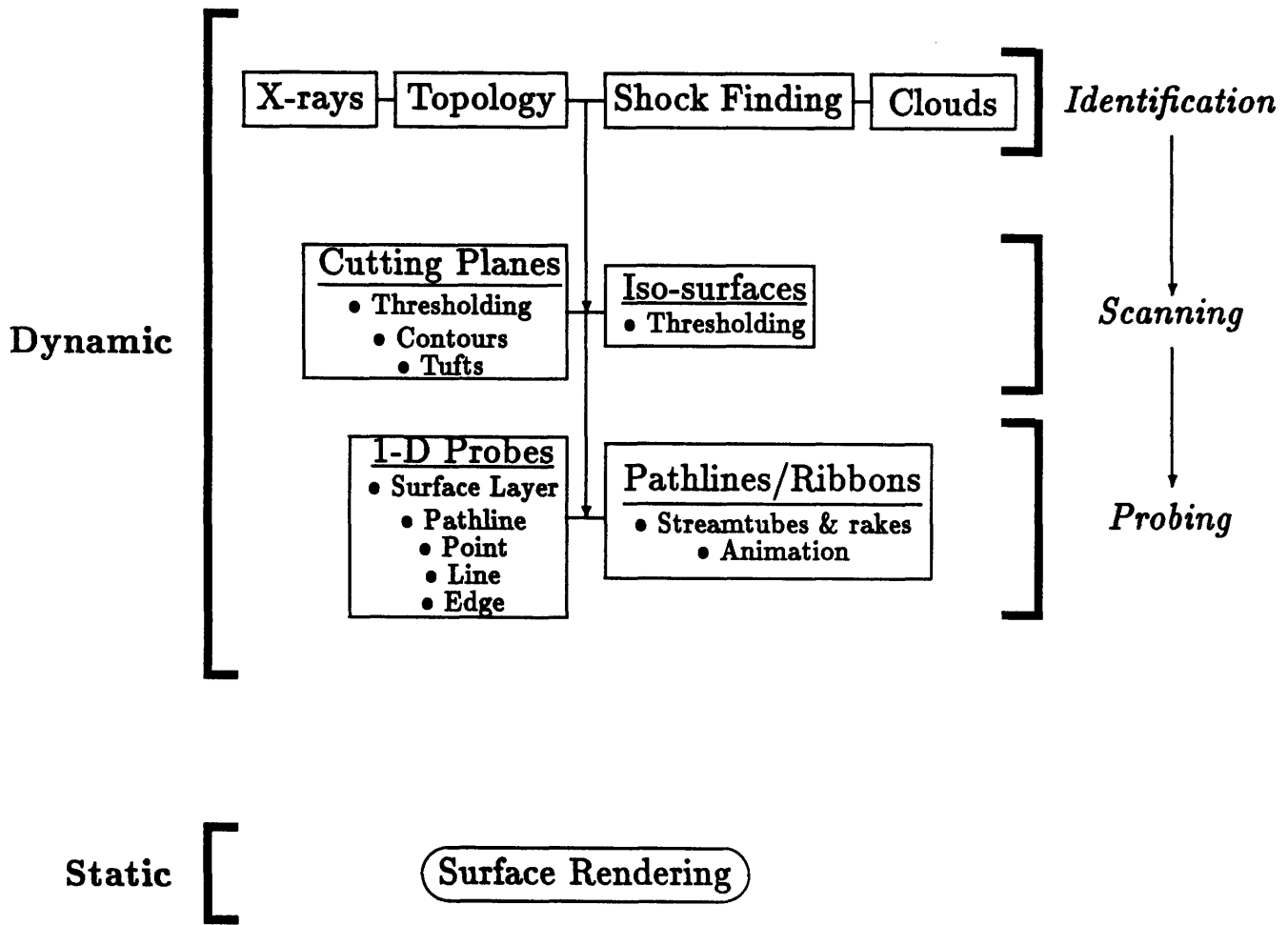
Figure 3.1: Visualization Technique Classification
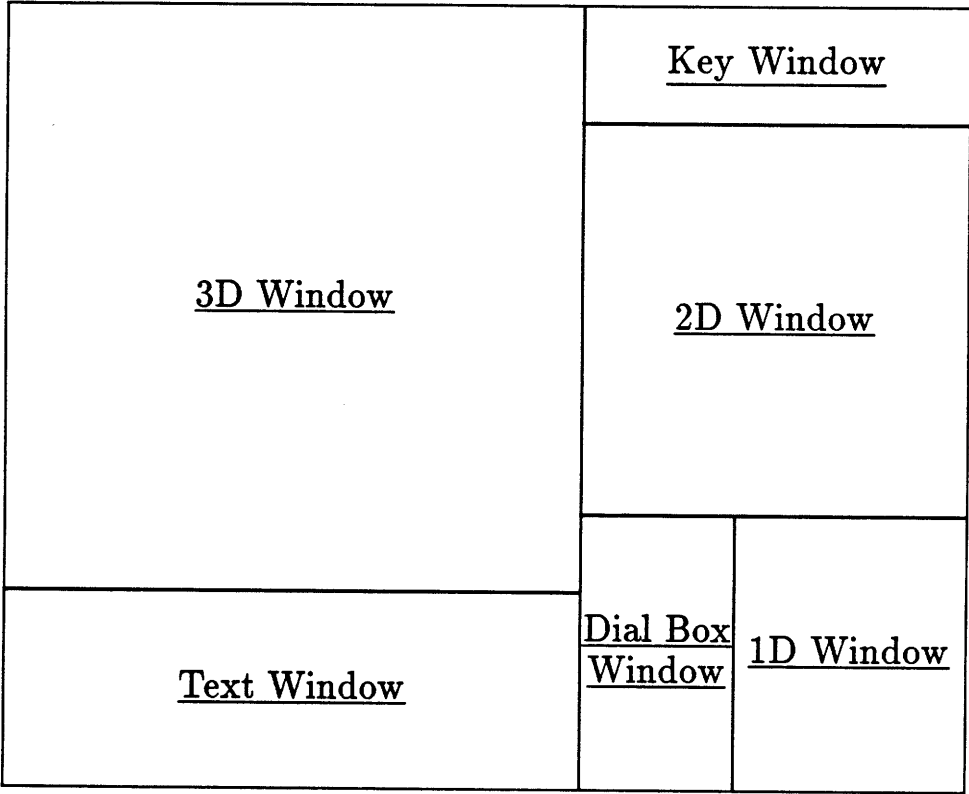
Figure 3.2: VISUAL3 screen layout[7]
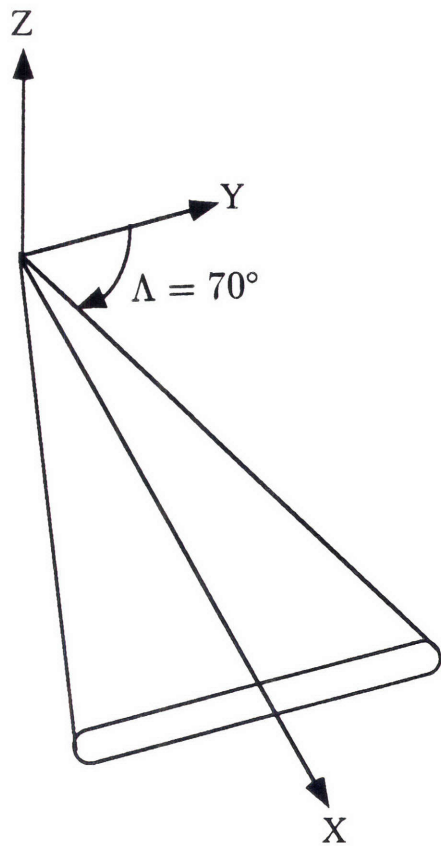
Figure 3.3: Coordinate system for Lee delta wing calculation
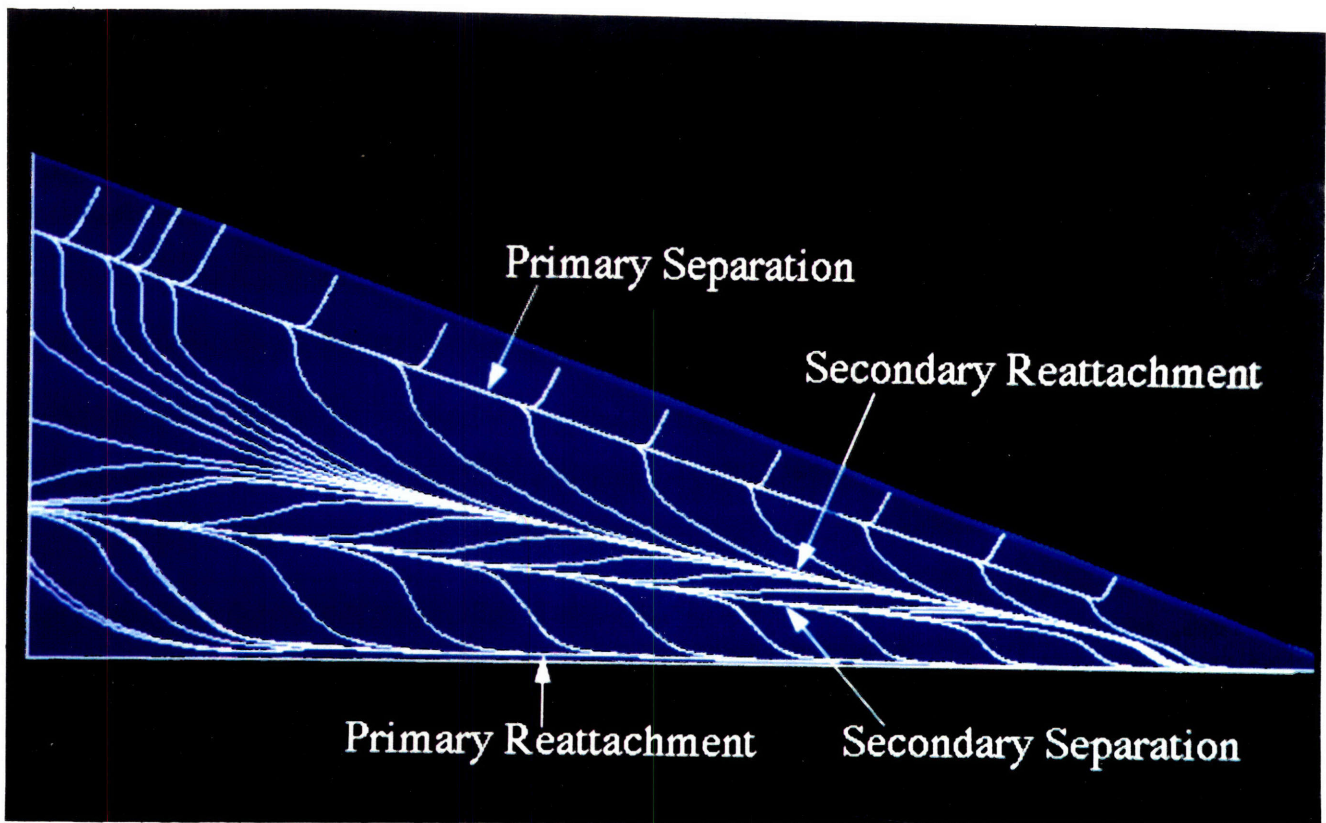
Figure 3.4: Surface pathlines simulating oil flow patterns
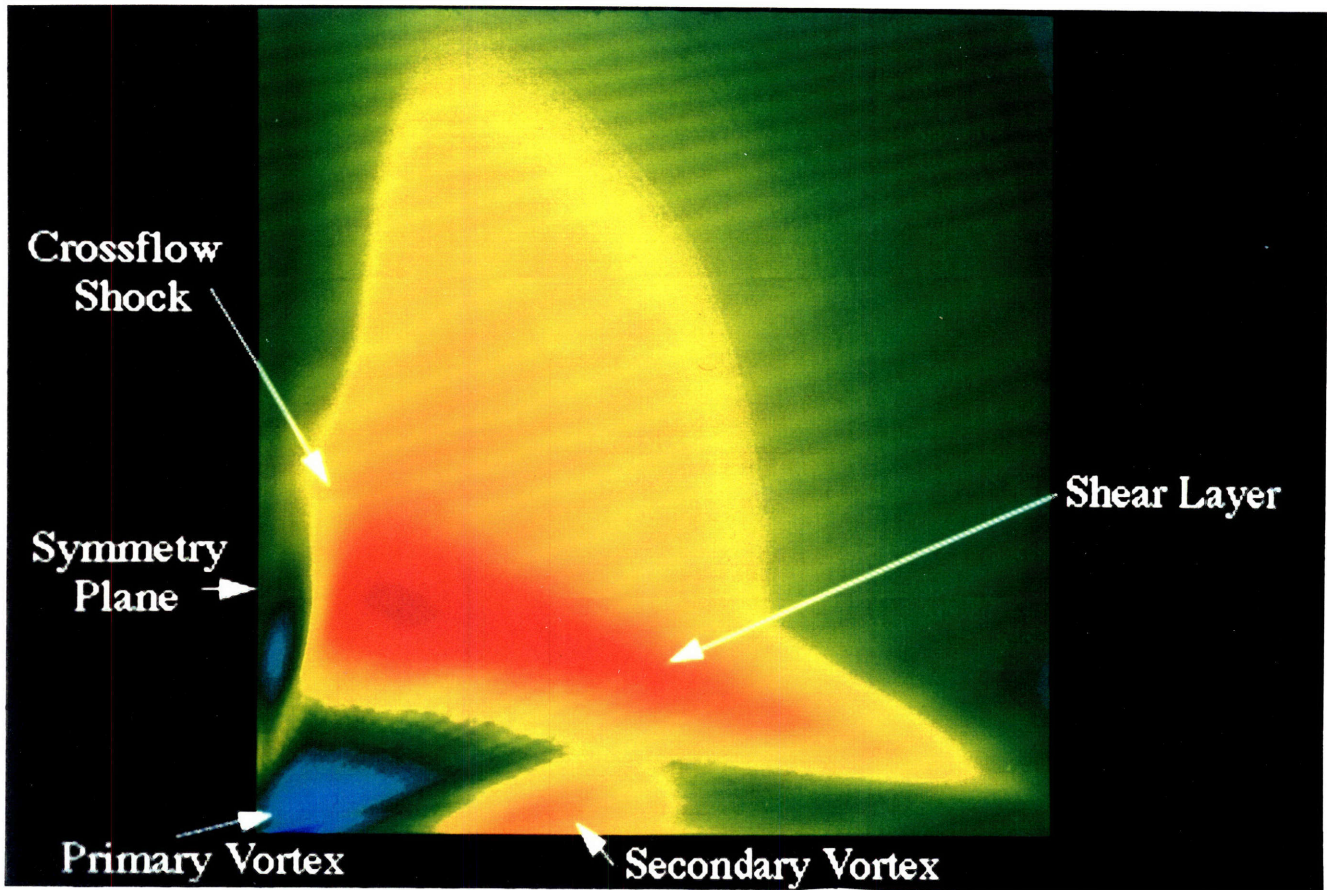
Figure 3.5: X-ray of helicity along x-axis
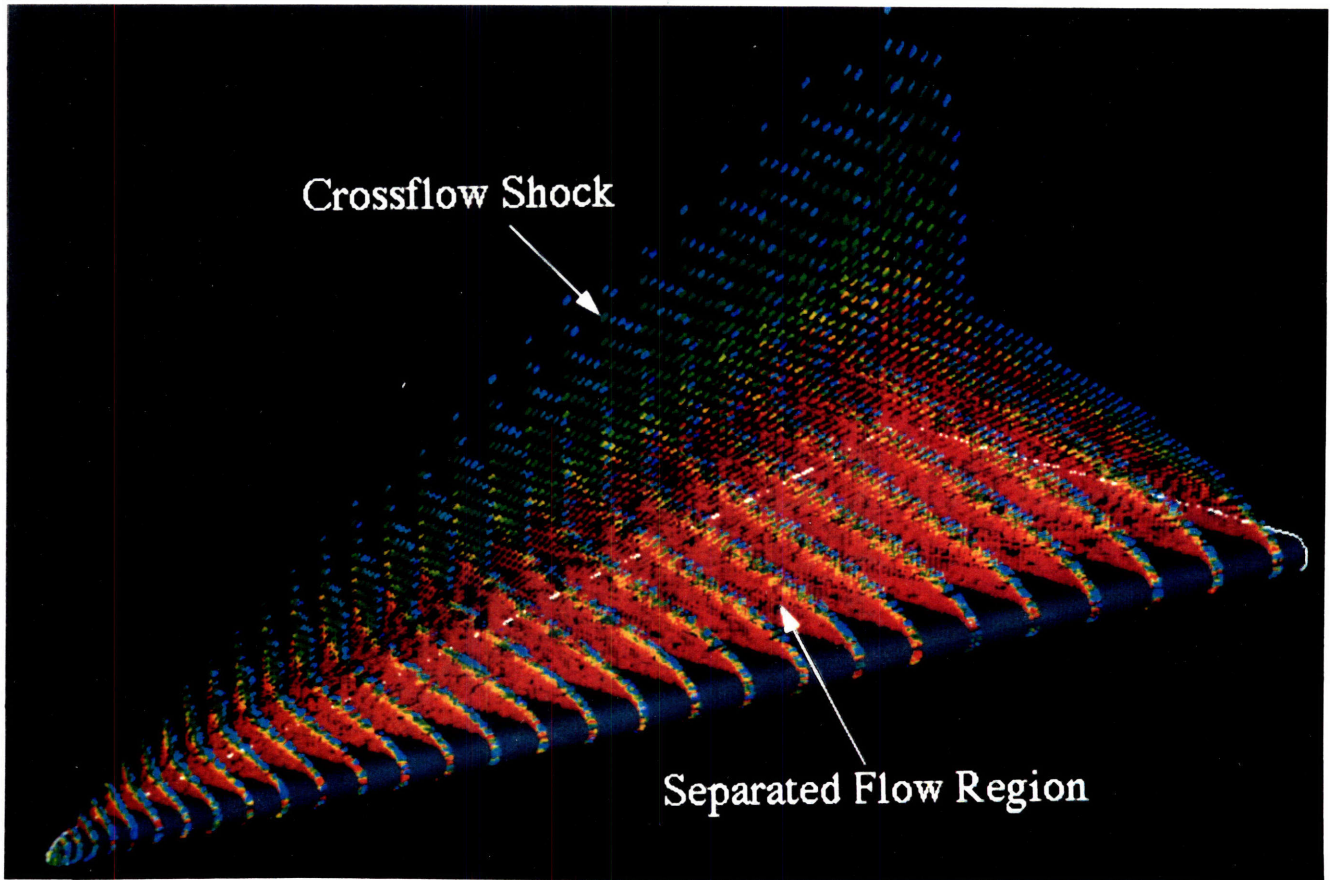
Figure 3.6: Total pressure loss cloud rendered by total pressure loss
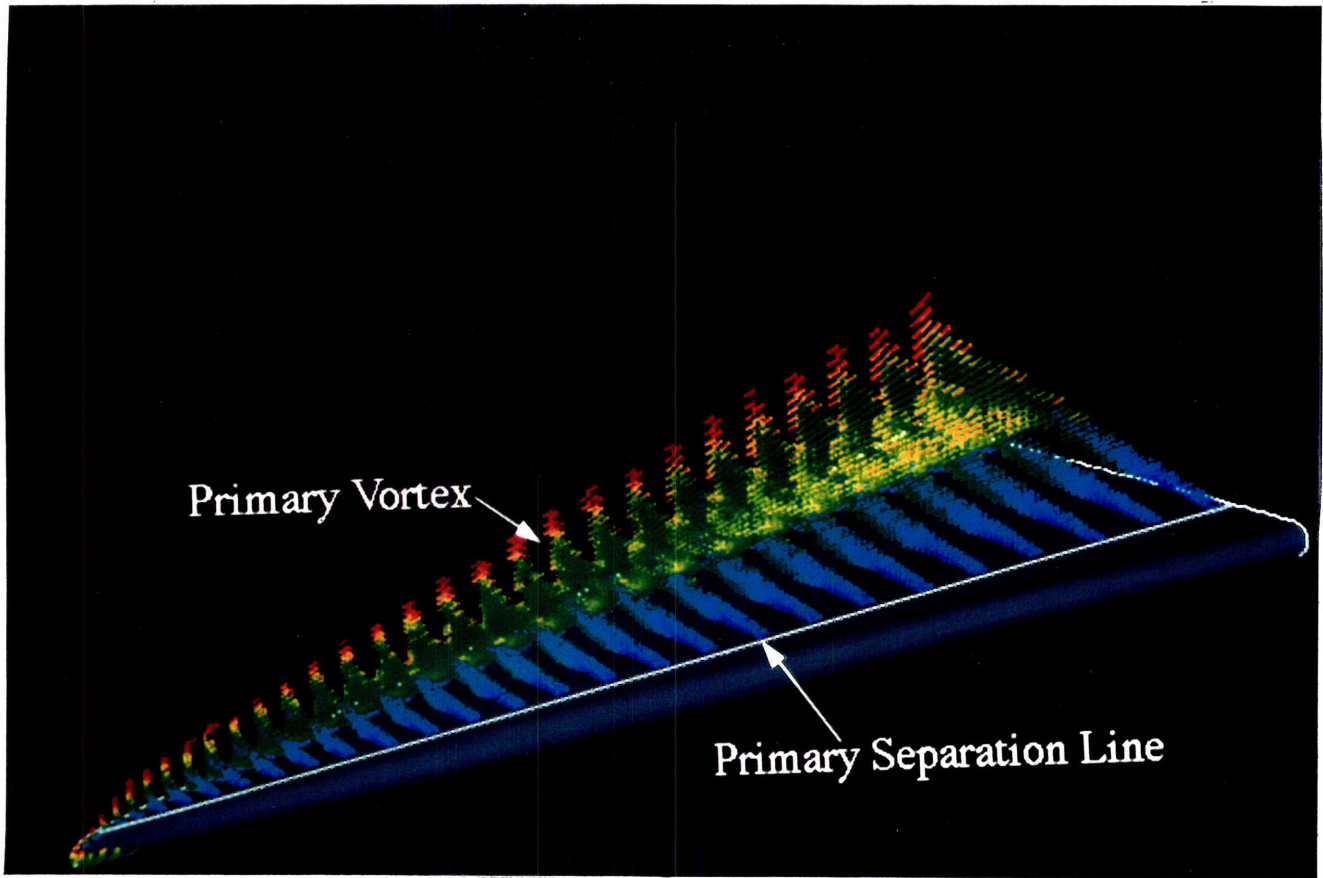
Figure 3.7: Multiple threshold cloud rendered by Mach
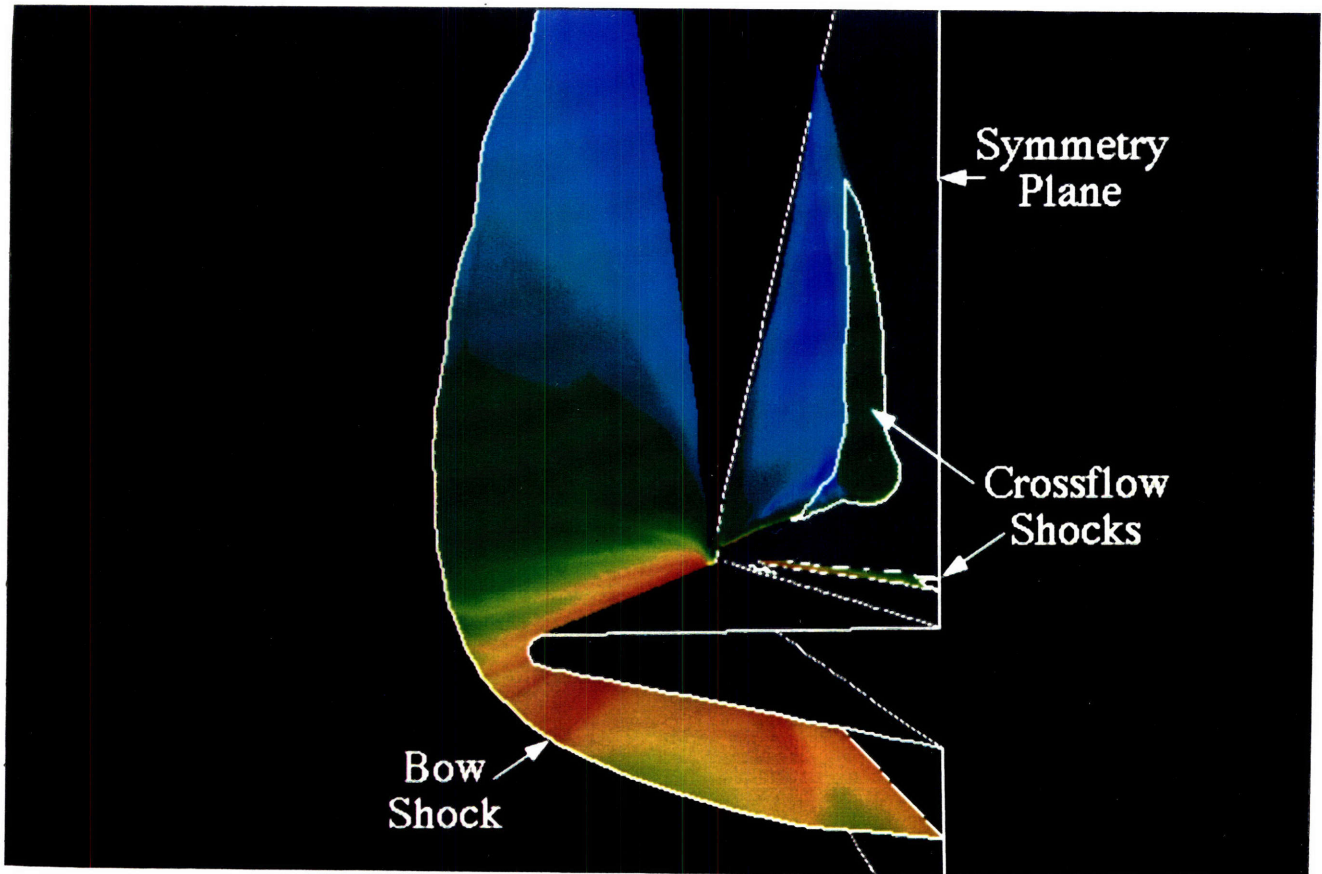
Figure 3.8: Shock surfaces viewed from trailing edge
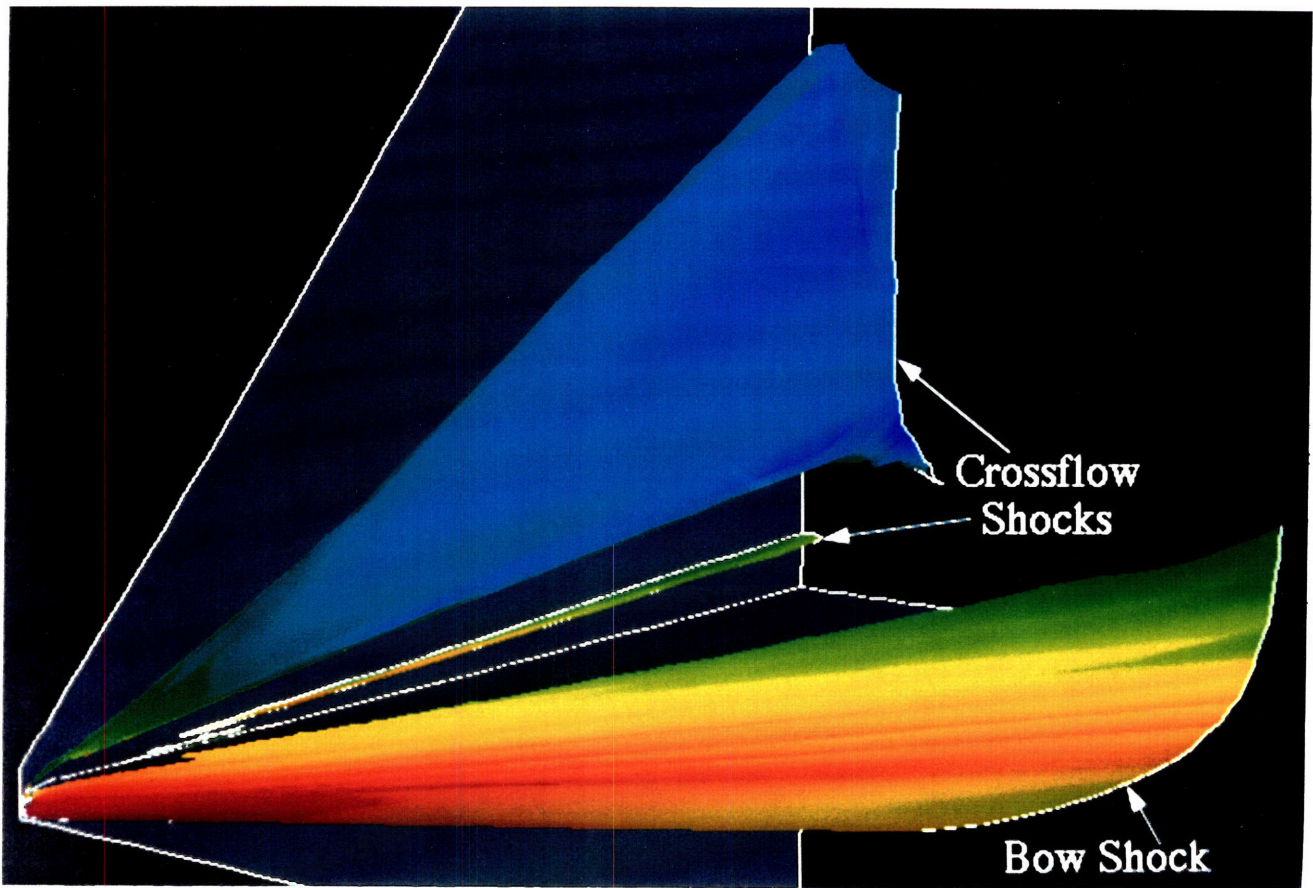
Figure 3.9: Thresholded shock surfaces
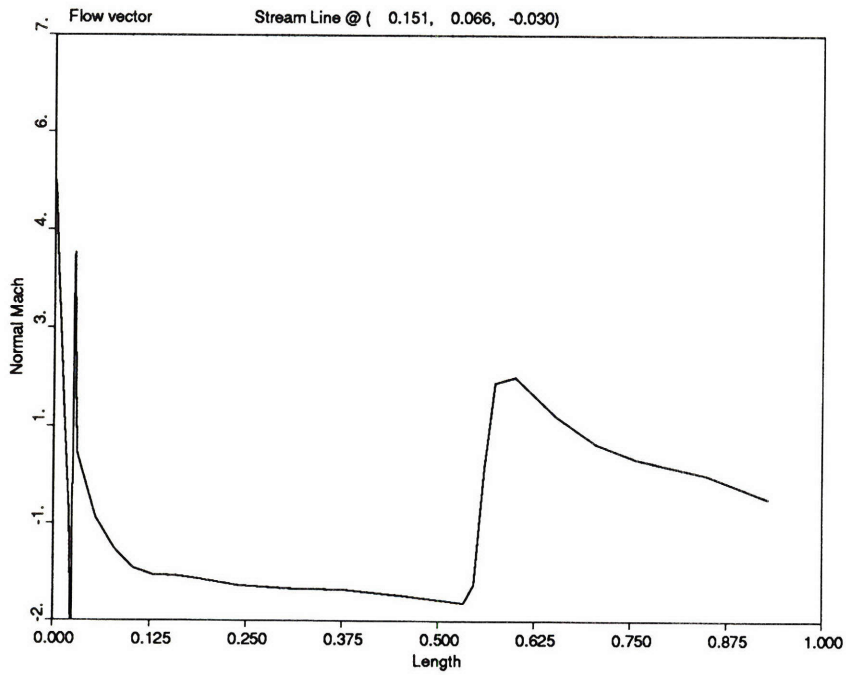
Figure 3.10: Normal Mach number along streamline through first crossflow shock
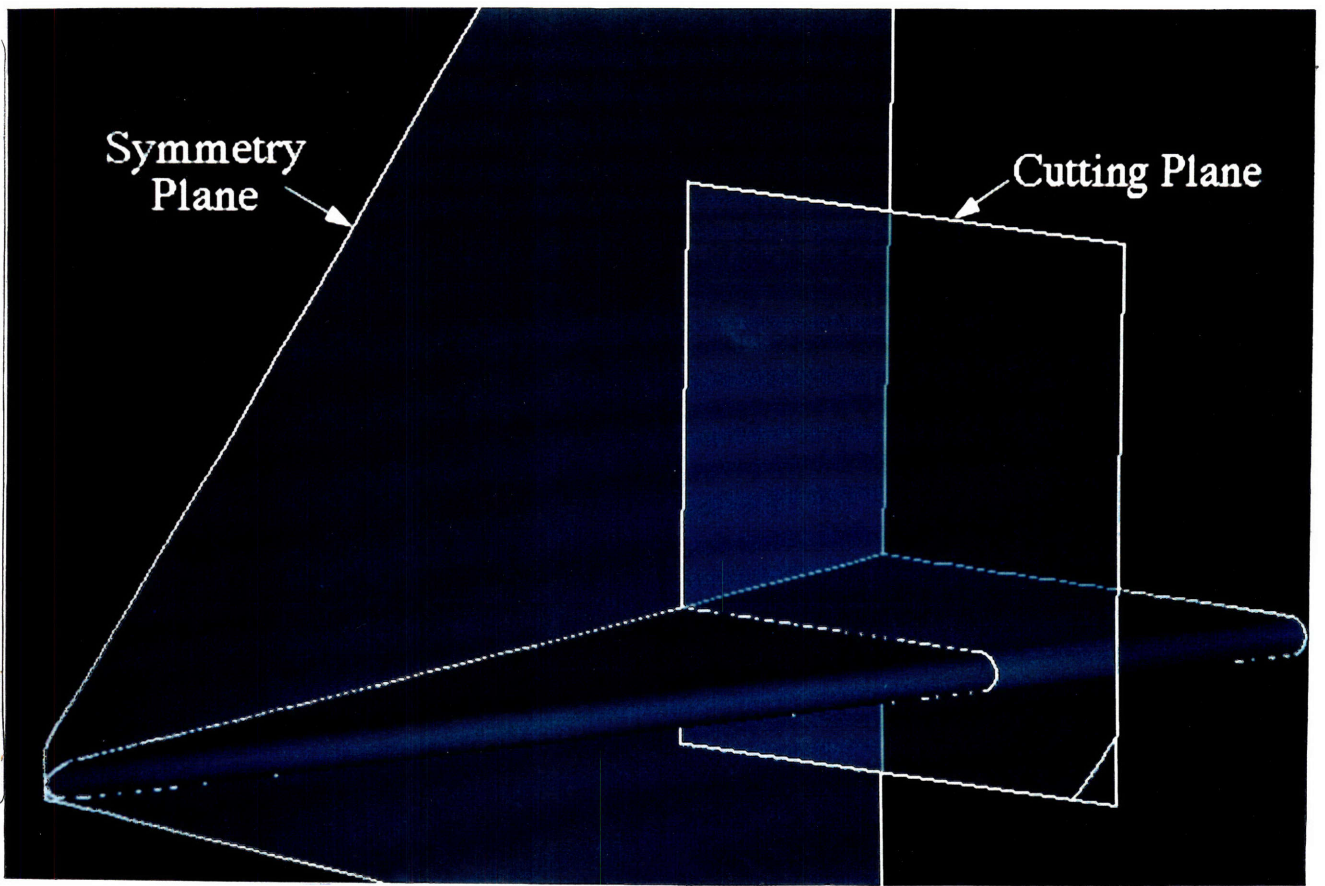
Figure 3.11: 3-D position of cutting plane
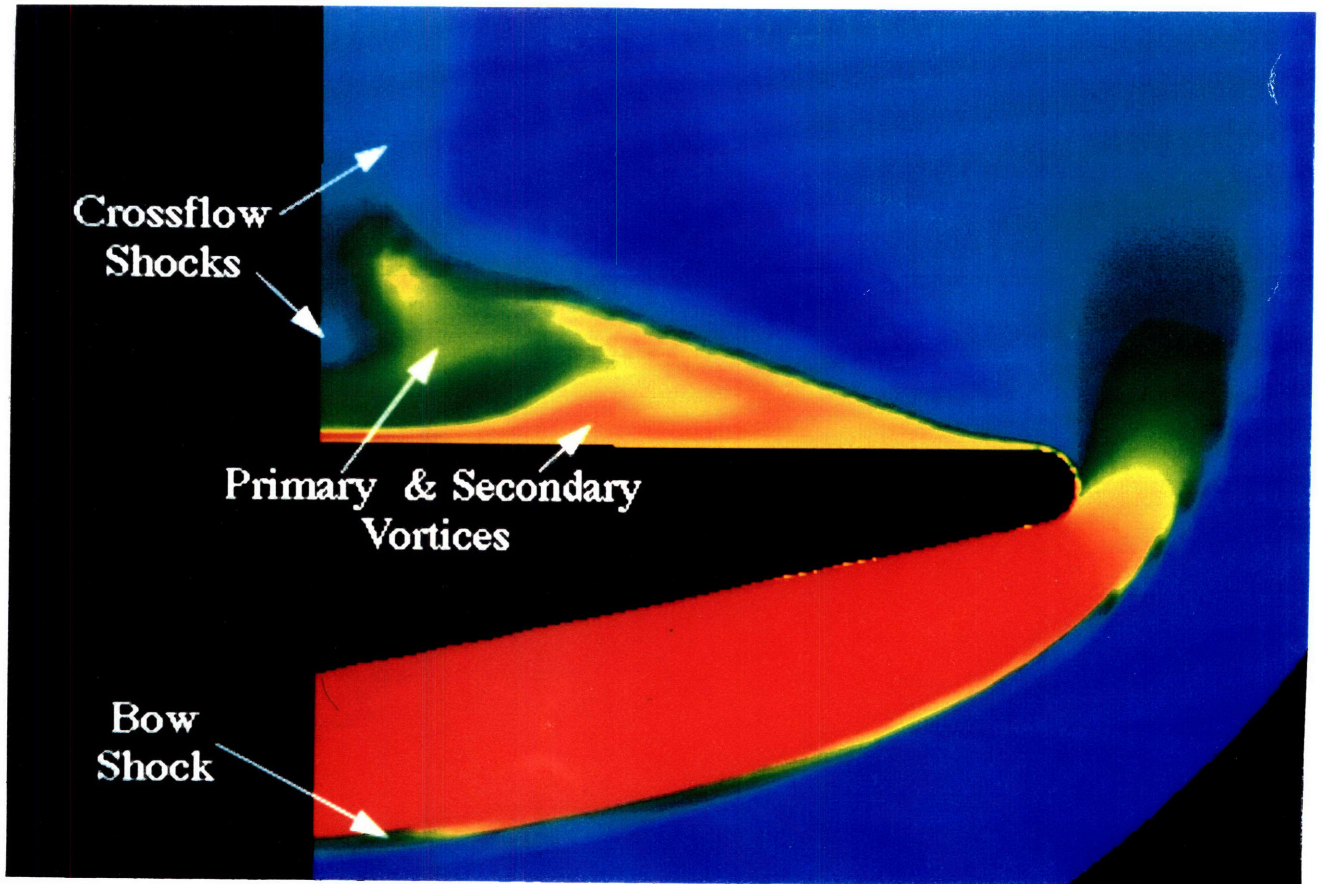
Figure 3.12: Temperature distribution on cutting plane - Goraud shading

65
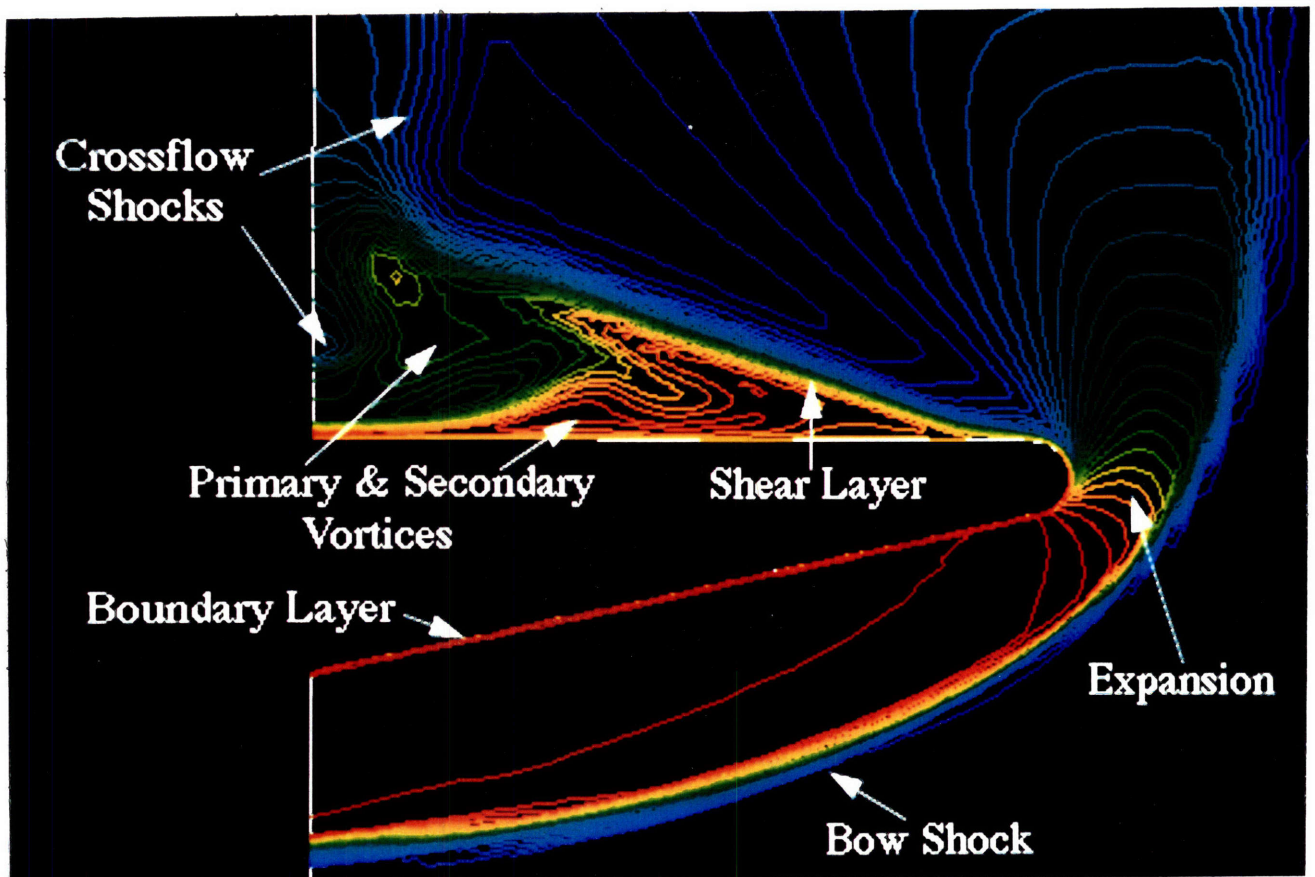
Figure 3.13: Temperature distribution on cutting plane - Contours
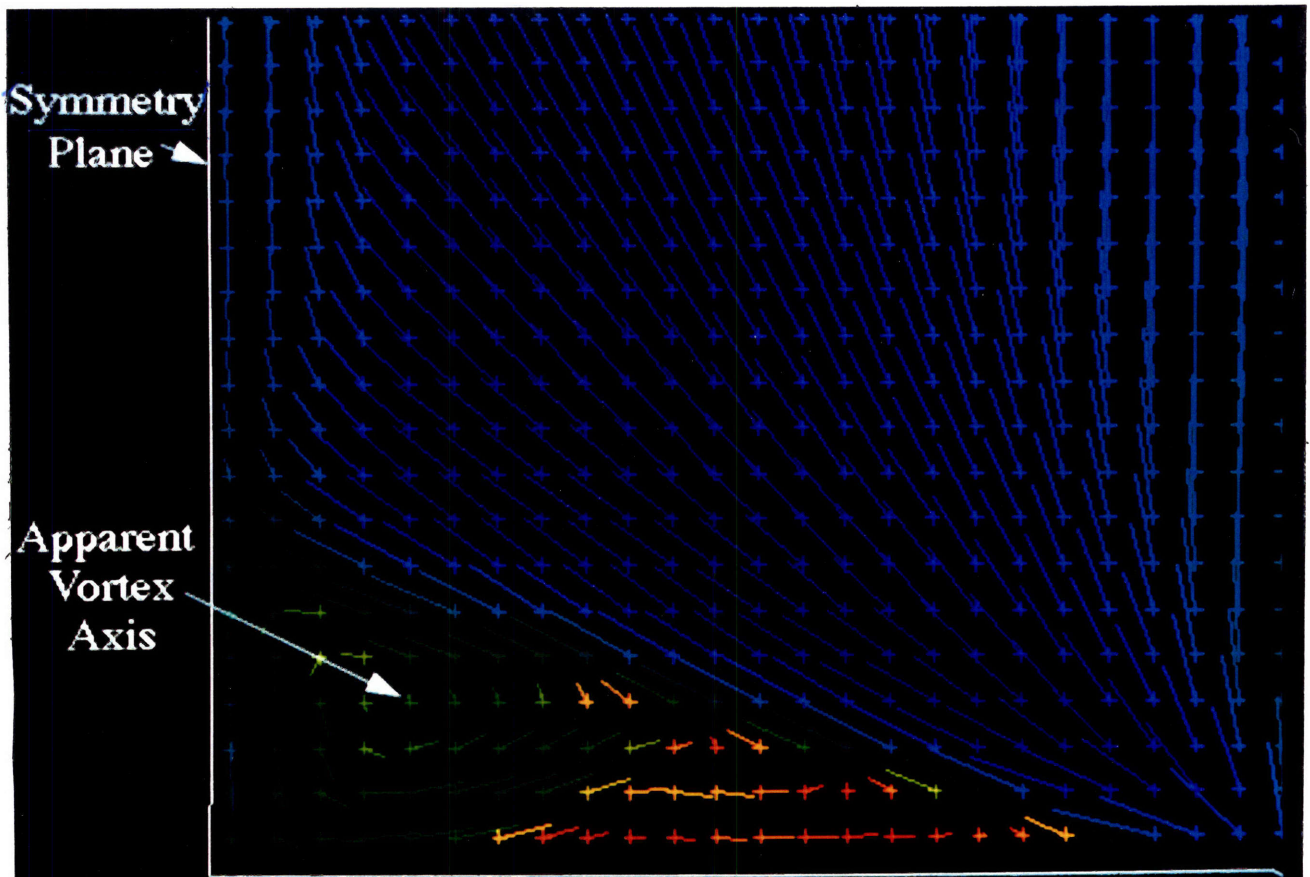
Figure 3.14: Tuft projection on cutting plane perdendicular to symmetry plane
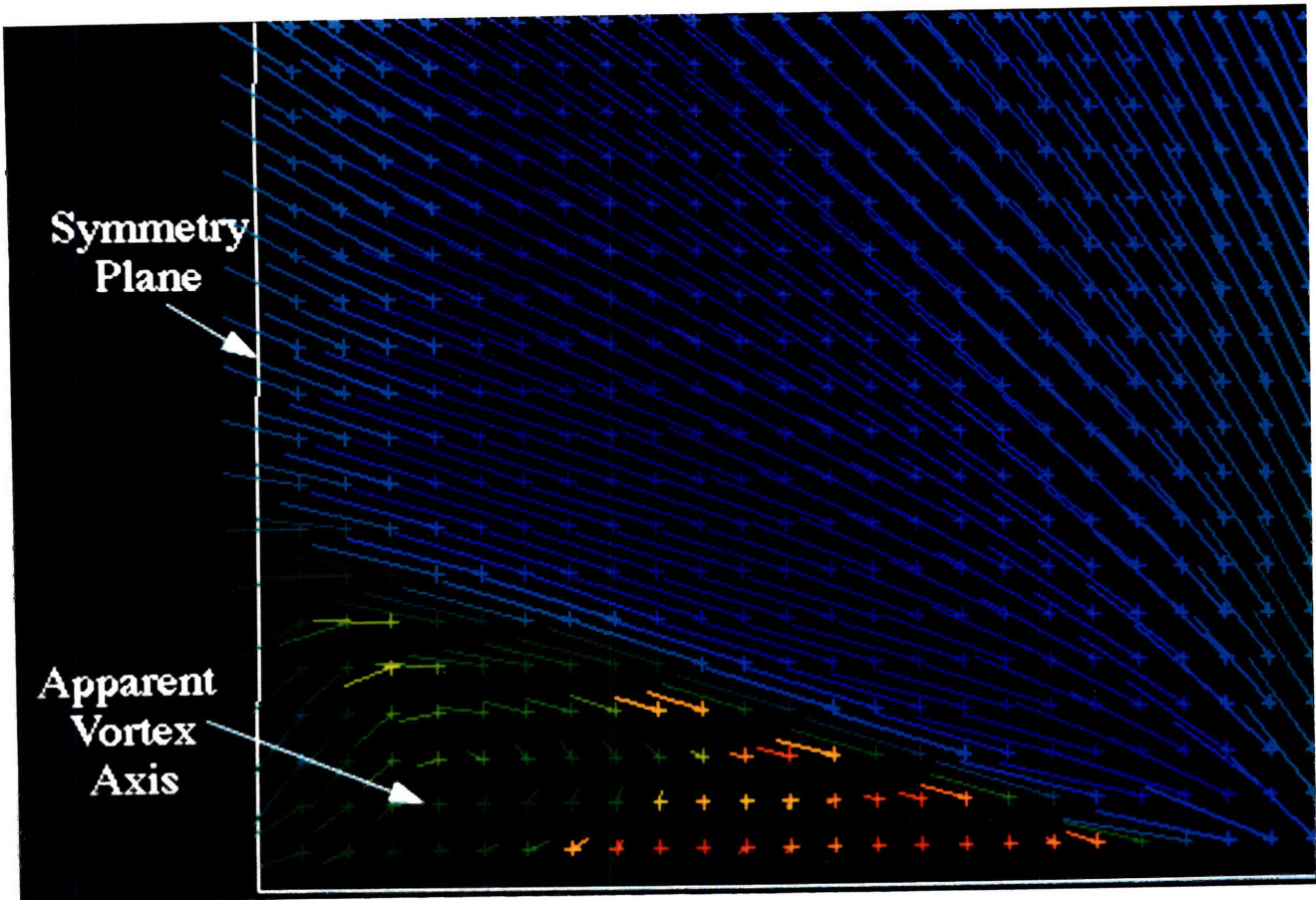
Figure 3.15: Tuft projection on cutting plane perdendicular to leading edge
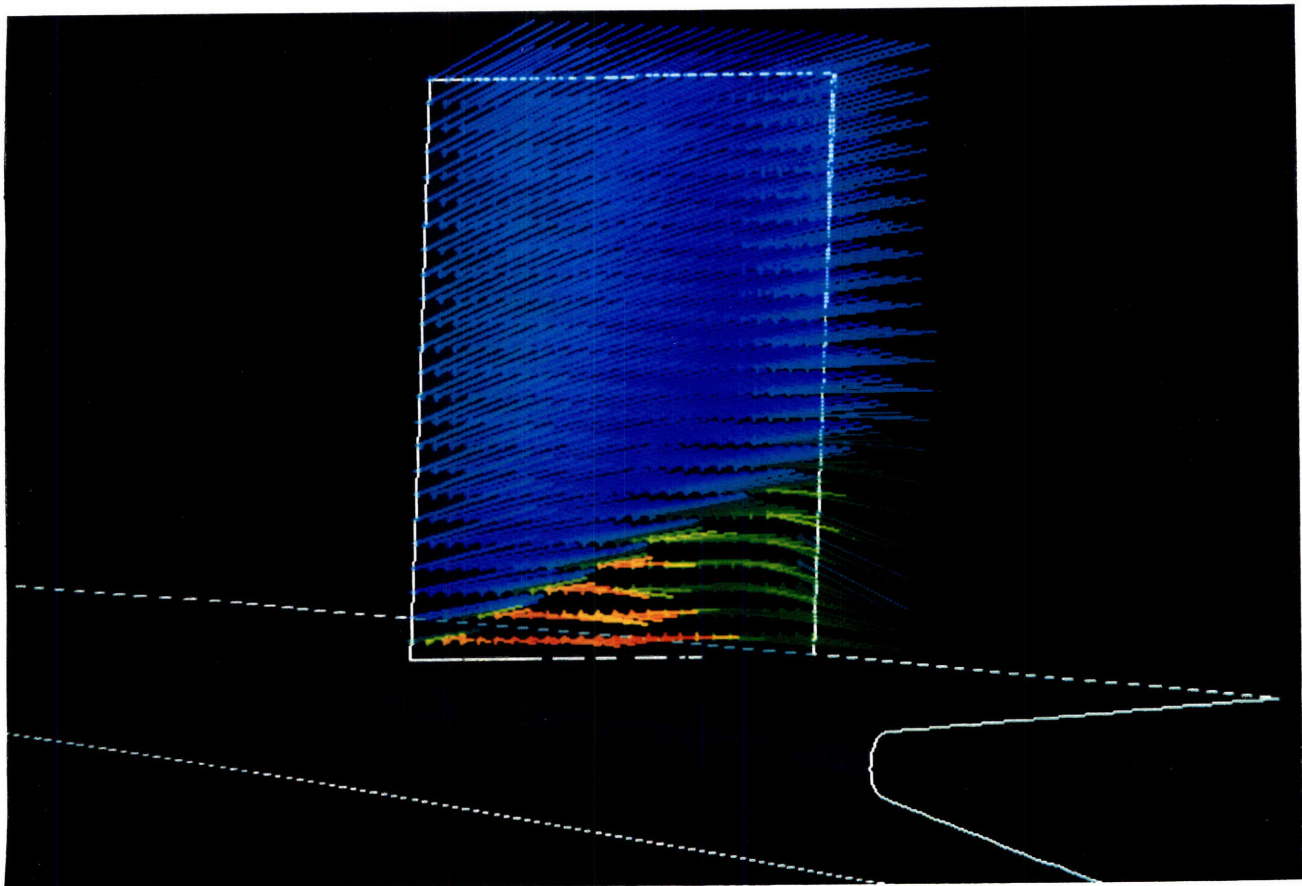
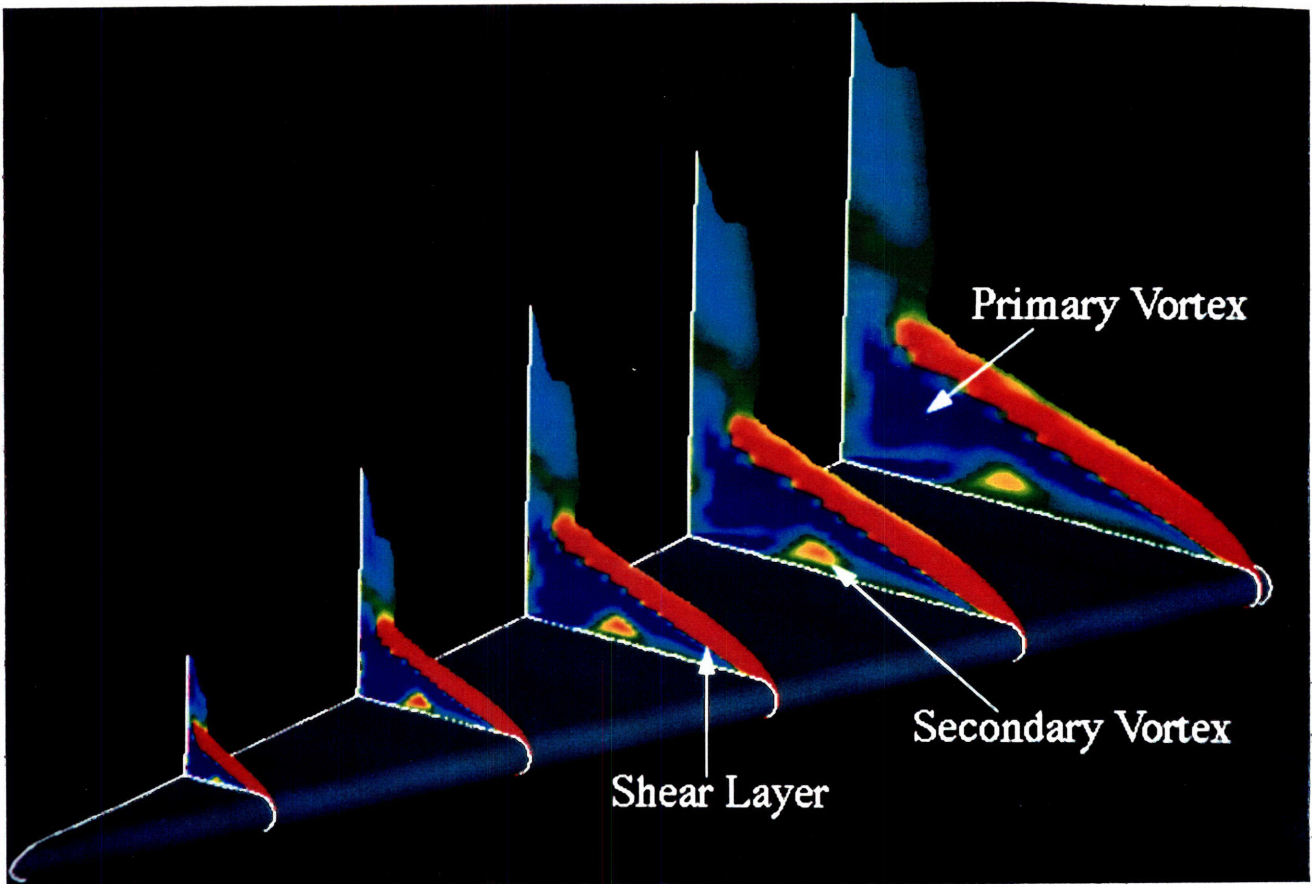
Figure 3.16: 3-D view of tufts

69

Figure 3.17: Several cutting planes thresholded by total pressure rendered by helicity
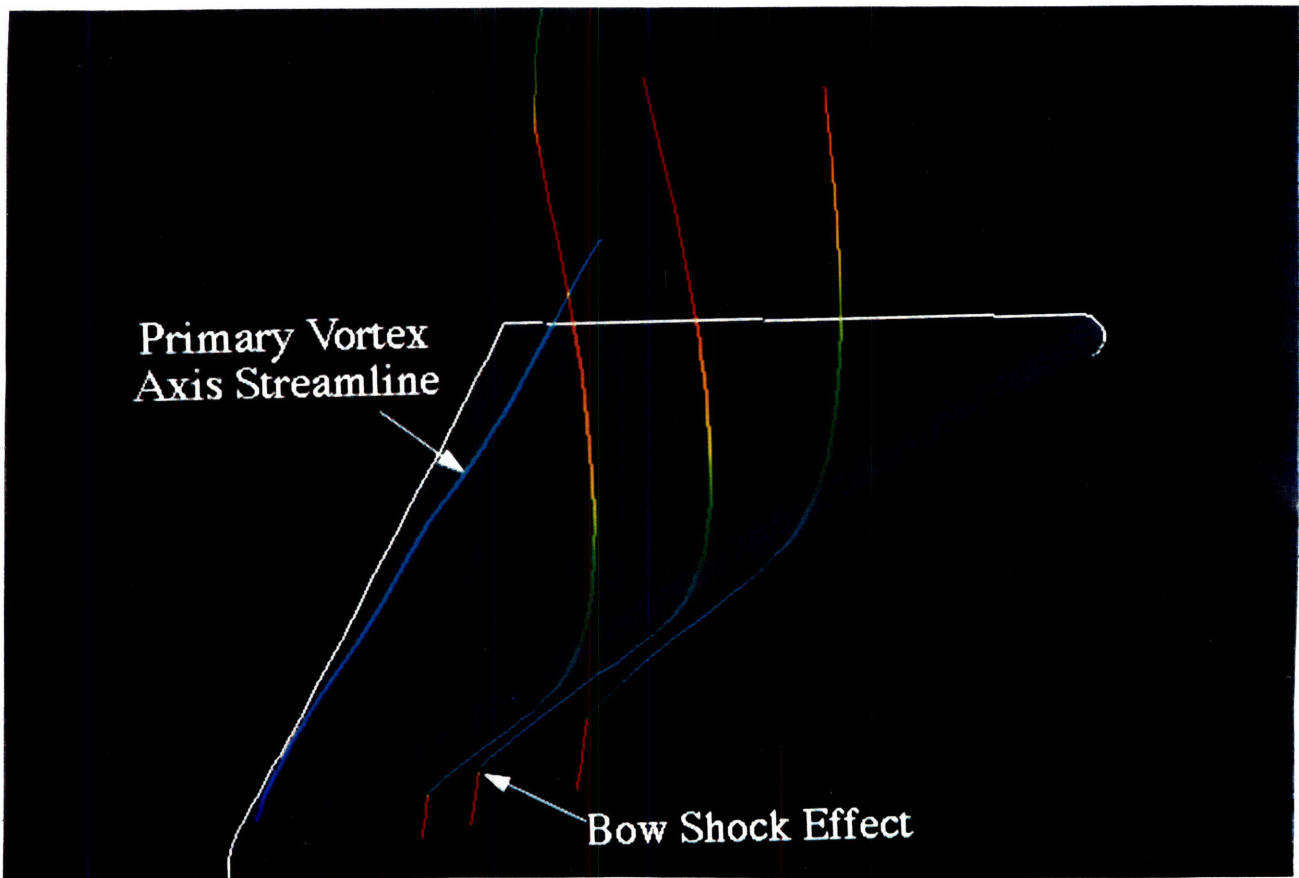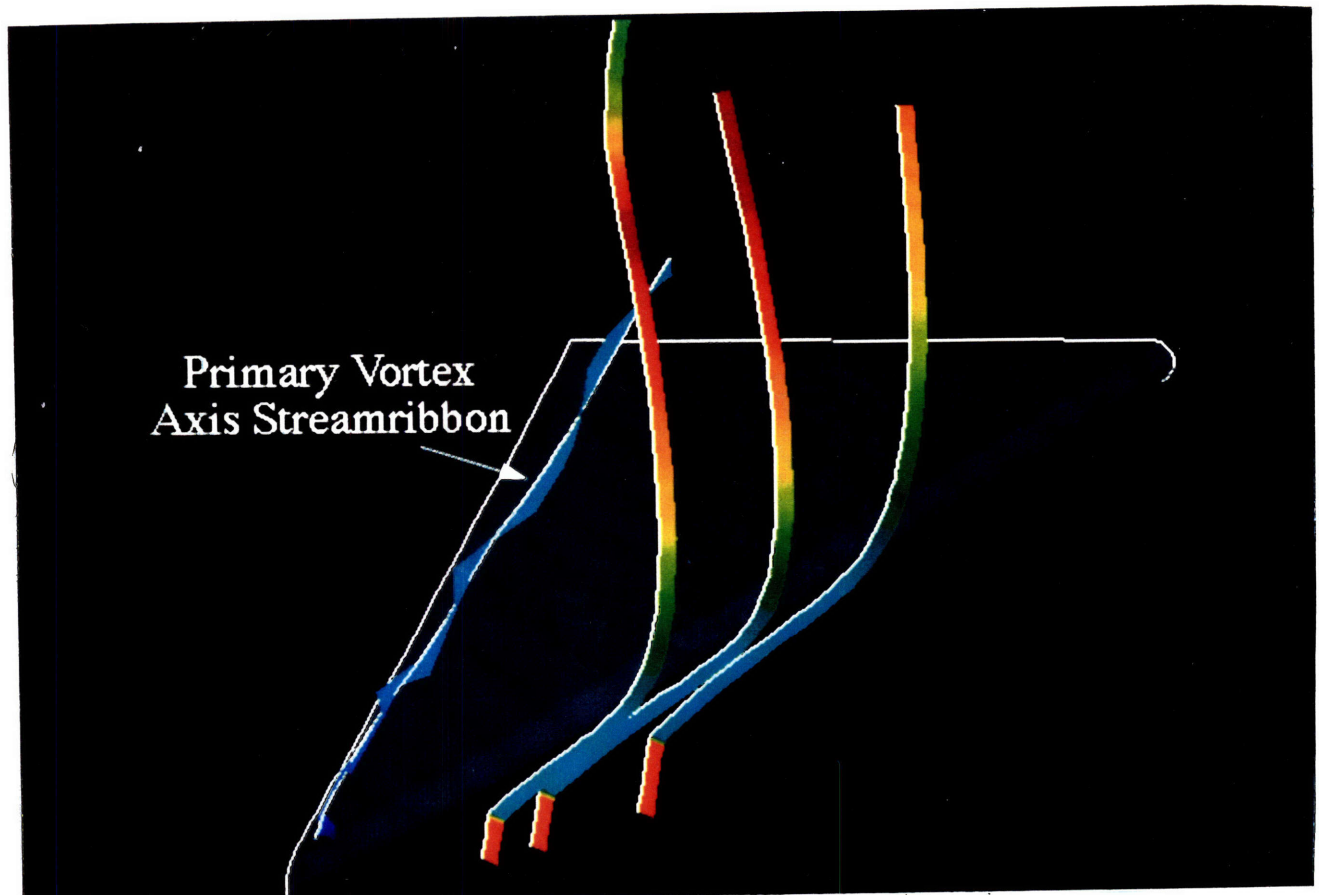

Figure 3.18: Streamlines rendered by Mach number
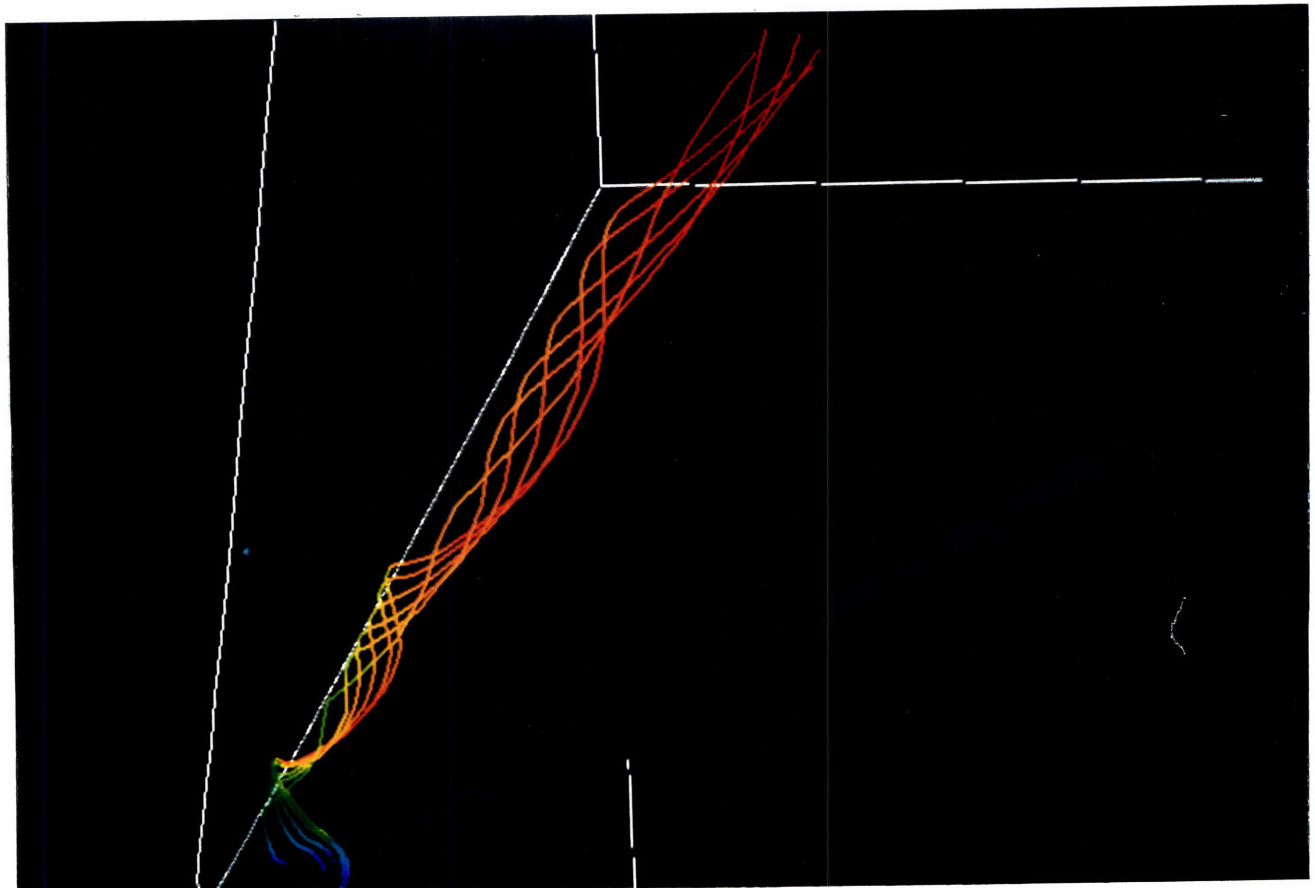
Figure 3.19: Streamribbons rendered by Mach number

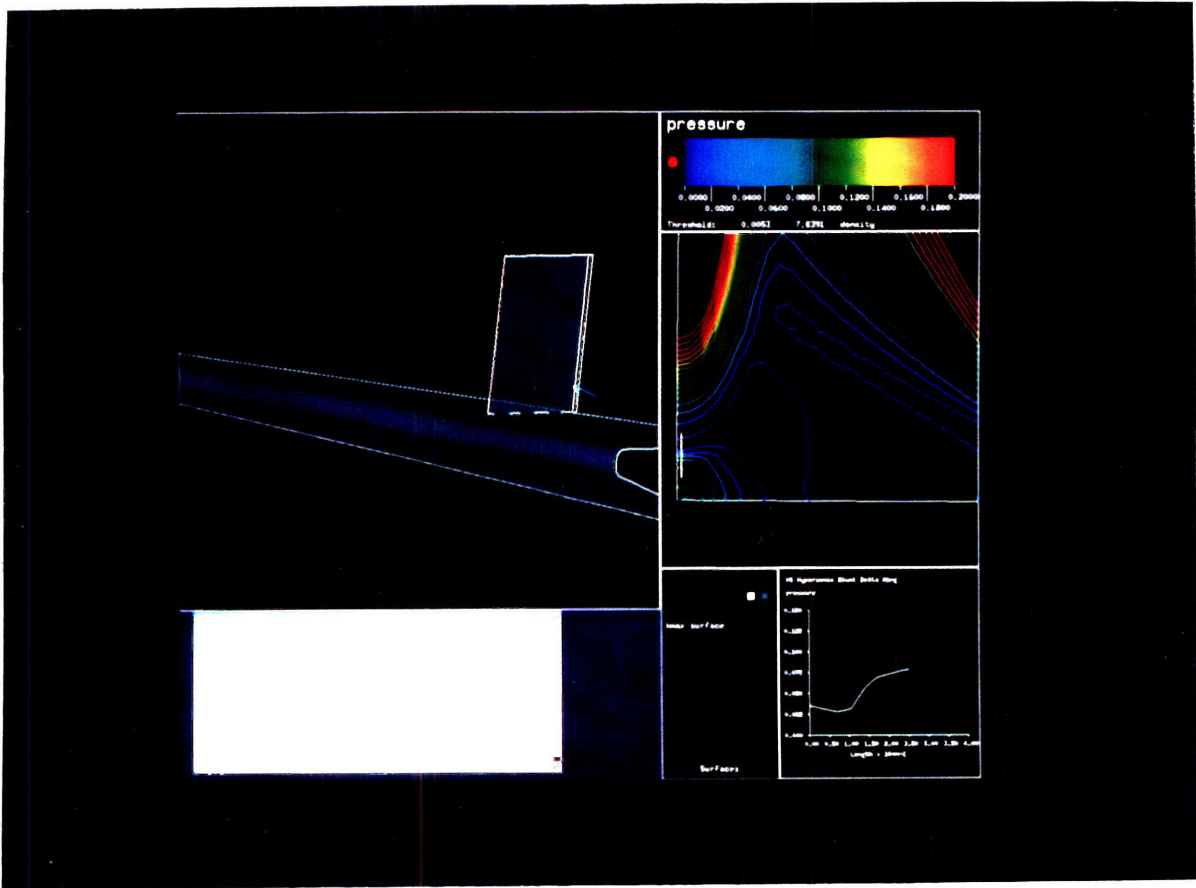Figure 3.20: Streamtube in primary vortex rendered by Mach number

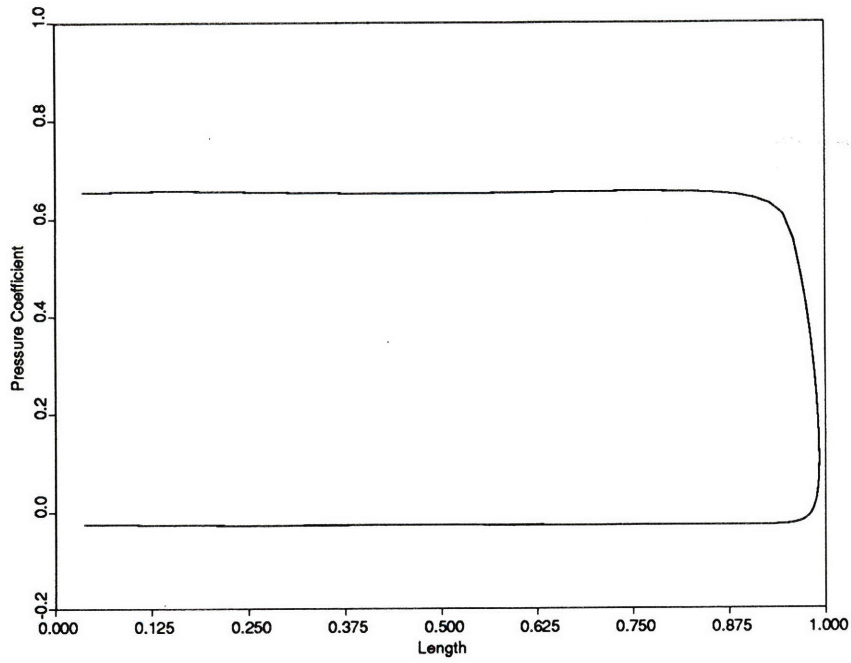Figure 3.21: View of screen with line probe in use

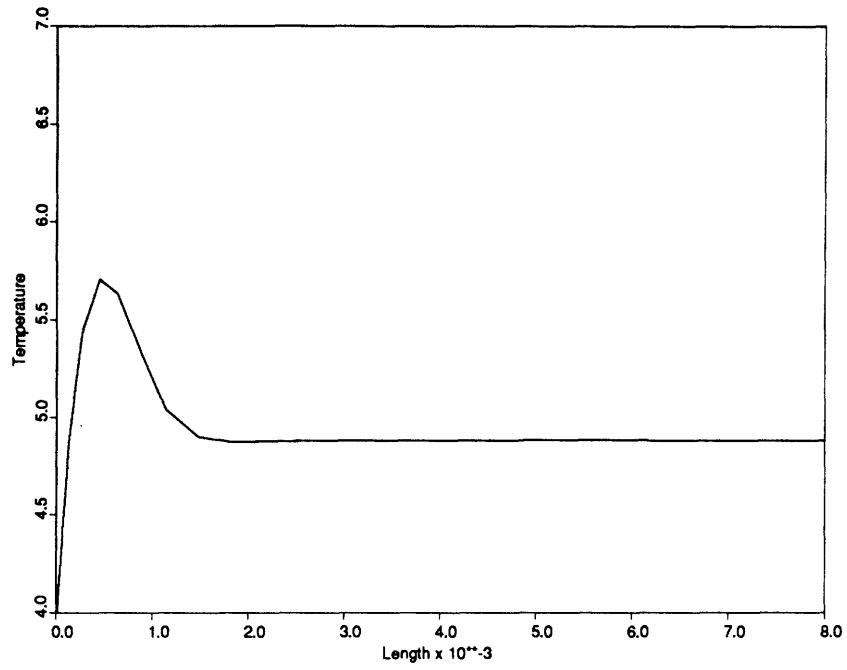Figure 3.22: Surface C_p distribution at 75% chord

75

Figure 3.23: Density distribution in boundary layer
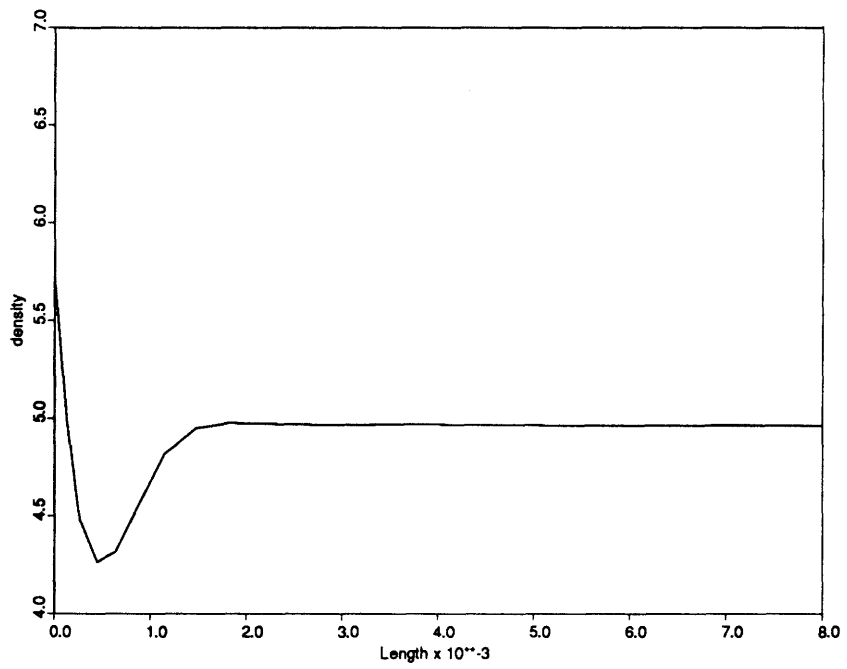

Figure 3.24: Temperature distribution in boundary layer
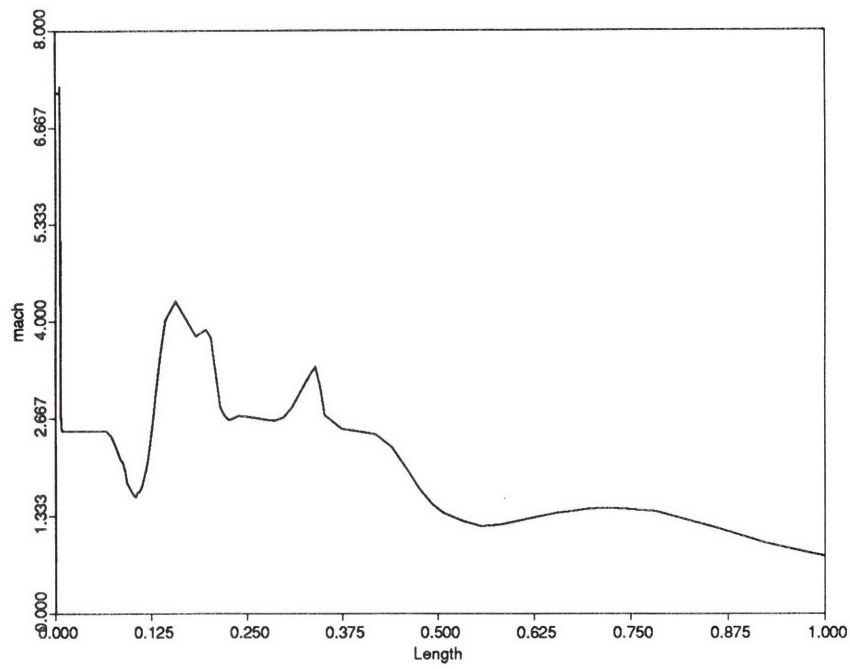
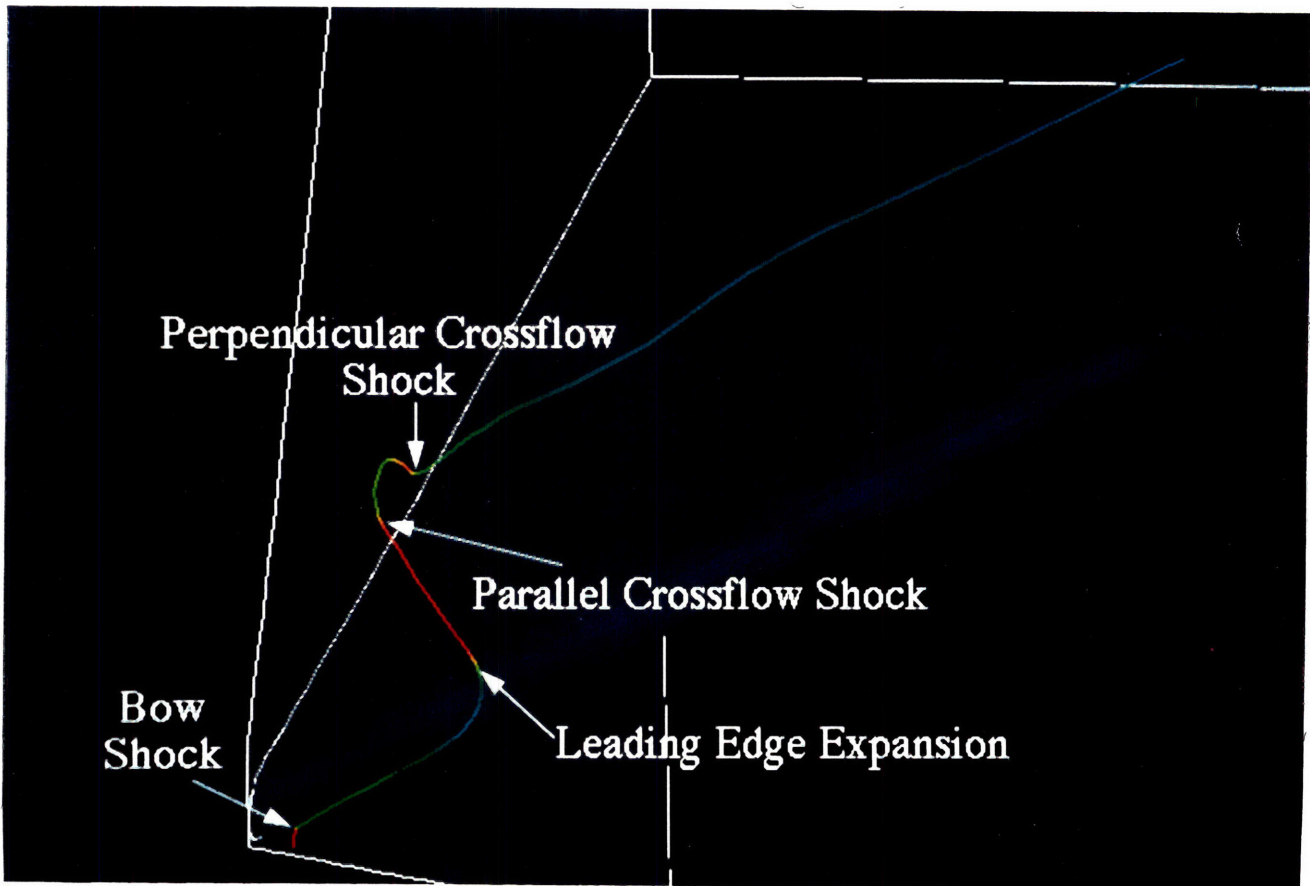Figure 3.25: Mach number along a streamline

Figure 3.26: 3-D view of streamline in secondary vortex

Chapter 4

Vortical Flow Visualization : An Example

The best way to illustrate the effectiveness of the visualization techniques described
previously is by example and that is the emphasis of this chapter. We will employ the
hierarchal visualization strategy discussed in Chapter 3. The 3-D data set used for
this purpose was calculated with a hybrid Euler/Navier-Stokes algorithm by Becker [2].
Preliminary visualization results were presented by Murman $et\ al$[22]. The geometry is
that of the NASA National Transonic Facility (NTF) wing which has a blunt leading
edge with a 65 degree sweep angle. The solution near the wing surface is a thin-layer
Navier-Stokes calculation; the outer solution is an Euler solution. The combined grid
contains 276,000 cells. The alignment of the wing with the coordinate system is the
same as the Lee hypersonic calculation in Figure 3.3. The freestream conditions are:
$M_\infty = 0.85$, $\alpha_\infty = 15°$, and $Re_\infty = 7.5 \times 10^6$.

The freestream conditions of the computation are equivalent to $M_n = 0.41$ and
$\alpha_n = 32.3°$ which from Figure 2.1 is flow Type 2, or the classical vortex flow. Thus, we
expect the solution to contain primary and secondary separation and possibly tertiary
effects. No crossflow shocks should appear. Since the leading edge is rounded, the flow
is not forced to separate there and thus we will need to locate the primary separation
point. Furthermore, because of the blunt leading edge, the flow type near the wing will
vary with secondary separation occurring somewhere along the wing surface. Also, with
the flow being transonic, pressure waves from the trailing edge will travel upstream and
this effect will be felt at the rear of the wing.

4.1   Feature Identification

The first step in the hierarchal visualization strategy is the use of the feature identifi-
cation techniques of Section 3.2 to locate areas of interest in the computation. After

this step, each of the features will then be examined using the scanning and probing techniques.

4.1.1 Flow Topology

One of the best starting points when visualizing a vortical flow is the topology or surface flow. As evidenced by the oil flow descriptions of Chapter 2, topology can provide a great deal of information about the entire flow field. Figure 4.1 shows the surface oil flow pattern. Starting from the symmetry plane, the flow is primarily in the freestream direction. Next, the accumulation at about 40% span is the primary attachment. Further outboard, at 72% span is the secondary separation line. The presence of tertiary separation can also be seen from the oil flow; the separation line is at 79% and the reattachment at 86% span. Although it does not form an obvious line, the secondary reattachment is the final feature and is at 95% span. The primary separation, lacking from the oil flows, must occur at or at least very near the wing's leading edge. The surface flow also shows the change of the flow progressing from the apex to the trailing edge. For example, tertiary separation first appears at about 50% root chord. Another feature which should be highlighted is the presence of an accumulation at the trailing edge. This line probably indicates that the boundary layer separates before the trailing edge due to the adverse pressure gradient. Thus, a region of reversed flow exists between the trailing edge and the accumulation line. Finally, the oil flow patterns also indicate a change in the tertiary vortex at about 85% chord. At this point, the oil flow lines appear to have a reversal in direction. Again, we are probably seeing a trailing edge effect on the tertiary vortex but a further, more detailed, examination will be required.

4.1.2 X-rays

The first step when using X-rays is to choose the scalar field. In a vortex, the total pressure loss is generally high; thus, if an X-ray of total pressure loss is performed, it should detect the vortices. The linear mapping function will be used to preferentially highlight the greater regions of total pressure loss. Next, a decision must be made

concerning the position of the first X-ray picture. The flow will be vortical on the leeside; thus, an image looking in the flow direction, i.e., along the x-axis, could prove useful. Figure 4.2 is an X-ray image in that position. The primary vortex can be clearly seen emanating from the symmetry plane and eventually turning into the freestream direction. At the turning of the primary vortex, the shading increases; this effect is because the vortex is now more nearly aligned with the X-ray direction. Consequently, an individual X-ray will travel through more of the vortical region and a greater loss will occur. Still concentrating on the primary vortex, notice that after it turns into the freestream, the vortical region expands. This expansion is expected and is simply the vortex diffusing due to both physical and numerical dissipation of the vortex as it travels downstream. Just outboard of the primary vortex is what appears to be the secondary vortex. At the end of the secondary vortex, probably in the vicinity of the trailing edge, a drastic change of shape occurs. The exact cause of this change cannot be determined from this image and further investigation is needed. Finally, near the symmetry plane, just above the wing, a small area of loss also appears. This feature could be the wake or possibly the boundary layer at the trailing edge if it separates as indicated from the surface flow visualization. Before continuing with the next image, note the effectiveness of this one X-ray; with only a single image, we found the primary and secondary vortex, noted the expansion of the primary vortex after turning into the freestream, and detected interesting flow features near the end of the secondary vortex and near the symmetry plane.

Next, we will attempt to reach a better understanding of the two unknown features which are believed to be near the trailing edge. To further probe this area, we will take an X-ray looking down on the wing's leeside near the trailing edge (Figure 4.3). This image clearly shows both vortices. The secondary vortex is extremely large as it turns downstream which is probably the feature noticed in the first X-ray. From this image, the secondary vortex would appear to have a higher total pressure loss than the primary. However, the truth is that the secondary vortex is much larger than the primary and thus an X-ray must travel through a longer distance of loss. To bring this point out further, take the same X-ray but this time use the midpoint mapping function to highlight moderate loss levels (Figure 4.4). The secondary vortex clearly suffers a higher X-ray loss level; thus, the secondary vortex has a larger area of mid-range total

pressure loss. Besides the two vortices, this midpoint X-ray also reveals a region of moderate loss on the symmetry plane at the trailing edge (the light green-blue area). This feature probably corresponds to the symmetry plane feature from Figure 4.2 which was postulated to be a trailing edge effect and may indicate separation.

4.1.3 Clouds

The next step is to use clouds for feature identification. As with X-rays, total pressure is chosen as the threshold variable. Figure 4.5 is the result of clouds with a total pressure loss range of (0.2,0.8). This image is also rendered by total pressure loss and shows the highest losses occuring in the core of the primary vortices (the yellow region). All the features detected from the X-rays are present. The primary and secondary vortices can be clearly seen. At the trailing edge, the rapid expansion of the secondary vortex is now unmistakable. Also, the wake at the symmetry plane is visible and the shape is similar to that displayed by the X-ray of Figure 4.2. To get a handle on the trailing edge effect, the same clouds are rendered by Mach number in Figure 4.6 with blue (red) being low (high)Mach number. The flow in the secondary vortex is very slow and near stagnation at the trailing edge. The rapid deceleration and subsequent breakdown of the secondary vortex is easily recognizable. The primary vortex also undergoes a sudden deceleration at the trailing edge; however, being much stronger than the secondary vortex, the primary still persists downstream of the wing.

Finally, the total pressure loss clouds are rendered by helicity in Figure 4.7. The negative helicity (blue) primary vortex and positive helicity (red) secondary vortex can be seen. The rolling of the leading edge vortex sheet into the primary vortex is also apparent and confirms the suspicion that primary separation occurs on the leading edge. Note that the breakdown region of the secondary vortex indicates very little helical motion exists (green is zero helicity). Therefore, all vortical motion from the secondary vortex has probably been diffused as a result of the trailing edge adverse pressure gradient. One last feature detected with clouds is an enlargement in the leading edge vortex sheet just before the primary vortex. The feature is particularly evident at about 50% chord just above the secondary vortex. At this stage in the visualization, the exact cause of the anomaly is unknown and a more intensive examination will be

4.1.4 Shock Finding

The shock finder only detects a small possible shock in the primary vortex near the trailing edge. The speed gradient is extremely small, however, and this region is probably a rapid, but isentropic, deceleration due to the trailing edge.

4.2 Detailed Analysis

After identifying various features in the flow field, the next step is to perform a detailed analysis of each of them. The scanning and probing visualization methods are used for this purpose. This portion of the visualization is organized by the particular feature being investigated; this organization better highlights the truly systematic approach used when visualizing a flow field.

4.2.1 Location of Primary Separation

From the surface flow visualization, the exact location of the primary separation could not be determined; these results indicated that primary separation occurred very near the leading edge. The helicity clouds of Figure 4.7 also indicated the same separation location. However, a detailed look at the leading edge will quickly show the exact position of primary separation. First, a cutting plane is placed normal to the leading edge at approximately 50% chord with shading by helicity (Figure 4.8). At primary separations, helicity switches sign[16]. The location of primary separation can now clearly be seen just above the leading edge where the helicity shading switches from red (positive) to blue (negative). To probe just slightly further, tufts of the velocity field are displayed on a blow-up of the cutting plane at the leading edge (Figure 4.9). The vectors confirm the primary separation as occurring just slightly above the leading edge.

4.2.2 Leading Edge Vortex Sheet Anomaly

An unexpected enlargement in the leading edge vortex sheet was first noticed using clouds (Figure 4.5). To further investigate, the same cutting plane normal to the leading edge at approximately 50% chord is used. Tufts of the velocity vectors rendered by helicity are displayed in Figure 4.10. The vortical flow in the region of interest can be clearly seen. The presence of this small sub-vortex has been seen in the experimental results of Payne[25] albeit at much lower Mach number and Reynolds number. Their existence is thought to be related to the Kelvin-Helmholtz instability of free shear layers. Payne's flow visualization shows the presence of many sub-vortices in the leading edge vortex sheet. With this in mind, we scan the cutting plane to attempt to locate additional sub-vortex structures. At about 30% chord, another sub-vortex can clearly be seen (Figure 4.11). Streamlines are now spawned from this cutting plane in the sub-vortices and the primary vortex; they are rendered by total pressure loss (Figure 4.12). The three vortices can now be seen clearly. The first sub-vortex and the primary vortex begin at the nose of the wing while the second sub-vortex begins around 30% chord. Both sub-vortices appear to breakdown as a result of the trailing edge pressure gradient. The primary vortex, being significantly stronger, persists beyond the trailing edge. After the streamlines leave either sub-vortex, they become entrained in the primary vortex. Thus, the primary shear layer appears to be composed of several smaller sub-vortices that are very similar in nature to the Kelvin-Helmholtz instability of a free shear layer.

4.2.3 Secondary Vortex Breakdown

The next feature we wish to investigate is the large total pressure loss region at the trailing edge associated with the secondary vortex. This feature, first noticed with X-rays, is believed to be the result of the secondary vortex breaking down as it nears the trailing edge. Once again, we use a cutting plane, this time normal to the symmetry plane, to begin scanning the data. In this instance, the cutting plane is particularly useful because the feature of interest has been clearly located by the various X-rays and, therefore, we know exactly where and how to scan the flow field. Thresholding will also be used with the cutting plane to allow several planes to be viewed simultaneously.

86

First, cutting planes are positioned at $x = 0.8, 0.9, 1.0, 1.1, 1.2$ in chord units. Then, a total pressure loss threshold of (0.2,0.8) is applied. Figure 4.13 and 4.14 are these thresholded cutting planes rendered by total pressure and helicity, respectively. The large total pressure loss region associated with the secondary vortex is clearly seen; at the trailing edge, the secondary vortex has greatly expanded which is the first hint of breakdown occurring. The helicity-rendering shows that in the rapid expansion region of the secondary vortex, the helical motion disappears. Thus, the secondary vortex has indeed gone through a breakdown process. Also, recall that the clouds had previously revealed the secondary vortex to essentially stagnate at the trailing edge.

One final check on the secondary vortex breakdown hypothesis is done using streamlines. In Figure 4.15, several streamlines in the primary and secondary vortex are displayed looking at the wing leeside from along the z-axis. The streamlines are colored by Mach number. The vortical nature of the secondary vortex clearly stops just before the trailing edge is reached. Also, the secondary vortex streamlines nearly stagnate (note the blue, i.e. low, Mach number color) and significantly change directions to the outboard. Since the flow beyond the bursting region would be turbulent, the laminar calculation cannot adequately determine the type of burst that occurs. The primary vortex, being much stronger, manages to overcome the adverse pressure gradient without suffering breakdown. Finally, from the total pressure loss cutting planes, note that the total pressure loss in the secondary vortex is actually less than that in the primary vortex beyond the trailing edge; however, the secondary vortex loss region does cover a larger area. This finding confirms the interpretation of the X-ray images using the linear and midpoint mappings (Figure 4.3 and 4.4).

4.2.4 Tertiary Vortex Breakdown

The flow topology indicated a breakdown of the tertiary vortex at about 85% chord. First, we place a cutting plane in the center of the tertiary separation region tangent to the core direction. This particular view is used because the flow is suspected to separated and a quick way to visualize this is using tufts. However, for tufts to be effective in detecting separation, the cutting plane must be aligned in the approximate flow direction; in this alignment, the projection of the velocity vectors on to the cutting

plane will clearly show the reversal in flow direction and thus the separation location. Figure 4.16 shows the velocity vector on this streamwise oriented cutting plane rendered by pressure (red is high pressure). The tufts have been displayed at the intersections of the cutting plane and the computational grid. The stray vectors are a result of the computational grid and the cutting planed not being perfectly aligned. The white line is the wing surface and the slope change on the left hand side is the beginning of the trailing edge. The separated flow is now obvious from the velocity profiles. Note that the adverse pressure gradient from the trailing edge is visible in the shading of the vectors. To see the effect of the separation, several streamlines are spawned from the cutting plane and rendered by pressure in Figure 4.17. The streamline technique clearly shows the separated flow. The two reversed flow streamlines reveal a rapid rising in what remains of the tertiary vortex as it encounters the trailing edge. The result is an apparent thickening of the trailing edge.

4.2.5   Trailing Edge Separation

The effects of the trailing edge have already been observed on the secondary and tertiary vortices. From this experience, the accumulation line from the surface flow is sure to be a trailing edge separation region. Looking back at Figure 4.13, notice that the boundary layer undergoes a rapid thickening at the trailing edge. This rapid boundary layer growth is indicative of flow separation. Also, recall that this larger region of total pressure loss due to the boundary layer thickening was noticed using X-rays with a midpoint mapping in Figure 4.4. As with the tertiary vortex breakdown, the exact location of separation was determined by aligning a cutting plane in an approximately streamwise direction (normal to the trailing edge in this case) and using tufts to display the velocity vectors. After locating the separation point, streamlines were then spawned in the separated region. Figure 4.18 shows the resulting streamlines which confirm trailing edge separation. The wing surface is rendered with pressure contours or isobars and shows the increasing pressure near the trailing edge in the region of separation.

4.2.6 Wake Position

The final feature of interest is the wake. The wake was noticed in both X-rays (Figure 4.2) and clouds (Figure 4.5). To visualize the wake, thresholded cutting planes rendered by total pressure loss are used again exactly as for Figure 4.13. The only difference is that the threshold is not as severe and more of the lower total pressure loss region is displayed; thus, more of the wake is seen. The shape of the wake in Figure 4.19 is now quite clear and matches what was expected from the feature identification techniques. As it travels downstream, the wake becomes entrained in the primary vortex. Also note that the loss in the wake and the primary vortex diffuses as they travel downstream. This diffusion is a result of numerical and physical diffusion. However, at this high of Reynolds number, the diffusion process should be extremely slow and thus numerical diffusion probably is the dominating factor. A possible solution to this problem is adaption which by placing more cells in regions of interests attempts to decrease numerical errors locally. Landsberg studied this possibility in her work and found numerical diffusion errors can be significantly decreased by using adaption[12].
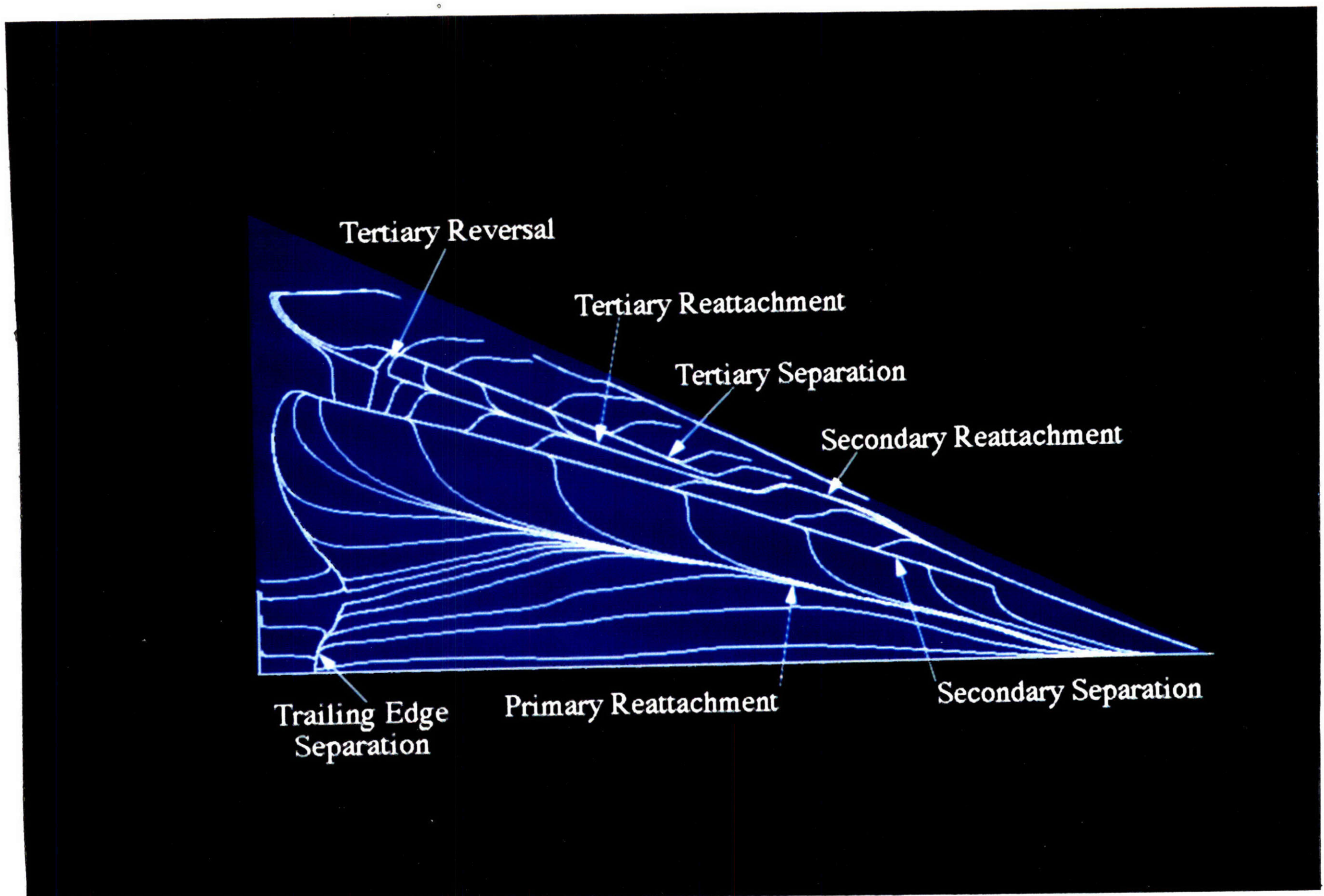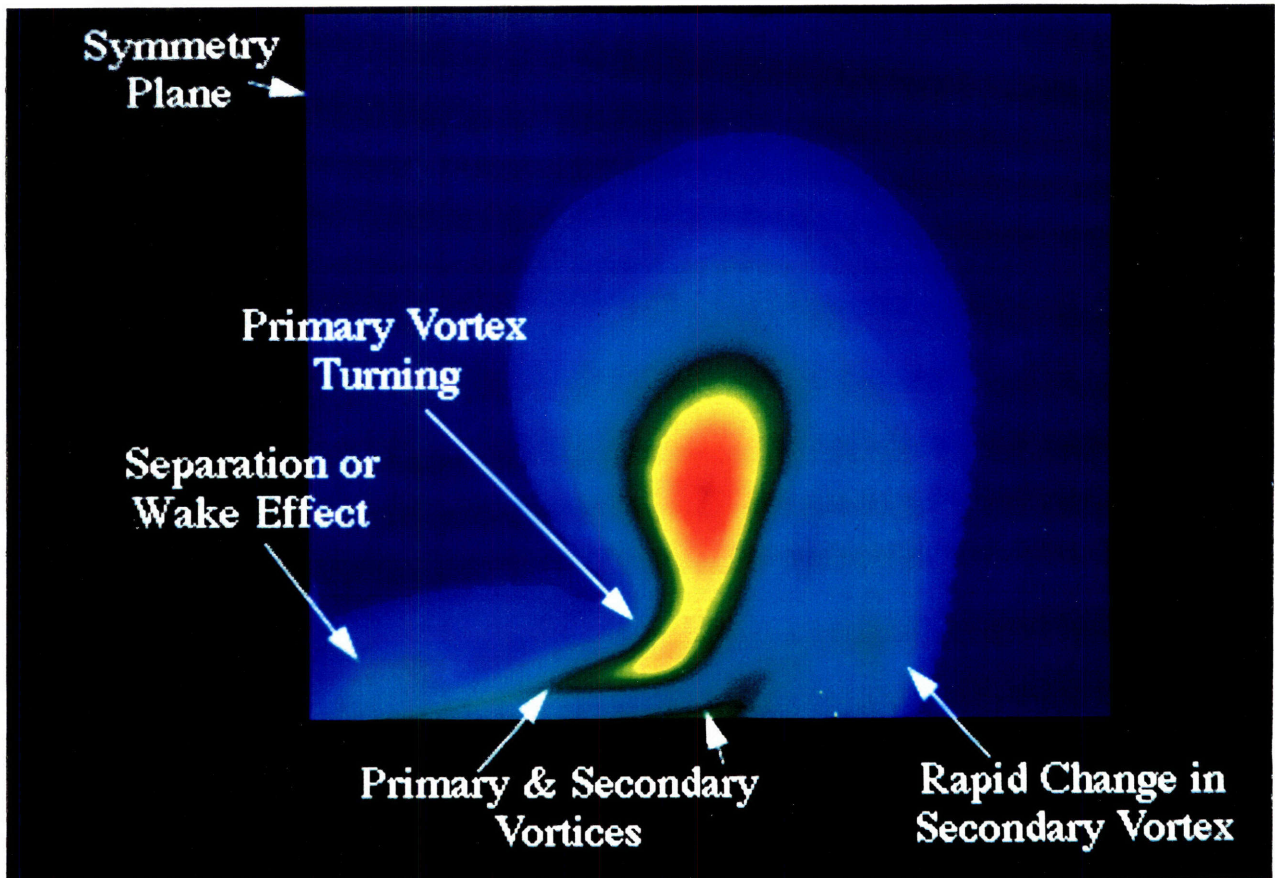
Figure 4.1: Surface flow topology visualization

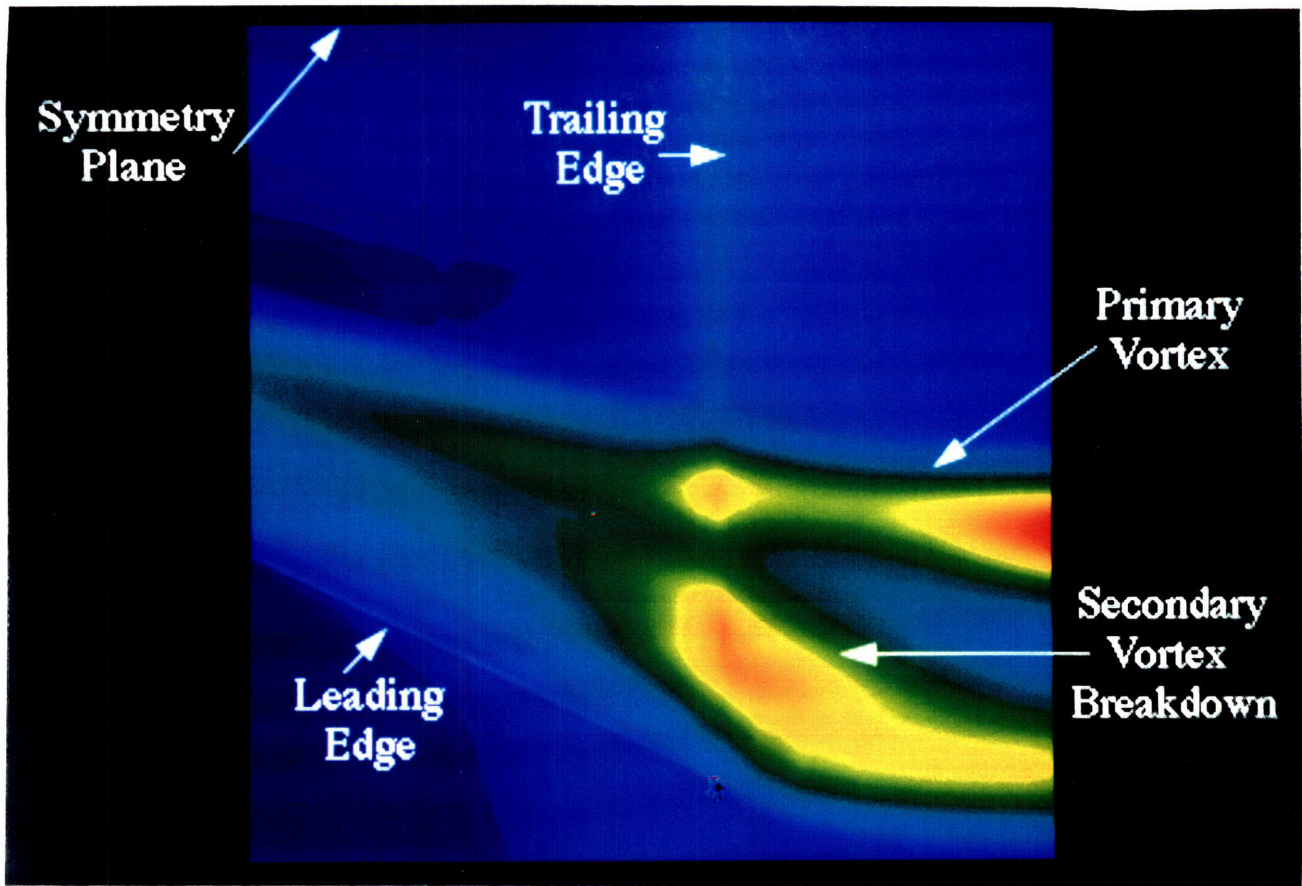Figure 4.2: X-ray of total pressure along x-axis

Figure 4.3: X-ray of total pressure at trailing edge - linear mapping
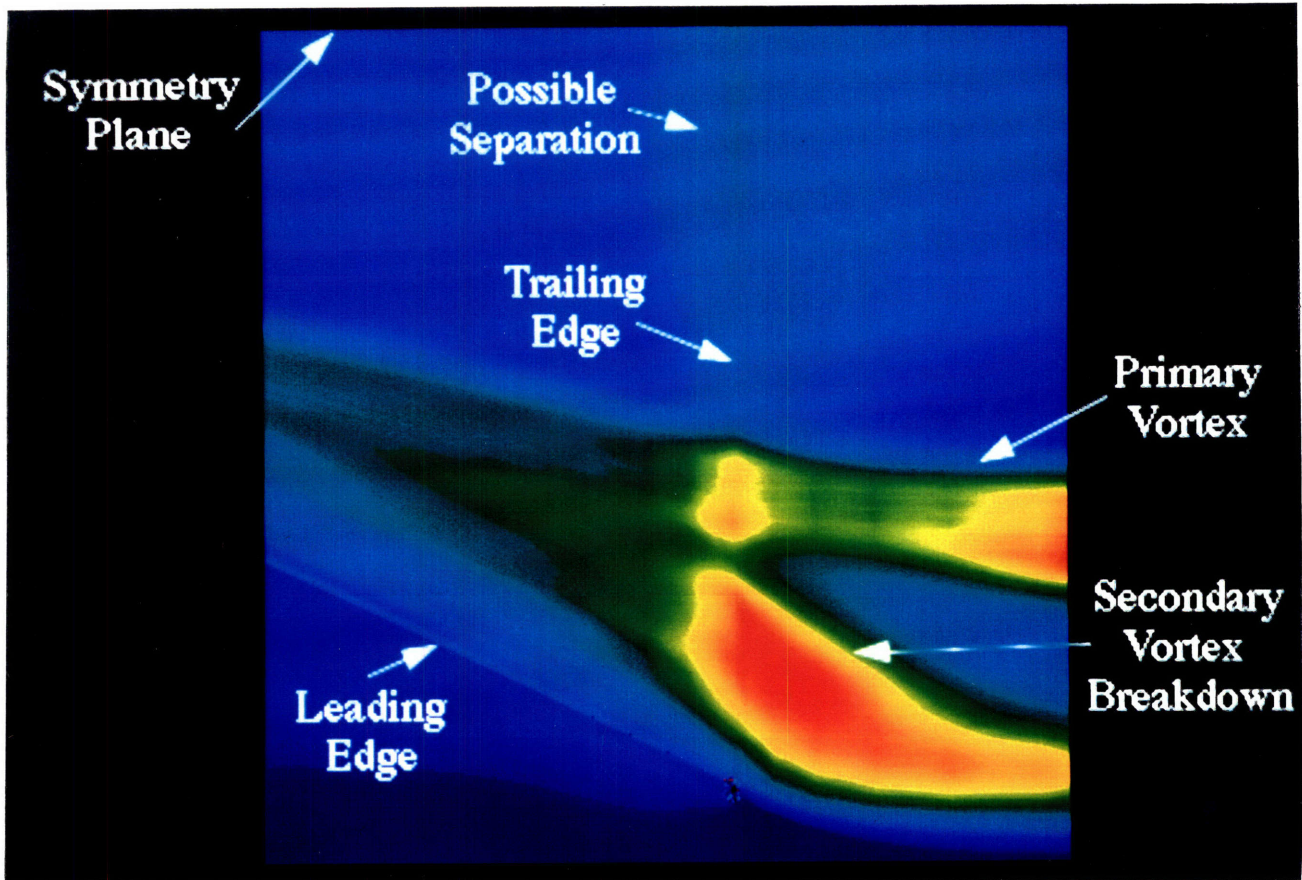

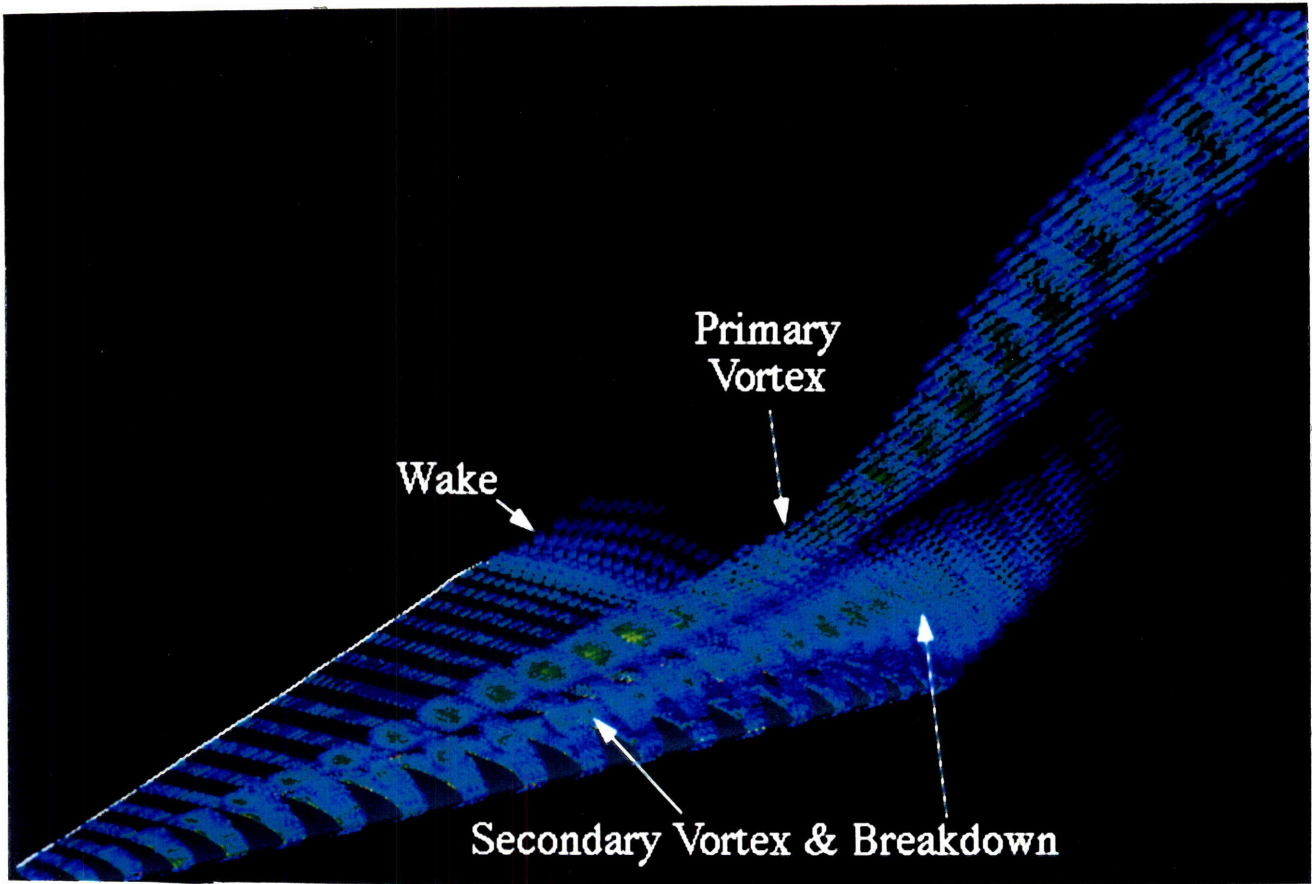Figure 4.4: X-ray of total pressure at trailing edge - midpoint mapping

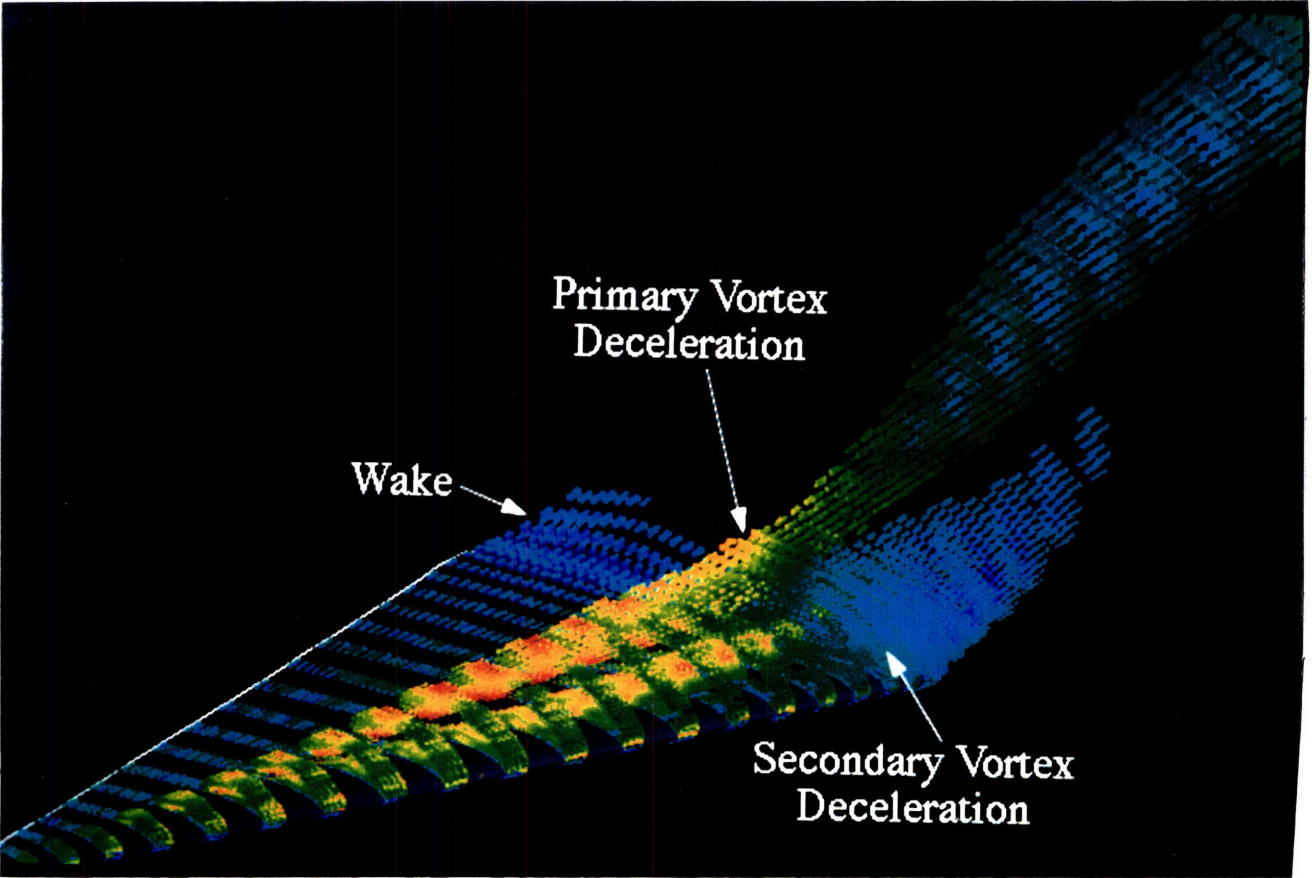Figure 4.5: Cloud of total pressure rendered by total pressure

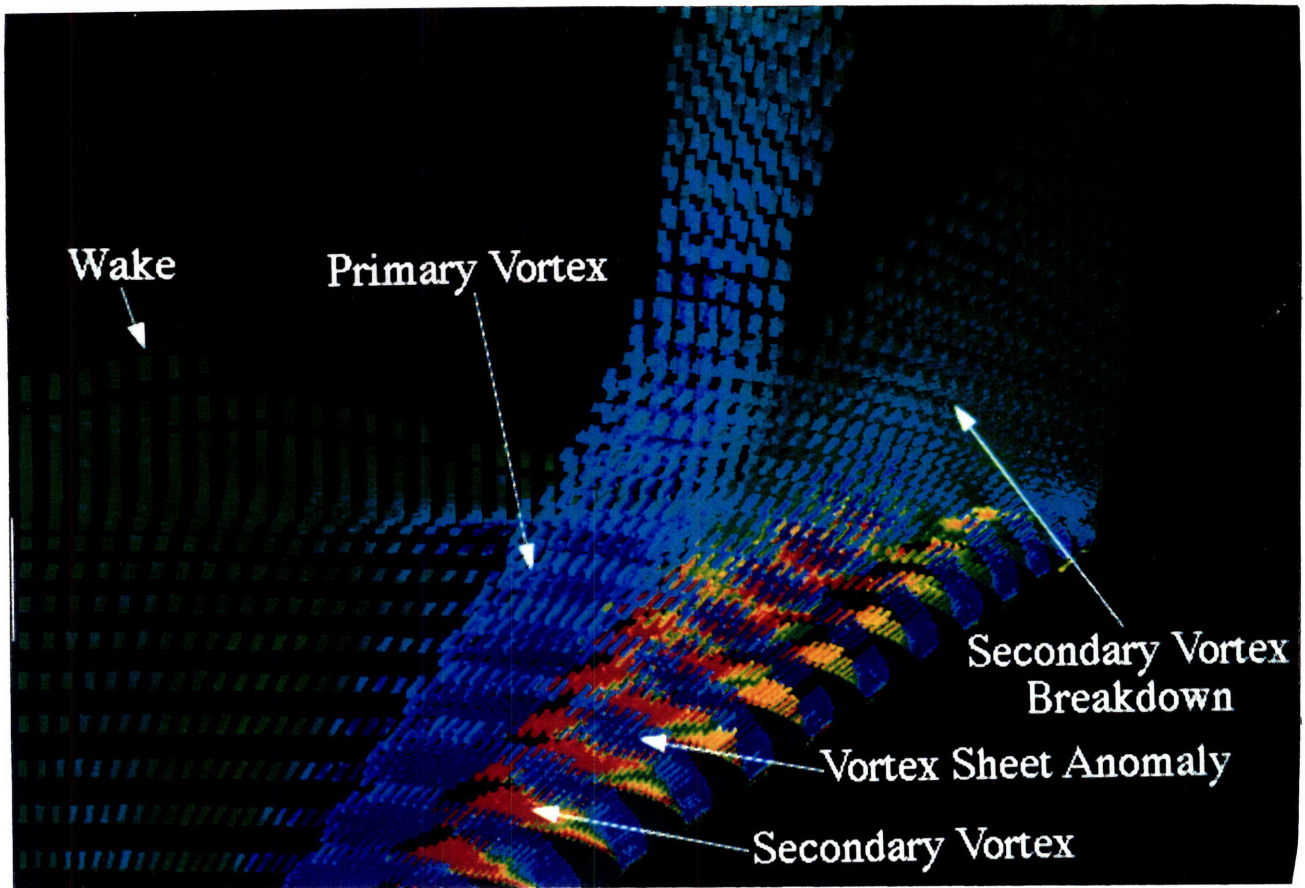Figure 4.6: Cloud of total pressure rendered by Mach number

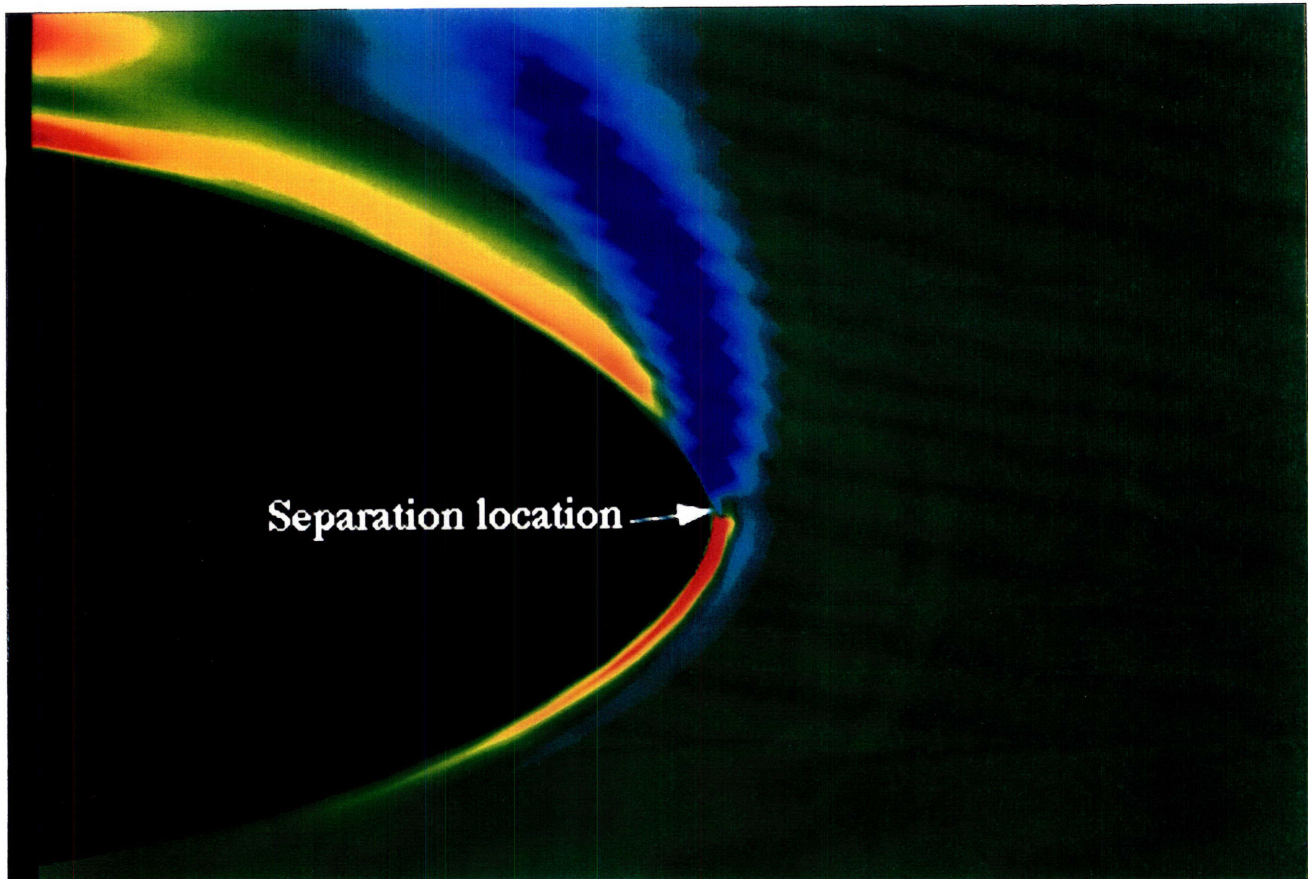Figure 4.7: Cloud of total pressure rendered by helicity

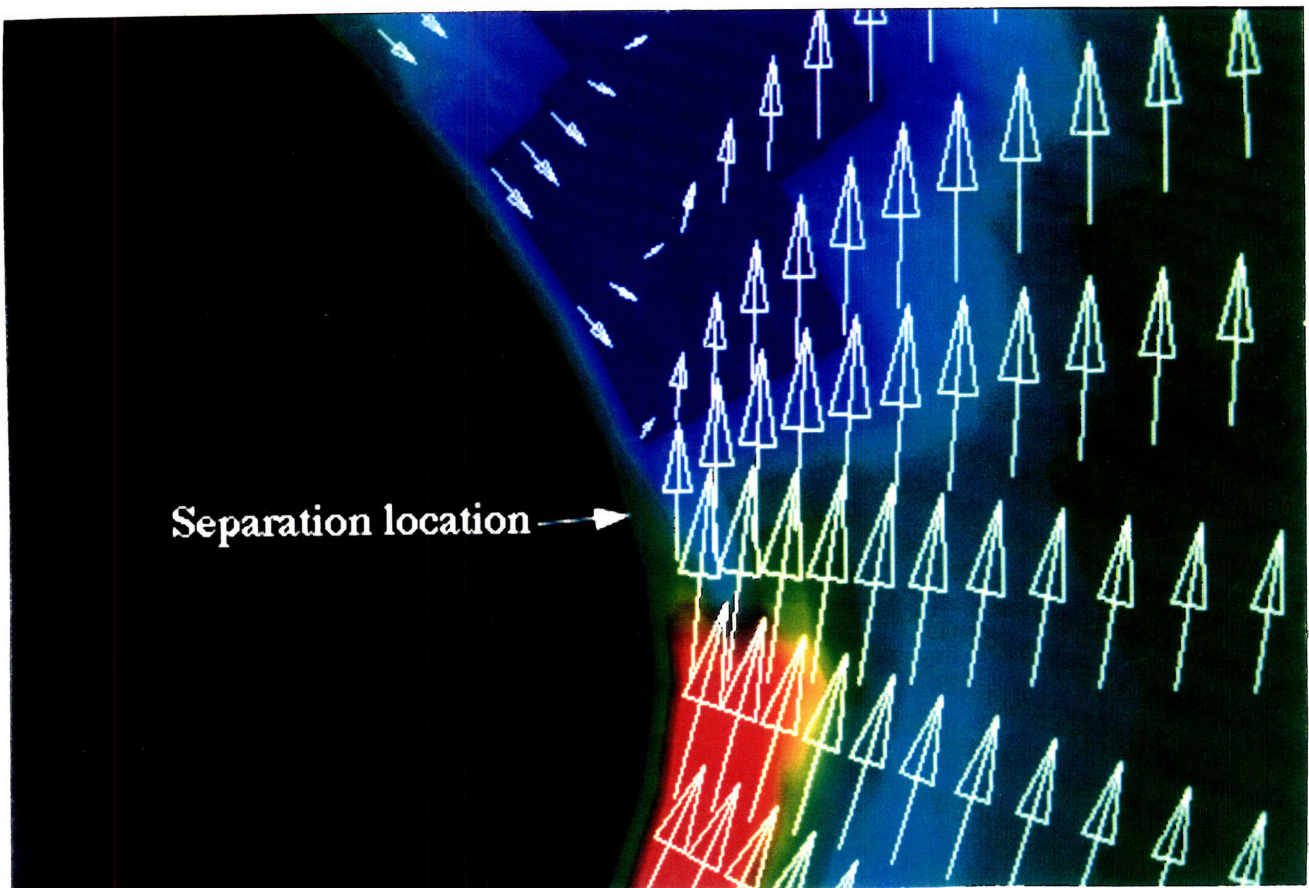Figure 4.8: Helicity at 50% chord showing primary separation

97

Figure 4.9: Tufts at leading edge showing primary separation
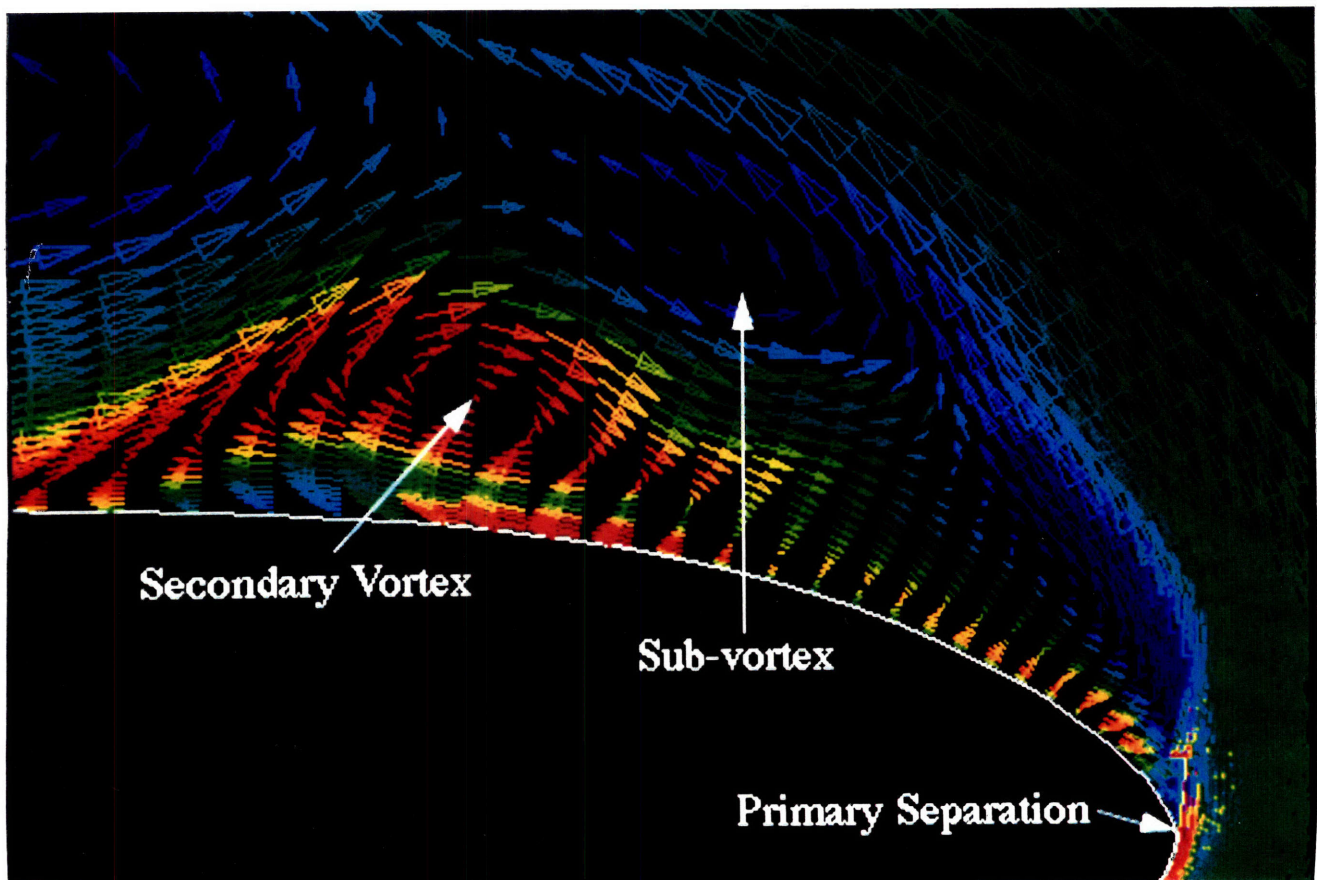

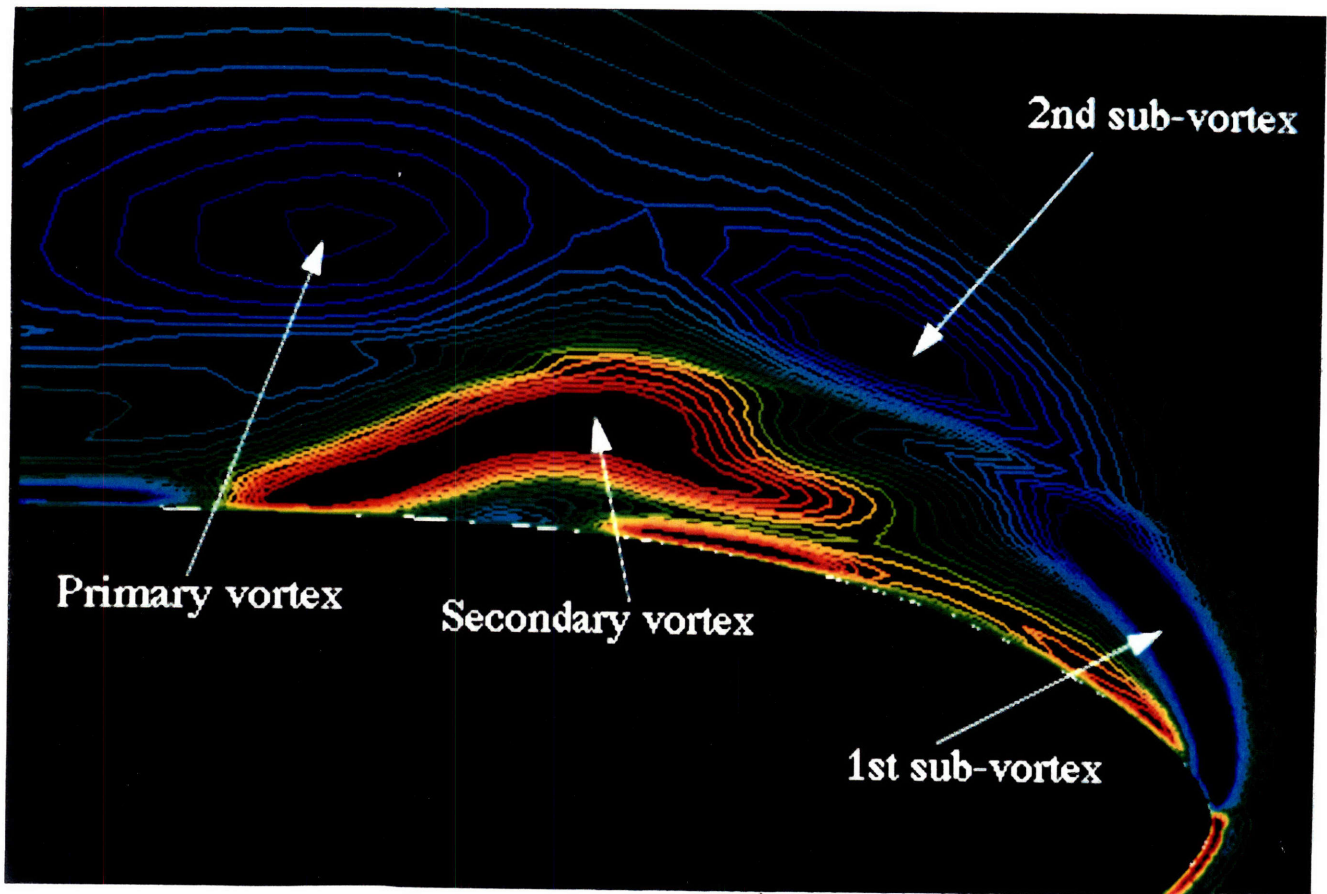Figure 4.10: Tufts in leading vortex sheet anomaly

Figure 4.11: Helicity at 30% chord showing two sub-vortices
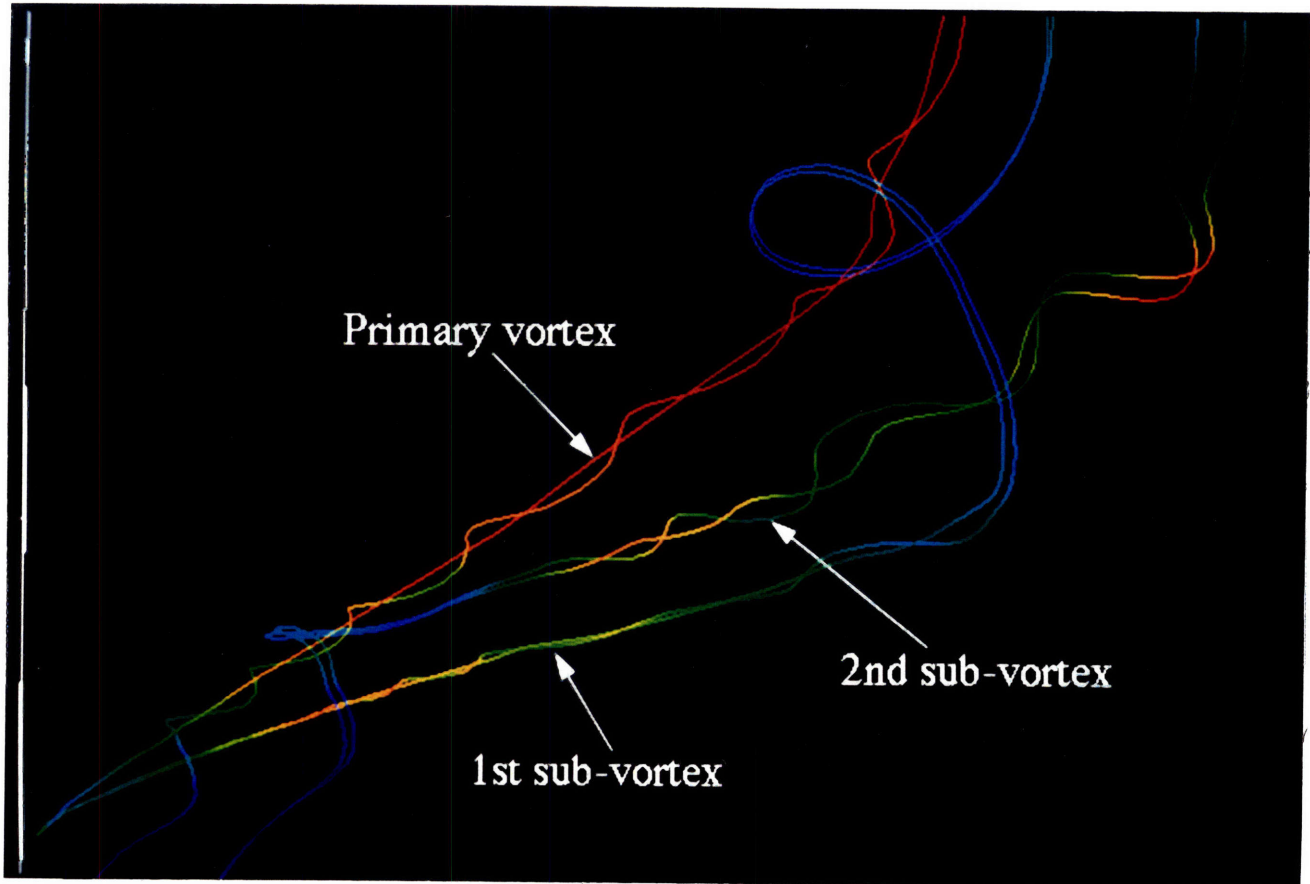
Figure 4.12: Streamlines in sub-vortices rendered by total pressure loss
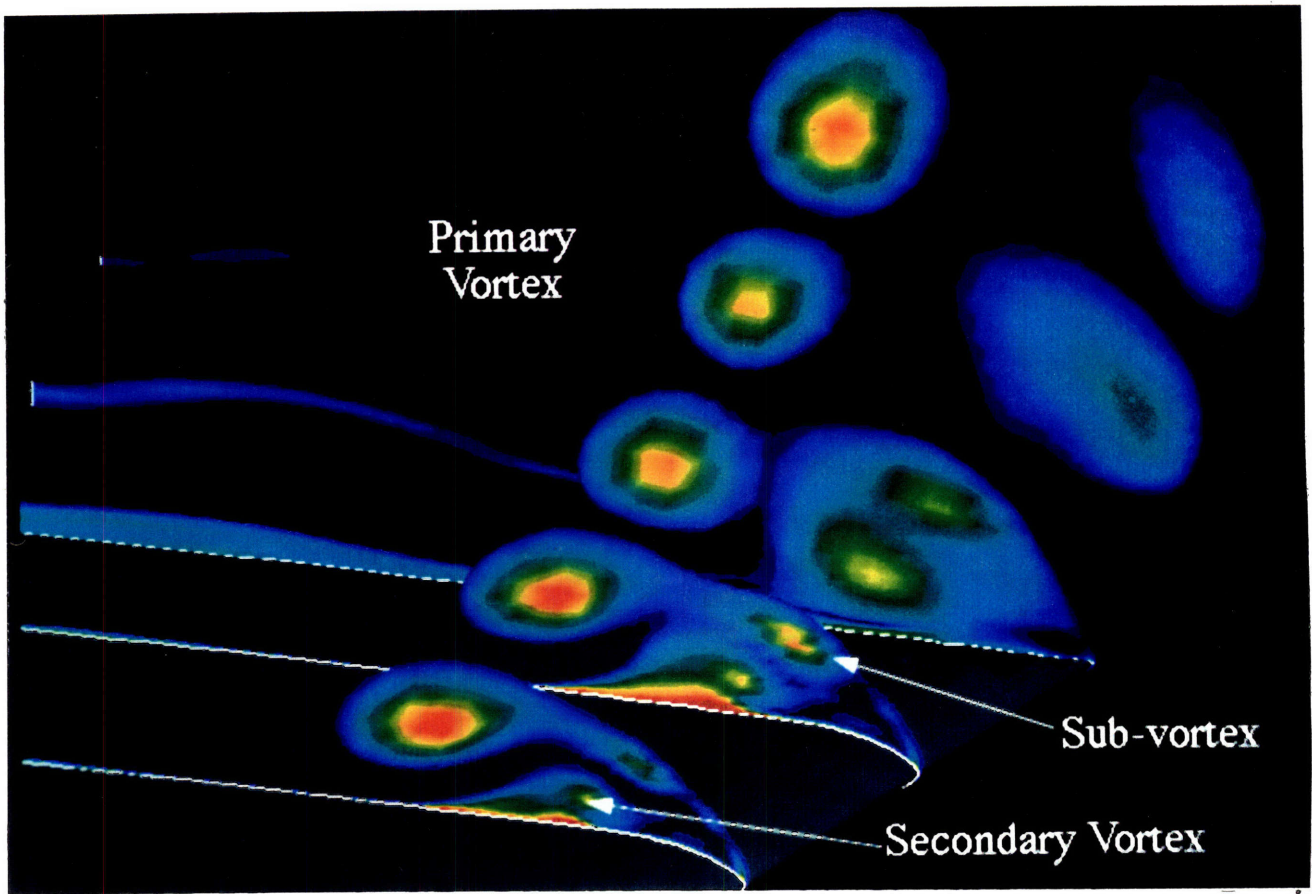
Figure 4.13: Threholded planes of total pressure loss near trailing edge

Figure 4.14: Thresholded planes of helicity near trailing edge

Figure 4.15: Streamlines in secondary vortex rendered by Mach number

Figure 4.16: Tufts along axis of tertiary vortex showing separation

Figure 4.17: Streamlines in tertiary vortex showing separation

Figure 4.18: Streamlines in trailing edge separation region

Figure 4.19: Thresholded cutting planes showing wake
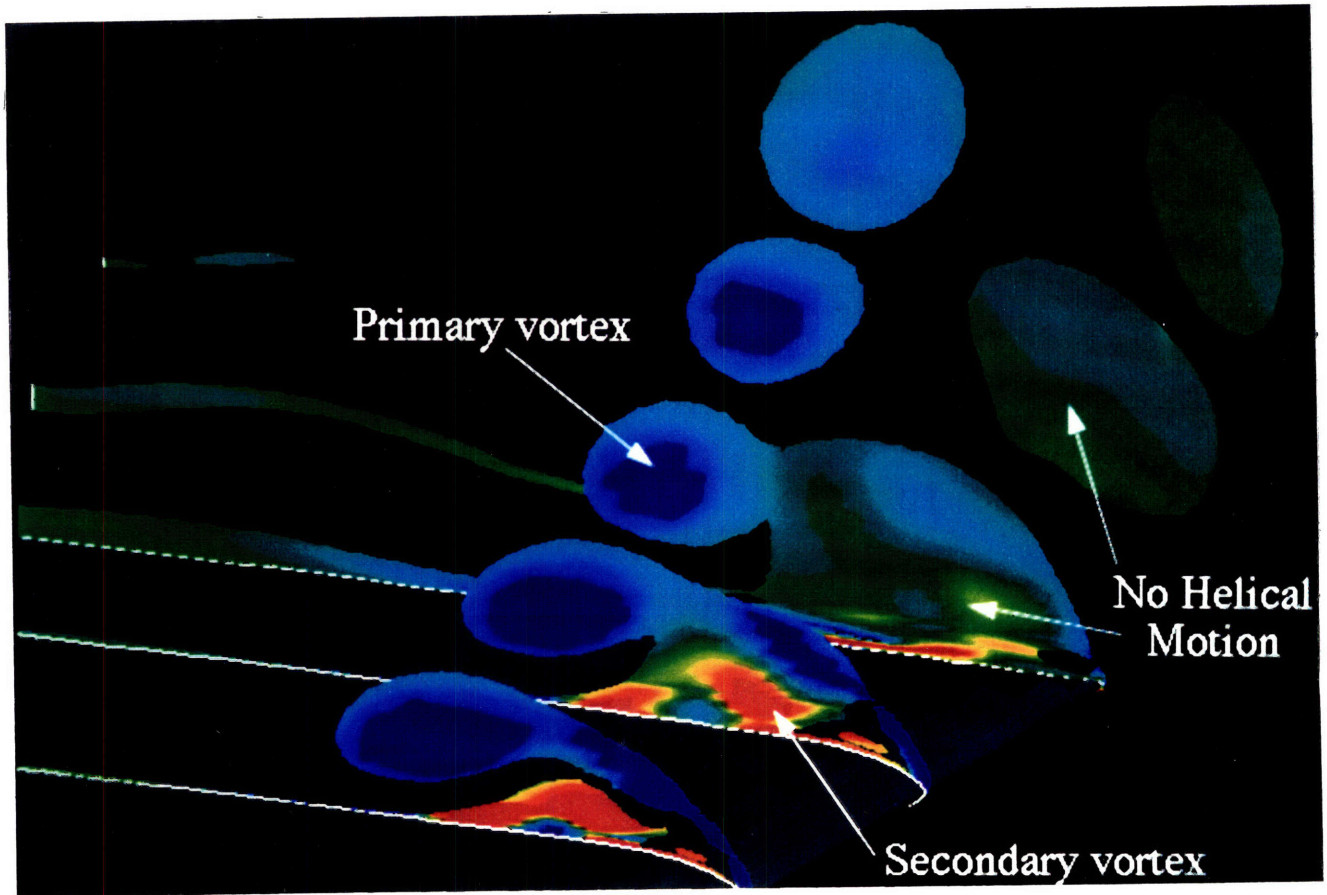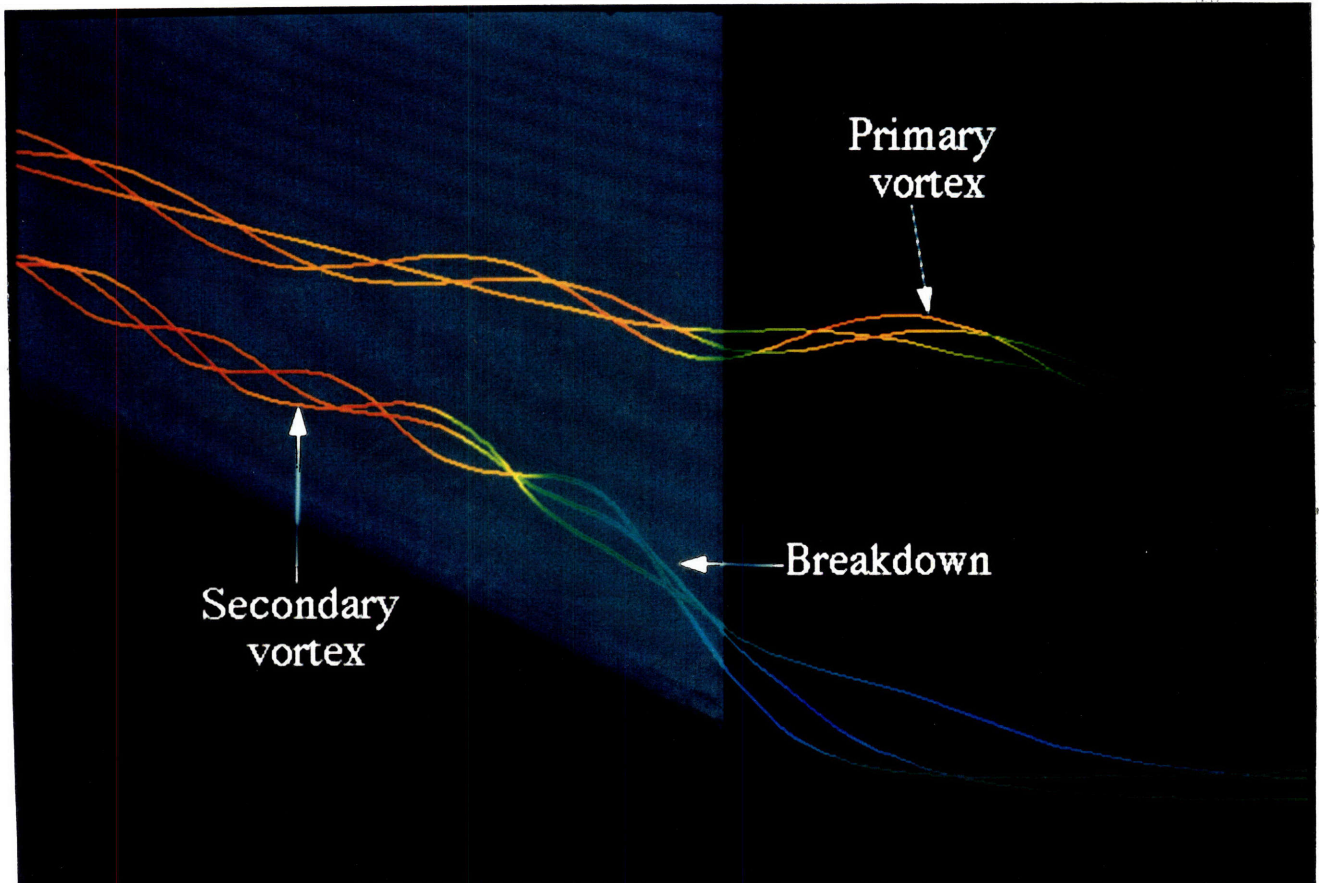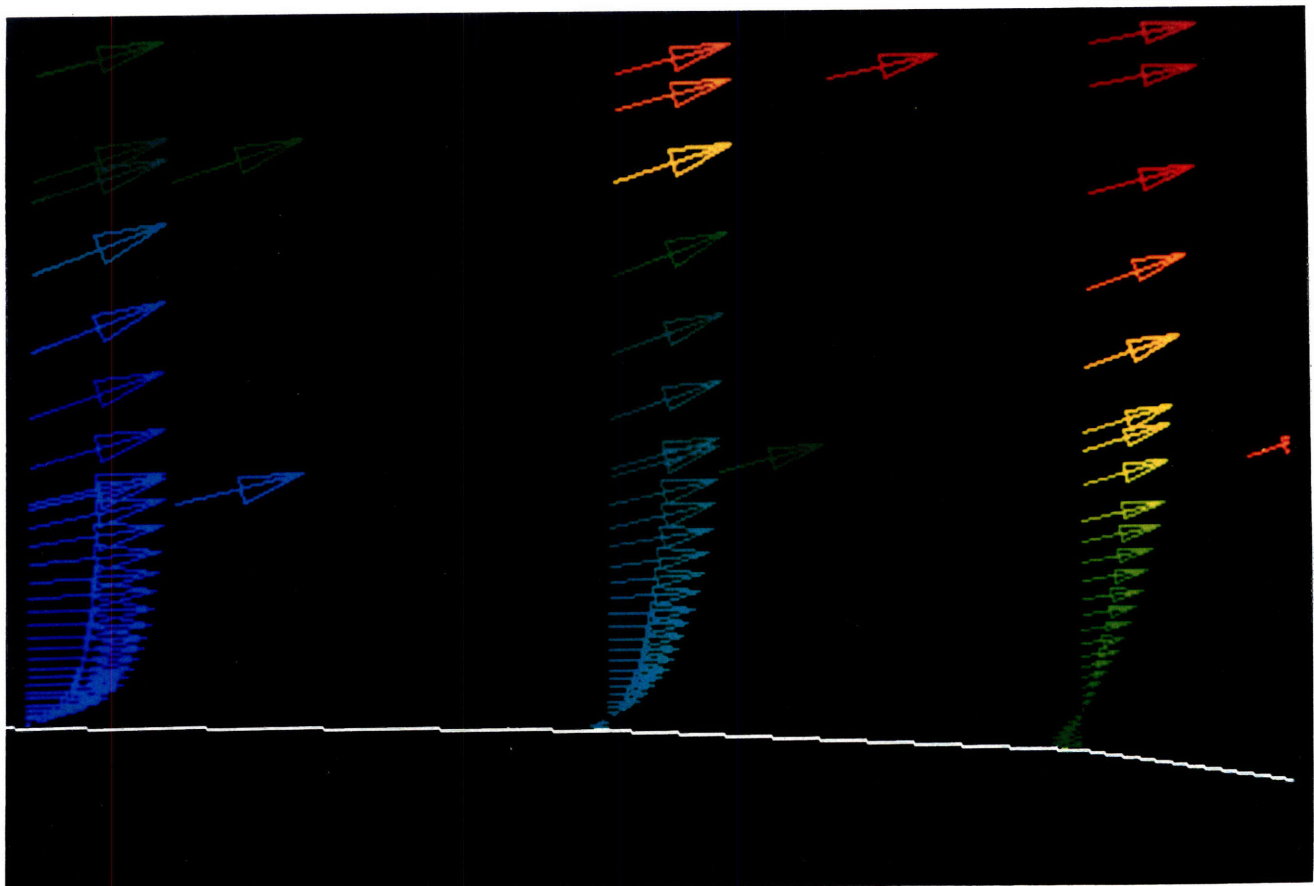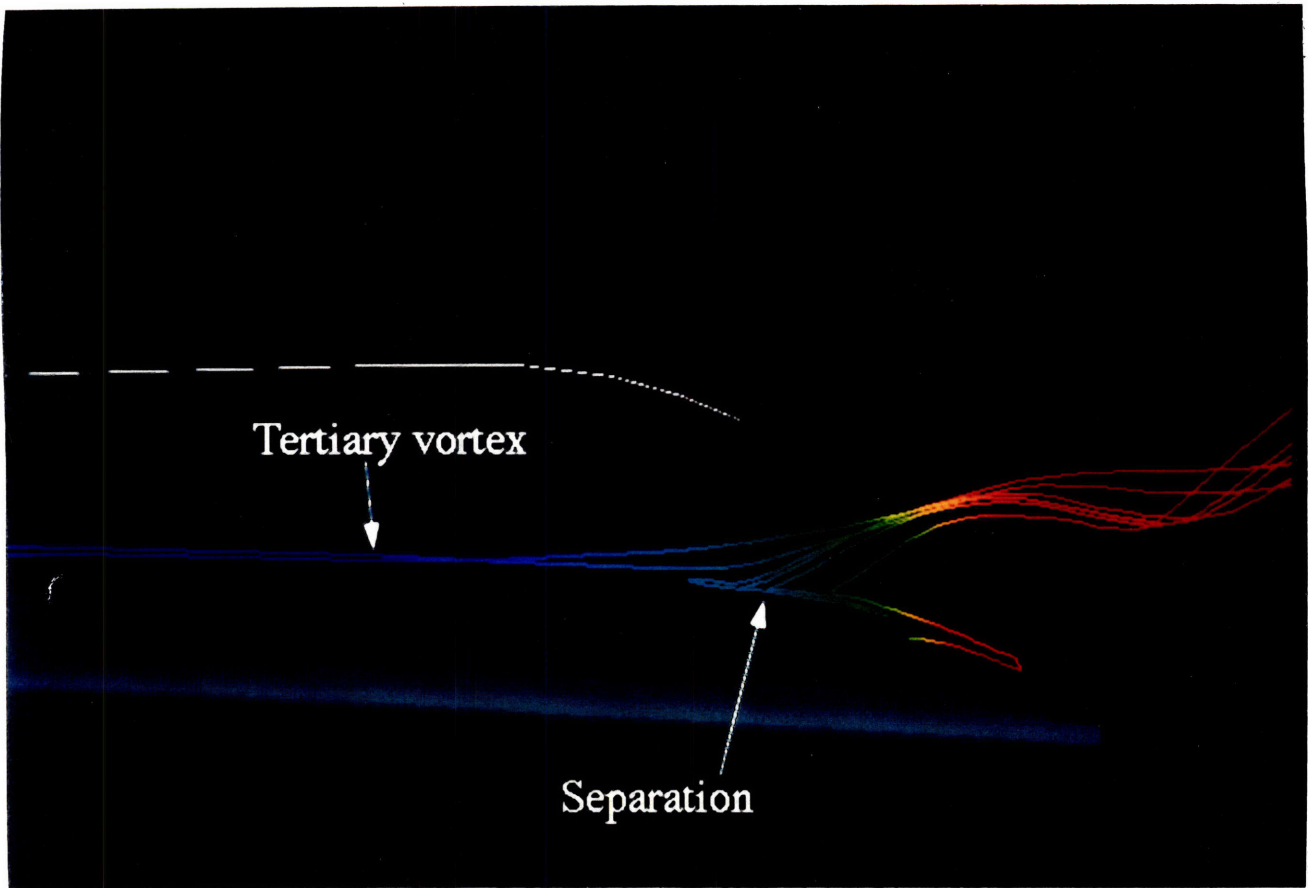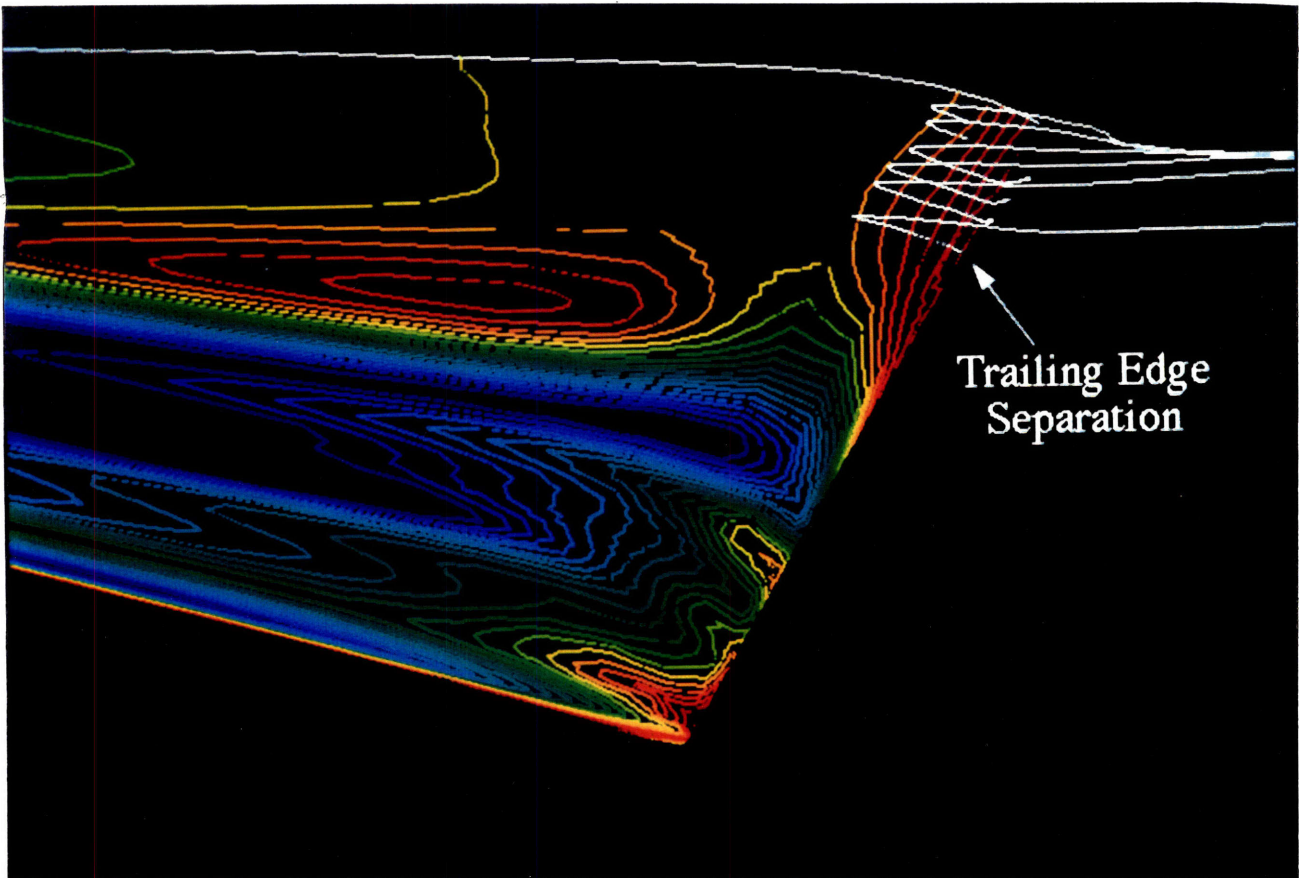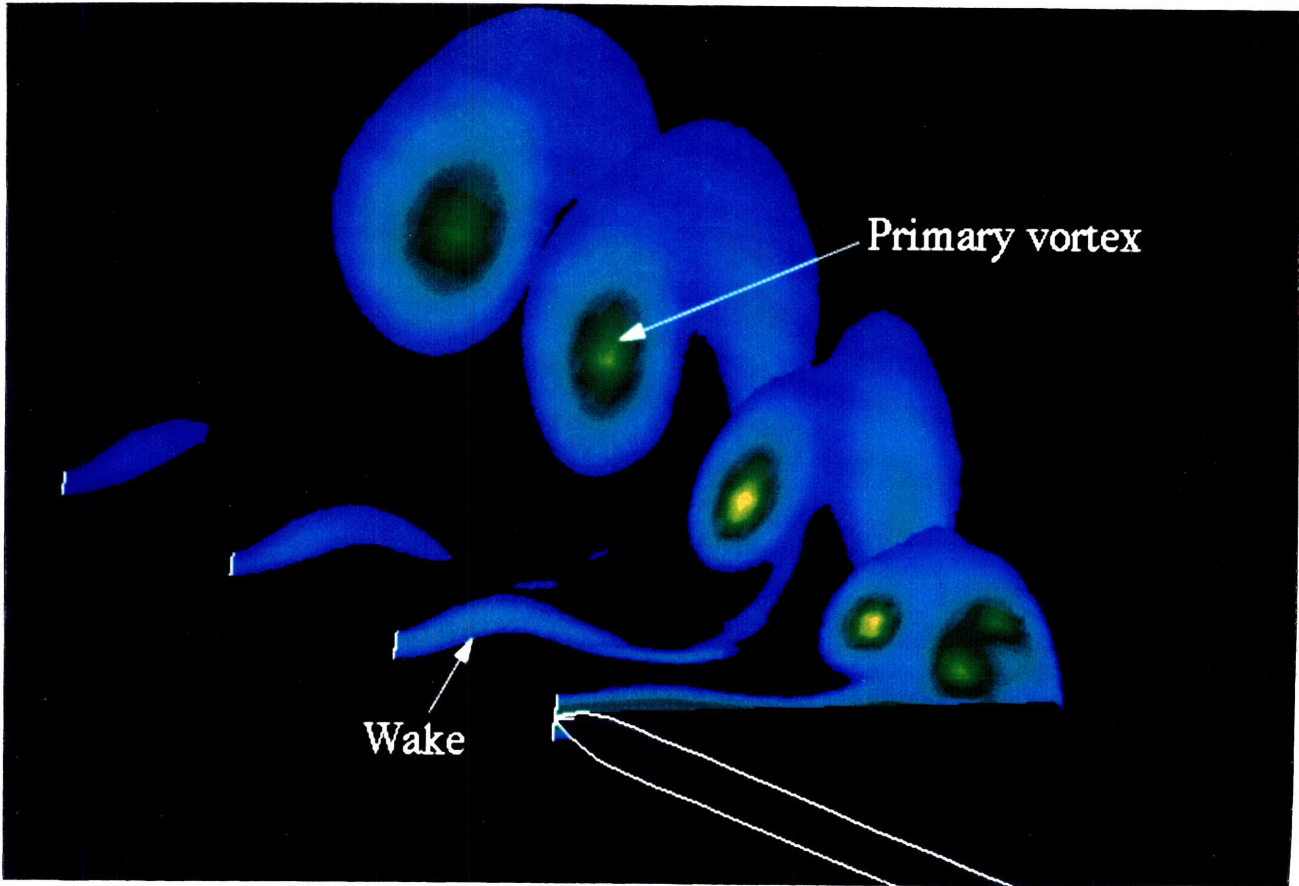
Chapter 5

Conclusions

A systematic, hierarchal approach to visualization of vortical flows was successfully applied. Inherent in the approach is a logical reduction of dimensions as a flow field is investigated. The method begins with first locating any interesting flow features using feature identification in the three-dimensional domain. Then, the flow features are further interrogated using scanning visualization techniques. These scan methods provide two-dimensional information and are extremely powerful when used in a small region. Finally, probing techniques are used to provide the ultimate level of detail. These probes provide one-dimensional information. This hierarchy allows one to first detect regions of interest and then to thoroughly examine them extracting quantative information without wasting time scanning over an entire domain to locate features.

The success of hierarchal visualization is strongly dependent upon the strength of feature identification techniques. A major portion of the work for this thesis was on the development of these new methods. X-rays can be a very informative tool but are often plagued by interpretation difficulties. One of the strengths of X-rays is to highlight any portion or portions of the flow field by using appropriate mapping functions. The clouds technique has proven to be extremely useful. The advantage of clouds over X-rays is that it provides a three-dimensional image where X-rays integrates over one of the spatial dimensions. Also, clouds may be used to determine the quality of a three-dimensional grid. The main drawback to clouds is that the resulting image can still be very "cluttered" and difficult to understand. Finally, a new shock finding technique was developed which proved highly successful in the hypersonic flow used as an example. These identification techniques can not only significantly reduce the time spent visualizing but also increase understanding by locating flow features that ordinarily might be missed.

In visualizing the transonic data set by Becker, several features were clearly detected

by the identification techniques. The surface flow located primary, secondary, and tertiary separation, detected the breakdown of the tertiary vortex, and revealed a region of separated flow at the trailing edge. X-rays identified the secondary vortex breakdown at the trailing edge and accurately detected the wake position. Clouds also detected a strange enlargement in the leading edge vortex sheet which lead to the identification of two sub-vortices believed to be related to the Kelvin-Helmholtz instability of a free shear layer. The shock identification technique indicated the flow to be shockless. All of these various features were then further investigated using probing and scanning techniques. Probing and scanning methods which proved particular useful in this process were cutting planes, thresholding, tufts, and streamlines.

The visualization of vortical flows, and complicated flow fields in general, is extremely difficult and much work still remains to be done. Many possibilities exist for valuable research to be performed. Artificial intelligence (AI) and expert systems could be a great tool for feature identification. Using AI to look for certain features and then display them in some logical fashion would greatly reduce visualization time. A successful AI program could place streamlines in vortices, display shock surfaces, identify region of separated flows, and detect vortex breakdown. The development of an expert system such as this will probably be closely linked with a topological description of the flow field. Obviously, the possibilities are essentially limitless.

Another area of visualization that still needs a great deal of effort is three-dimensional unstructured grid viewing. Currently, unstructured grid viewing is extremely limited and at best amounts to displaying the grid on domain surfaces. As mentioned earlier, clouds is one technique that could be successfully used for unstructured grid viewing. For example, a cloud based on distance from a point, a line, or a plane could be very helpful. The user could interactively select the point, line or plane, and then dynamically scan the threshold limits to display the cells in the surrounding region.

Bibliography

[1] G. Batchelor. *An Introduction to Fluid Dynamics.* Cambridge University Press, 1967.

[2] T. Becker. *Hybrid 3-D Euler/Navier-Stokes Calculations of Transonic Vortex Flows over the NTF Delta Wing.* Master's thesis, M.I.T., August 1989.

[3] C. Dailey and F. Wood. *Computation Curves for Compressible Flow Problems.* Wiley, 1949.

[4] U. Dallman, A. Hilgenstock, S. Riedelbauch, B. Schulte-Werning, and H. Vollmers. *On the Footprints of Three-Dimensional Separated Vortex Flows Around Blunt Bodies.* AGARD Symposium on Vortex Flow Aerodynamics, 1990.

[5] M. Giles. 1991. Personal communication.

[6] M. Giles and R. Haimes. "Advanced Interactive Visualization for CFD." *Computing Systems in Engineering,* 1(1):51–62, 1990.

[7] R. Haimes and M. Giles. *VISUAL3: Interactive Unsteady Unstructured 3D Visualization.* AIAA Paper 91-0794, 1991.

[8] J. Helman and L. Hesselink. *Automated analysis of fluid flow topology.* Proceedings of the SPIE Conference, January 1989.

[9] H. W. M. Hoeijmakers. *Numerical Simulation of Vortical Flow.* NLR TR MP 86032 U, National Lucht-En Ruimtevaartlaboratorium, 1986.

[10] J. Hultquist. "Interactive Numerical Flow Visualization Using Stream Surfaces." *Computing Systems in Engineering,* 1(2-4):349–353, 1990.

[11] R. Korkegi. "A Simple Correlation for Incipient Turbulent Boundary Layer Separation Due To a Skewed Shock Wave." *AIAA Journal,* 11(11):1578–1579, November 1973.

[12] A. Landsberg. *Adaptation for Vortex Flows Using a 3-D Finite Element Solver.* Master's thesis, M.I.T., November 1990.

[13] T. Lasinski, P. Buning, D. Choi, S. Rogers, G. Bancroft, and F. Merritt. *Flow Visualization of CFD using Graphics Workstations.* AIAA Paper 87-1180, 1987.

[14] K.-M. Lee. *Numerical Simulation of Hypersonic Flow Over a Blunt Leading Edge Delta Wing.* Master's thesis, M.I.T., October 1989.

[15] S. Leibovich. *Vortex Stability and Breakdown.* AGARD CP-342, 1983.

[16] Y. Levy, A. Seginer, and D. Degani. "Graphical Representation of Three-Dimensional Vortical Flows by Means of Helicity Density and Normalized Helicity." AIAA Paper 88-2598, June 1988.

[17] R. Löhner, P. Parick, and C. Gumbert. *Some Algorithmic Problems of Plotting Codes on Unstructured Grids.* AIAA Paper 89-1981, 1989.

[18] B. Loyd. *A Semi-Implicit Navier-Stokes Solver and Its Applications to a Study of Separated Flow about Blunt Delta Wings.* PhD thesis, M.I.T., February 1989.

[19] J. McMillin, S.N. Thomas and E. Murman. *Navier-Stokes and Euler Solutions for Lee-Side Flows Over Supersonic Delta Wings.* NASA TP 3035, December 1990.

[20] W. Michael. *Flow Studies on Flat-Plate Delta Wings at Supersonic Speeds.* NACA TN 3472, 1955.

[21] D. Miller and R. Wood. *An Investigation of Wing Leading-edge Vortices at Supersonic Speeds.* AIAA Paper 83-1816, 1983.

[22] E. Murman, T. Becker, and D. Darmofal. "Computation and Visualization of Leading Edge Vortex Flows." *Computing Systems in Engineering,* 1(2-4):341–348, 1990.

[23] K. Narayan and S. Seshadri. *Vortical Flows on the Lee Surface of Delta Wings.* Symposium Transsonicum III, 1989.

[24] R. Newsome and O. Kandil. *Vortical Flow Aerodynamics–physical aspects and numerical simulation.* AIAA Paper 87-0205, 1987.

[25] F. Payne. *The Structure of Leading Edge Vortex Flows Including Vortex Breakdown.* PhD thesis, Notre Dame, May 1987.

[26] K. G. Powell. *Vortical Solutions of the Conical Euler Equations. Notes on Numerical Fluid Mechanics,* Vieweg, 1990. ScD thesis, M.I.T., July, 1987.

[27] A. Rizzi. "Euler Solutions of Transonic Vortex Flow Around the Dillner Wing." *Journal of Aircraft,* 22(4):325–328, 1985.

[28] A. Rizzi, G. Drougge, and B. Müller. *Navier-Stokes and Euler Solutions for Vortex Flow over a Delta Wing.* Symposium Transsonicum III, 1989.

[29] A. Rizzi, E. Murman, P. Eliasson, and K.-M. Lee. *Calculation of Hypersonic Leeside Vortices Over Blunt Delta Wings.* AGARD Symposium on Vortex Flow Aerodynamics, 1990.

[30] S. Ruffin. *Solutions for Hypersonic Viscous Flow over Delta Wings.* Master's thesis, M.I.T., May 1987.

[31] S. Seshadri and K. Narayan. "Shock-Induced Separated Flows on the Lee Surface of Delta Wings." *Aeronautical Journal,* 91(903):128–141, 1987.

[32] M. Siclari, M.J. Mandel and A. Scuderi. "Flow Visualization Research at Grumman's Computational Aerodynamics Laboratory." AIAA Paper 89-0137, 1989.

[33] A. Stanbrook and L. Squire. "Possible Types of Flows at Swept Leading Edges." *Aeronautical Quarterly,* 15(1):72–82, 1964.

[34] G. Volpe. "Streamlines and Streamribbons in Aerodynamics." AIAA Paper 89-0140, January 1989.

[35] G. Vorropoulos and J. Wendt. *Laser Velocimeter Study of Compressibility Effects on the Flow Field of Delta Wings.* AGARD CP-342, 1983.

[36] S. Webb. *The Physics of Medical Imaging.* IOP Publishing Ltd., 1988.

[37] R. F. Weston. *Color Graphics Techniques for Shaded Surface Displays of Aerodynamic Flowfield Parameters.* AIAA Paper 87-1182, 1987.

Appendix A
Glossary of Visualization Terms

contouring - a rendering technique displaying lines of constant scalar values colored by the scalar. The spacing of contours reflects local scalar gradients.

cutting plane - a planar surface which cuts through the three-dimensional computational domain. The plane may be interactively scanned along its normal direction. The position of the plane along the normal direction is a scalar variable which parameterizes the planes for a given normal direction. Thus, cutting planes can be thought of as a geometric subset of iso-surfaces.

Goraud shading - a color rendering method for triangular surfaces using linear interpolation of nodal color values to determine the color of internal points. This shading is typically performed by hardware on graphics mini-supercomputers.

iso-surface - a three-dimensional surface of constant scalar value. The given scalar values parameterize the iso-surfaces and the surfaces may be interactively scanned by varying this scalar parameter.

pathline - lines through a vector field which are everywhere tangent to the vector field at an instant in time.

rendering - the drawing of images onto the screen

ribbon - pathlines of a constant width with twist that indicates the local pathwise angular rotation. One edge of the ribbon is a true pathline. The other edge is constructed by rotating a constant length normal vector about the path according to the local pathwise rotation rate of the vector field.

screen coordinates - a left-handed coordinate system with the x-axis pointing from left to right on the screen, the y-axis pointing from bottom to top on the screen, and the z-axis pointing into the screen.

streamline - a pathline of the velocity vector field.

surface pathline - a pathline constrained to lie on a surface.

thresholding - a rendering technique limiting the displayed portion of a surface to areas where the scalar value falls within a user-defined range.

Appendix B

X-ray Algorithm Description

The X-ray algorithm is a complicated calculation which, when considering a single ray, is very similar to streamline integration. Before describing the algorithm, the following terminology is necessary. The computational coordinate system is simply (x, y, z). The screen coordinate system is denoted by primes, (x', y', z') with the x'-axis tangent to the screen plane and pointing to the right, the y'-axis tangent to the screen plane and pointing upward, and the z'-axis directed into the screen. This defines a left-handed coordinate system which is standard in 3-D graphics. Boundary faces are the cell faces which make up the domain boundaries. The X-ray grid is set-up such that the origins of the X-rays form a square Cartesian grid centered on the z'-axis, having a unit length side, and aligned with the x'- and y'-axes (Figure B.1). The number of rays on a side is N_{rays} and the total number of rays is N_{rays}^2. The X-ray grid is simply a two-dimensional structured grid of the form, $xr(i, j)$ where $1 \leq i, j \leq N_{rays}$. Thus, a simple algebraic mapping exists relating (i, j) to the X-ray origin in the screen coordinate system. Finally, because VISUAL3 allows tetrahedra, pyramid, prism, and hexahedra cells, it was necessary to handle both triangular and quadrilateral cell faces. This problem was solved by breaking all quadrilateral faces into triangles. Thus, calculations are performed only on triangular faces.

For a single ray, the X-ray algorithm is as follows:

1. Determine the boundary faces which the X-ray intersects and sort them by distance from the X-ray plane.

2. Determine the first cell which the ray enters from the sorted boundary face list.

3. Calculate the cell face from which ray exits and perform the numerical integration of Equation 3.1 using a trapezoidal approximation from cell entrance to cell exit.

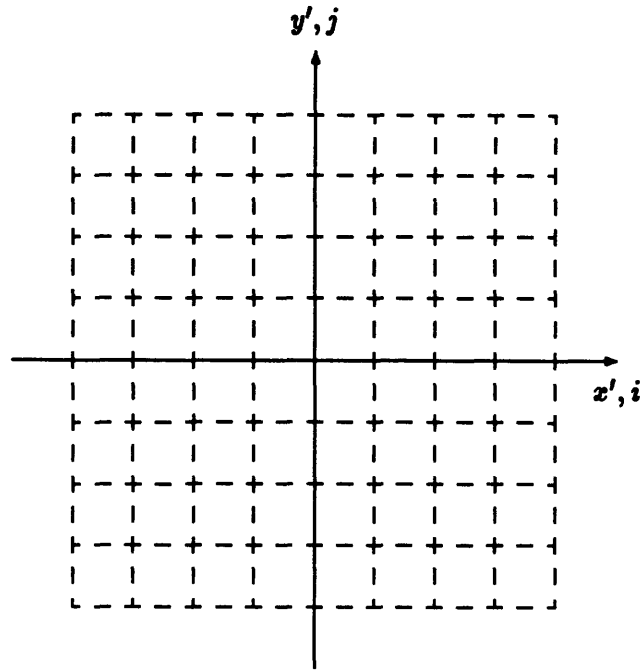4. If the ray has entered another cell repeat the previous step.

Figure B.1: X-ray grid

5. If the ray has left the domain, determine if it re-enters by scanning the sorted boundary face list for an intersection beyond the current location. If so, continue the cell-to-cell integration process. If not, the integration is done.

Upon trying this algorithm the speed was too slow to allow adequate interactivity. A profiling of an X-ray calculation revealed that much of the time was being spent in determining which boundary faces a ray intersects. The problem with the algorithm is that for each X-ray a calculation must performed over the list of all boundary faces.

In order to increase the speed, it was necessary to alter the boundary face calculations. Instead of calculating which boundary faces intersect a given ray, the problem was reversed; in other words, the rays which intersect a given boundary face were calculated. Thus, the new boundary algorithm contains one loop over all boundary faces. The result is a linked-list of all the faces which intersect each X-ray (i,j). Specifically, the algorithm for boundary face k is:

1. Calculate the screen coordinates, $\vec{x^j}(i)$, of the triangular boundary face where $i = 1, 2, 3$ for each node of the triangle.

119

2. Determine the minimum and maximum y' values. The minimum and maximum points are now called $\vec{x}'_{bot}$ and $\vec{x}'_{top}$; the remaining point of the triangle becomes $\vec{x}'_{mid}$ (See Figure B.2).

3. Determine the j range of X-rays which face k spans from y'_{bot} and y'_{top}. Loop over the range from (j_{bot}, j_{top}).

4. Determine x'_{left} and x'_{right} for y'_j; if $y'_j < y'_{mid}$ then sides a and b are used, else sides a and c are used.

5. Determine i_{left} and i_{right} from x'_{left} and x'_{right}.

6. Add boundary face k to the linked list for X-rays (i_{left}, j) to (i_{right}, j).

7. Continue loop over j-range.

8. Boundary face k is completed; continue loop.

This algorithm significantly improves the speed. The first step of the original algorithm is now completely eliminated; otherwise, the general procedure remains exactly the same. A final gain in speed may be obtained by parallelizing the integration of each ray; this is possible because the calculation for each ray is completely independent.
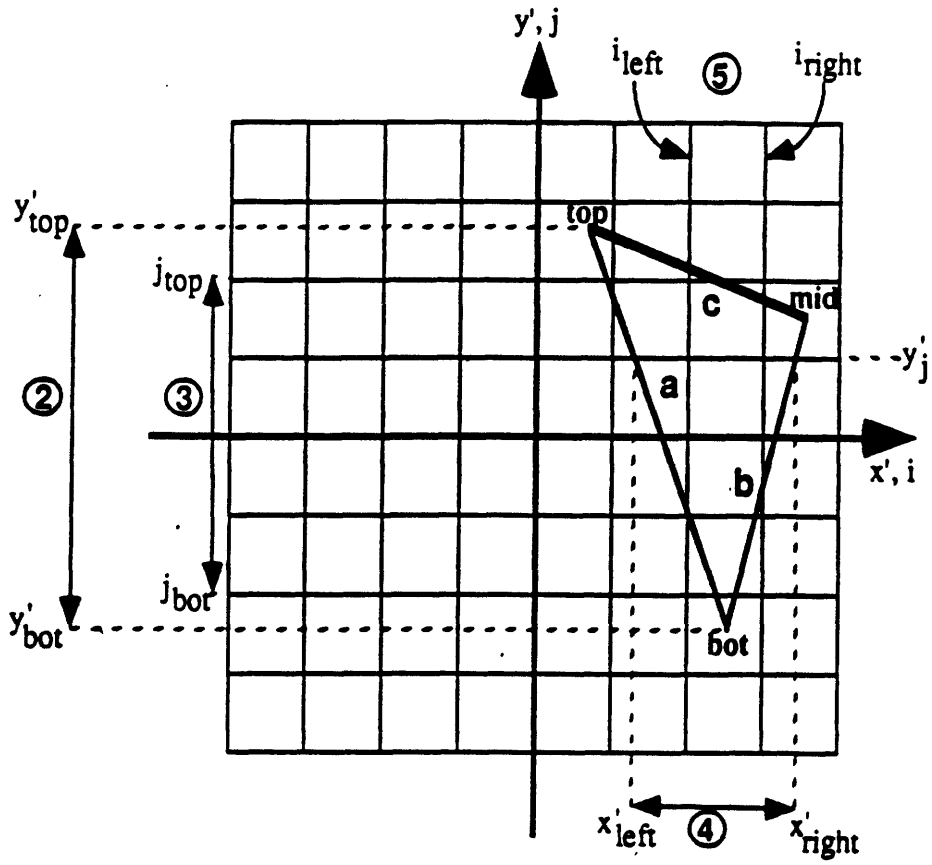
Figure B.2: X-ray : boundary face algorithm

Appendix C

Clouds Algorithm Description

The algorithm used for clouds is simple to implement and is based upon the variation of the algorithm used in VISUAL3 for cutting planes and iso-function surfaces[6]. Recalling that VISUAL3 deals with a computation on unstructured grid, an individual cell will be referenced by the letter j, where $1 \leq j \leq N_{cells}$. The basic procedure is as follows:

1. Calculate the cell-average scalar threshold variable, t'_j for each j.

2. Sort t'_j.

3. Find the location of the user-set limits, t'_{min} and t'_{max} in the sorted list. Render any cells which appear between these two values in the sorted t' list.

4. If the user changes t'_{min} or t'_{max} then the new limits may be found very quickly and the desired cells are rendered.

Using this technique, only the initial set-up and sort is expensive. The set-up involves calculating the t'_j values which is an $O(N_{cells})$ operation. The sort used is a combination of a merge sort and a quick sort. The list is divided in half sending $N_{cells}/2$ cells to two separate processors. Next, the two halves are sorted in parallel using a quick sort which is $O(N_{cells} \log N_{cells})$. Finally, a merge sort is performed upon the two halves which is $O(N_{cells})$. Thus, the total initialization time is $O(N_{cells} \log N_{cells})$ due to the quick sort. The advantage of this algorithm is that, after initialization, the calculation time is very small.